# Photovoltaics International

THE TECHNOLOGY RESOURCE FOR PV PROFESSIONALS

## Edition 45

**Busbarless solar cells**
Fraunhofer ISE discusses the challenge of measuring busbarless cells

**PERC cell failure**
Suntech asks whether we truly understand the failure mechanism of PERC cells

**Industrial PERC**
ISFH looks at projections for PERC+ solar cells with efficiencies up to 24%

**Heterojunction bifaciality**
CEA-INES reveals the optimal bifaciality of silicon heterojunction cells

**Tandem cells**
What's needed to bring c-Si tandem technology into production

www.pv-tech.org
PVTECH.ORG

JA SOLAR

## Integration of Five Leading Technologies
## Excellent Power Generation Performance

**450W+ Mass Production in Ramp Up**

www.jasolar.com

Harvest the Sunshine

Photovoltaics International

Published by:
Solar Media Ltd.,
123 Buckingham Palace Rd
Victoria, London SW1W 9SH
United Kingdom
T: +44 (0) 207 871 0122
T: +44 (0) 7827 885311
E info@pv-tech.org
www.pv-tech.org

Publisher: **David Owen**

Editor in Chief: **Liam Stoker**
Technical Publishing Director: **Mark Osborne**
Commissioning Editor: **Adam Morrison**
Sub-Editor: **Steve D. Brierley**
Design: **Tina Davidian**
Production: **Daniel H Brown, Sarah-Jane Lee**
Sales Director: **David Evans**
Account Managers: **Adam Morrison, Graham Davie, Lili Zhu**



Cover image: Perovskite silicon tandem solar cells in pilot production. Credit: Oxford PV

Printed by Buxton Press

Photovoltaics International
Forty Fifth Edition
November 2020
Photovoltaics International is a six monthly journal published in February and September each year.

Distributed in the USA by Mail Right International, 1637 Stelton Road B4, Piscataway, NJ 08854.

ISSN: 1757-1197



USPS Information
USPS Periodical Code: 025 313

Periodicals Postage Paid at
New Brunswick, NJ
Postmaster: Send changes to:
Photovoltaics International,
Solar Media Ltd., C/o 1637 Stelton Road,
B-4, Piscataway, NJ 08854, USA

# Foreword

Welcome to Photovoltaics International 45. The foreword of the previous volume of PVI, published in May 2020, mentioned the impact of the COVID-19 pandemic but, in truth, we were all still in the early days and perhaps had little understanding of quite how severe the spread of the novel coronavirus would be on a global scale. Now, six months on, the industry is acutely aware of the disruption it has caused and continues to cause.

But the last six months has also been typified by the determination of an industry to press ahead. The avalanche of new manufacturing capacity announcements referenced in the pages of PVI 44 has not only continued, but accelerated in the second half of the year and, driven by increased demand, the PV supply chain stands on the cusp of a new era of manufacturing.

Suffice to say, this new era is being at least partly facilitated by significant developments in technology, some of which grace the pages of this edition of PVI.

The Fraunhofer Institute for Solar Energy Systems details how the omission of busbars from solar cells introduces new challenges to the accurate measurement of their current and voltage, while also exploring the two main approaches for measuring such cells that have evolved as a result.

Suntech provides a deep dive into the failure mechanism of passivated emitter rear cell (PERC) technology, detailing how some monofacial/bifacial PERC cells have been found to demonstrate much higher power degradation than alternatives after damp-heat exposure. Its paper (p.19) reveals how deviations between standard IEC conditions and real field conditions may result in misleading conclusions from lab test results.

ISC Konstanz has also led a team of authors from organisations including Oxford PV, NREL, UNSW and others which reviews c-Si based tandem technology and, crucially, determines what is needed to bring that technology into production as the industry looks to achieve that milestone within the next three to five years or, as the paper argues, perhaps even sooner.

Meanwhile, CEA-INES explores both the advantages and disadvantages of increasing the bifaciality of heterojunction solar cells by tuning the pattern of metal grids on the front and back side, detailing how very high bifaciality comes at a cost of lower conversion efficiency of the module's front side.

We also have a paper from Jolywood Solar Technology that discusses the progress towards 24% efficiency of industrial n-type bifacial passivating-contact solar cells, using its own experiences as one of the first few manufacturers to produce cells and modules featuring passivating-contract technology on an industrial scale.

Be safe, stay well, and we look forward to bringing you the next edition of PVI in the new year.

**Liam Stoker**
Editor in chief
Solar Media Ltd.

# Editorial Advisory Board

Photovoltaics International's primary focus is on assessing existing and new technologies for "real-world" supply chain solutions. The aim is to help engineers, managers and investors to understand the potential of equipment, materials, processes and services that can help the PV industry achieve grid parity. The Photovoltaics International advisory board has been selected to help guide the editorial direction of the technical journal so that it remains relevant to manufacturers and utility-grade installers of photovoltaic technology. The advisory board is made up of leading personnel currently working first-hand in the PV industry.

Our editorial advisory board is made up of senior engineers from PV manufacturers worldwide. Meet some of our board members below:

**Prof Armin Aberle, CEO, Solar Energy Research Institute of Singapore (SERIS), National University of Singapore (NUS)**

Prof Aberle's research focus is on photovoltaic materials, devices and modules. In the 1990s he established the Silicon Photovoltaics Department at the Institute for Solar Energy Research (ISFH) in Hamelin, Germany. He then worked for 10 years in Sydney, Australia as a professor of photovoltaics at the University of New South Wales (UNSW). In 2008 he joined NUS to establish SERIS (as Deputy CEO), with particular responsibility for the creation of a Silicon PV Department.

**Dr. Markus Fischer, Director R&D Processes, Hanwha Q Cells**

Dr. Fischer has more than 15 years' experience in the semiconductor and crystalline silicon photovoltaic industry. He joined Q Cells in 2007 after working in different engineering and management positions with Siemens, Infineon, Philips, and NXP. As Director R&D Processes he is responsible for the process and production equipment development of current and future c-Si solar cell concepts. Dr. Fischer received his Ph.D. in Electrical Engineering in 1997 from the University of Stuttgart. Since 2010 he has been a co-chairman of the SEMI International Technology Roadmap for Photovoltaic.

**Dr. Thorsten Dullweber, Head of PV Department at the Institute for Solar Energy Research Hamelin (ISFH)**

Dr. Thorsten Dullweber is leading the PV Department and the R&D Group Industrial Solar Cells at ISFH. His research work focuses on high efficiency industrial-type PERC and bifacial PERC+ silicon solar cells, where he co-authored more than 100 Journal and Conference publications. Before joining ISFH in 2009, Thorsten worked as project leader for DRAM memory chips at Infineon Technologies AG. He received his Ph. D. degree in 2002 for research on Cu(In,Ga)Se2 thin film solar cells. Thorsten is member of the Scientific Committees of the EU-PVSEC and SNEC conferences.

**Dr. Wei Shan, Chief Scientist, JA Solar**

Dr. Wei Shan has been with JA Solar since 2008 and is currently the Chief Scientist and head of R&D. With more than 30 years' experience in R&D in a wider variety of semiconductor material systems and devices, he has published over 150 peer-reviewed journal articles and prestigious conference papers, as well as six book chapters.

**Florian Clement, Head of Group, MWT solar cells/printing technology, Fraunhofer ISE**

Dr. Clement received his Ph.D in 2009 from the University of Freiburg. He studied physics at the Ludwigs-Maximilian-University of Munich and the University of Freiburg and obtained his diploma degree in 2005. His research is focused on the development, analysis and characterization of highly efficient, industrially feasible MWT solar cells with rear side passivation, so called HIP-MWT devices, and on new printing technologies for silicon solar cell processing.

Vertex

# Lower Voltage, Higher Module String Power Output

**600W/550W** high power,
with more than **21%+** high efficiency

- Multi-busbar and dense interconnection technology
- Extremely high string power for maximum usage of field
- Lower BOS cost and optimized customer value

*www.trinasolar.com*

Trinasolar

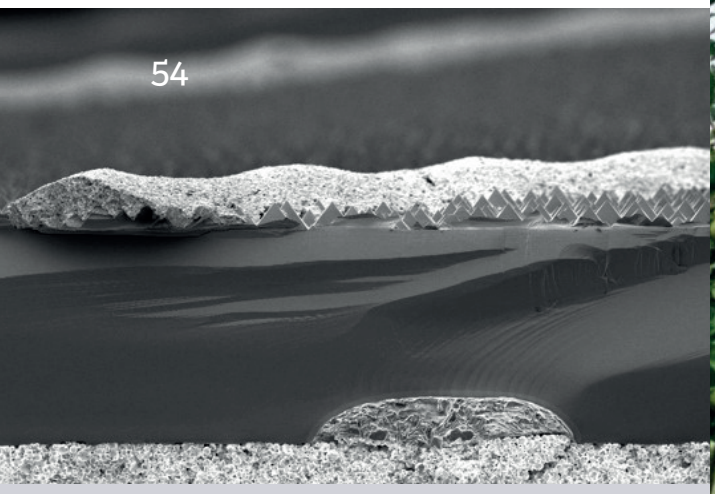



# Contents


Section 1: **PV Modules**

**8** The challenge of measuring busbarless solar cells and the impact on cell-to-module losses

*Michael Rauer, Alexander Krieg, Andrea Pfreundt, Max Mittag & Sebastian Pingel, Fraunhofer Institute for Solar Energy Systems ISE, Freiburg, Germany*

**19** Do we really understand the failure mechanism of a PERC cell?

*Haidan Gong[1], Minge Gao[1], Yiwei Guo[1], Jian Wang[1], Xiaogang Zhu[2], Jiayan Lu[2], Shan Yanyan[2] & Yi Liu[2]*

*[1]Wuxi Suntech Power Co., Ltd.; [2]National Center of Supervision & Inspection on Solar Photovoltaic Products Quality (CPVT), Wuxi, Jiangsu, China*

Section 2: **Thin Film**

**29** Both sides now: Optimal bifaciality with silicon heterojunction solar cells

*Adrien Danel, Julien Eymard, Vincent Barth, Mathieu Tomassini, Eric Gerritsen, Armand Bettinelli & Charles Roux, CEA, LITEN, Department of Solar Technologies, INES, Grenoble, France*

**40** tandemPV: A review of c-Si-based tandem technology and what is needed to bring it into production

*Radovan Kopecek[1], Lejo J. Koduvelikulathu[1], Daniel Tune[1], Dan Kirk[2], Chris Case[2], Michael Rienäcker[3], Henning Schulte-Huxel[3], Emily Warren[4], Adele Tamboli[4], Robby Peibst[3], Bart Geerligs[5], Sjoerd Veenstra[6] & Gianluca Coletti[5,7]*

*[1]ISC Konstanz, Germany; [2]OxfordPV, Brandenburg an der Havel, Germany; [3]ISFH, Emmerthal, Germany; [4]NREL, Golden, Colorado, USA; [5]TNO Energy Transition, Solar Energy, Petten, The Netherlands; [6]TNO Energy Transition, partner in Solliance, Eindhoven, The Netherlands; [7]School of Photovoltaic and Renewable Energy Engineering, UNSW, Sydney, Australia*

Section 3: **Cell Processing**

**54** Industrial PERC+ solar cell efficiency projection towards 24%

*Thorsten Dullweber, Maximilian Stöhr, Christian Kruse, Felix Haase, Birgit Beier, Philip Jäger, Verena Mertens, Robby Peibst & Rolf Brendel, Institute for Solar Energy Research Hamelin (ISFH), Emmerthal, Germany*

**64** Towards 24% efficiency for industrial n-type bifacial passivating-contact solar cells with homogeneous emitter

*Jie Bao, Cheng Chen, Ronglin Liu, Zhencong Qiao, Zheren Du, Zhifeng Liu & Jia Chen, Jolywood Solar Technology Co. Ltd., Taizhou City, Jiangsu Province, China*

**73** monoPolyTM to biPolyTM: Low-cost passivating contact technologies for efficiencies above 24%

*Naomi Nandakumar, Pradeep Padhamnath & Shubham Duttagupta, Solar Energy Research Institute of Singapore (SERIS), National University of Singapore (NUS)*

**78** Subscription / Advertisers Index

SERAPHIM®

# SERAPHIM SIII SERIES HALF-CELL MODULE

## 445W maximum power output
## 20% maximum module efficiency

Due to the significant improvement in efficiency, the application of Seraphim SIII series half-cell module can significantly reduce levelized cost of electricity (LCOE), balance of system (BoS), EPC (Engineering Procurement Construction) and land costs in large industrial/commercial and ground power stations.

***SHIFTING*** · THE FUTURE

*www.seraphim-energy.com* | *info@seraphim-energy.com*

# The challenge of measuring busbarless solar cells and the impact on cell-to-module losses

Michael Rauer, Alexander Krieg, Andrea Pfreundt, Max Mittag & Sebastian Pingel, Fraunhofer Institute for Solar Energy Systems ISE, Freiburg, Germany

## Abstract

The realistic measurement of solar cells is key for the whole PV industry, as accurate information about cell power is one of the most important aspects in solar cell purchase and PV module design. The omission of busbars introduces new challenges to the current–voltage measurement of solar cells, since contact to every single grid finger has to be established with independent current and voltage contacts. It is not just the shadow correction of the measurement unit that needs to be carried out more laboriously, but also the contacting of the front metal grid, which is more critical because of the high resistivity of the grid fingers. The position of the voltage sensing contact and the number of current contacts can thus have a noticeable impact on the measured performance of busbarless solar cells. Measured efficiencies are highly dependent on the contacting schemes used in different measurement systems, as these vary in contact number and sensing configuration. Two different main approaches for measuring busbarless solar cells have evolved, representing either realistic or idealized application of the cells in the module. The pros and cons of both approaches are discussed in detail in this paper. *Realistic* measurement conditions lead to efficiencies which best predict module performance, but are hard to realize and require knowledge about the subsequent module design. Although not their primary purpose, the use of *idealized* measurement conditions can make it easier to achieve record cell efficiencies, but with the disadvantage of limited comparability with busbar-based solar cell concepts. Idealized conditions can moreover lead to hidden losses in performance of the solar cells, related to the application in a module, which in turn causes inflated cell-to-module (CTM) losses. If solar cells are bought in terms of $/Wp and modules are sold likewise, the economic implications arising from the different measurement configurations have to be considered. Whichever approach is used for the measurement of busbarless solar cells, full disclosure of the measurement configuration is absolutely essential.

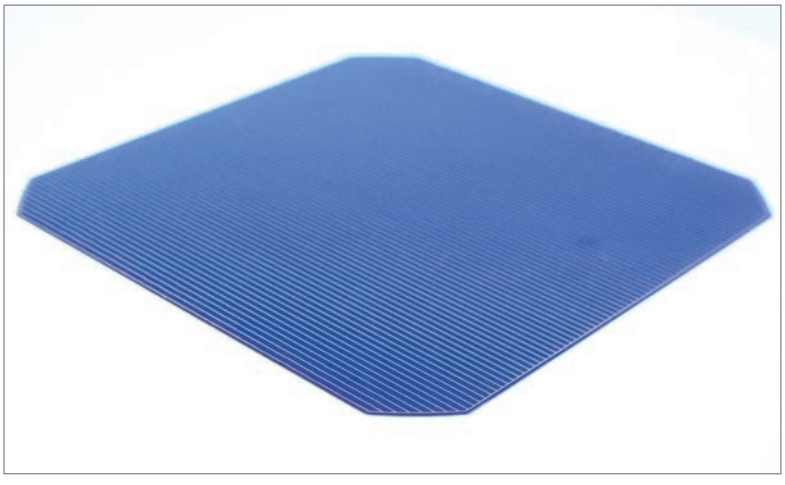

**Figure 1. Industrial busbarless silicon solar cell.**

## Introduction

In the last few years, there has been huge progress in screen-printing technologies with regard to reducing finger widths [1]. To keep the series resistance losses resulting from increased finger resistivity low, the number of busbars has continuously increased and their width decreased, with multi-busbar concepts becoming mainstream [2]. The next step in this evolution is to omit busbars entirely (Fig. 1). Interconnection between metal grids is no longer realized by means of interconnectors soldered to busbars, as has been done until recently, but is outsourced to the module level. Tabs or wires are either soldered or glued directly to the fingers [3,4], or wires embedded in adhesive foils are soldered to the solar cells [5]. The cost savings realized through reducing the amount of silver per cell is also driving this evolution. Although the market share of busbarless solar cells is still limited, it is predicted to increase to over 30% in the next ten years [2].

The evolution to busbarless solar cells is accompanied by new challenges in manufacturing as well as in quality testing. The most important test by far is the measurement of the current–voltage (*I–V*) characteristics, which is a key driver for the determination of solar cell selling price, and is used for sorting the solar cells into different bins according to current or power for the subsequent module interconnection. For this measurement, temporary contacts for current extraction and voltage measurement have to be applied to the solar cells.

For conventional solar cells, well-established contacting methods are available and specified in international standards [6]. Contacting is thereby oriented towards the idealized integration of the solar cells into a module: it requires that a constant potential over the entire busbars is realized, which corresponds to an infinitely conductive interconnector. In practice, this is realized by applying a sufficient number of current contacts [7] or by smart voltage sensing at the average voltage of the potential distribution [8,9]. Moreover, the shadow caused by the contact units needs to be eliminated, which is mainly for reasons of reproducibility. Sun simulators used throughout the PV community exhibit different light divergence. The contact units therefore cast different shadows on different simulators. Without shadow correction,

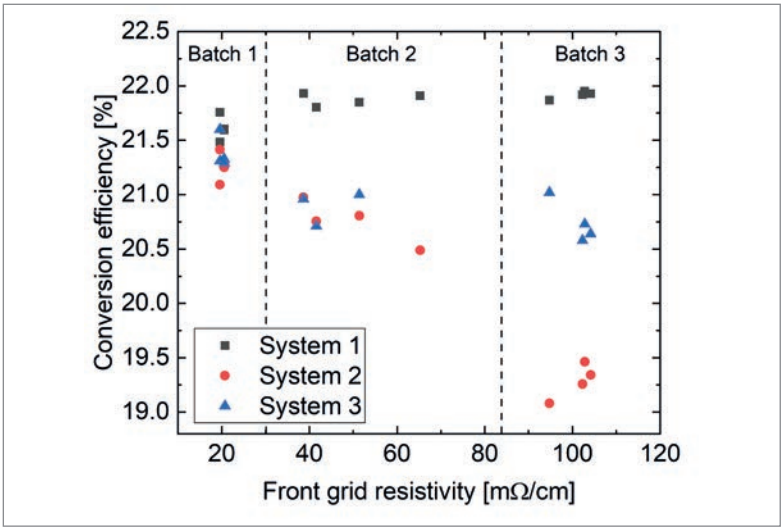


**Figure 2. Measured conversion efficiency $\eta$ for industrial silicon heterojunction (SHJ) solar cells with different front-grid resistivity ranges. Three different commercially available systems were used for the measurements.**

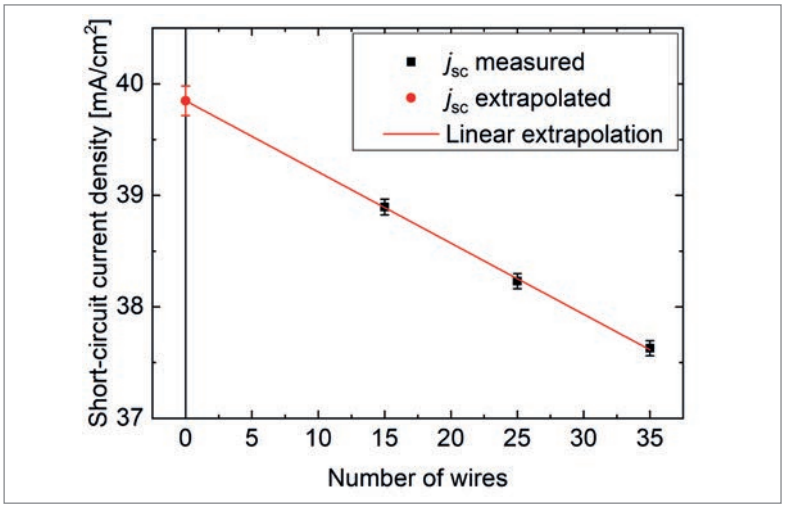


**Figure 3. Short-circuit current density $j_{sc}$ of a busbarless cell measured with different numbers of contact wires. The shadow-free $j_{sc}$ can be determined by linear extrapolation to zero wires.**

this could lead to false calibration of solar simulators and erroneous sorting of solar cells, if the calibration laboratory simulator and the production line *I–V* tester exhibit different divergences. The established way of measuring cells therefore corresponds to an ideal interconnector without any shadow. The losses occurring from realistic interconnection ribbons that cast a specific shadow contribute to the so-called *cell-to-module (CTM) ratio* [10,11]. Since the shadowing losses of interconnectors are considered in CTM analyses, cell measurements require either the shadow correction in order to avoid a double consideration of interconnector shading, or a cell measurement that exactly replicates the interconnectors as used in module integration, which is unrealistic because of the wide variety of module designs.

For busbarless solar cells, things are considerably less clear and less established. Although several different measurement systems are available on the market [12–16] or have been presented by research institutes [17,18], no common procedure for the measurement of busbarless solar cells has evolved so far. The contacting schemes realized in the systems can be very different. For some systems, only current contacts are applied to the solar cells, and the voltage is measured on the current contact bars. For other systems, both current and voltage contacts are realized on the metal grid of the solar cells, but the positioning of these contacts relative to each other can be very different from system to system. Furthermore, the systems also vary in the number of current contacts to the solar cells. All these aspects strongly affect the *I–V* measurement results, and the effect intensifies with increasing resistivity of the metal grid [19]. Fill factor (*FF*) values in particular – and thus efficiency values $\eta$ – can vary considerably and depend on the system used for the measurement.

As there are so many different ways to perform *I–V* measurements, this unavoidably leads to the question as to which particular value of efficiency of busbarless solar cells can be considered the most meaningful. This paper therefore discusses deviations in *I–V* parameters by applying different contacting schemes, and gives background information on shadow correction and contacting of busbarless solar cells. The comparability with conventional, busbar-based solar cell concepts is also analysed. The implications of different measurement approaches for CTM losses are then addressed. Finally, the question of what might be the most relevant efficiency of busbarless solar cells is discussed and recommendations are given.

## Measurement systems for busbarless solar cells

To investigate the influence of the contacting scheme on the performance of busbarless solar cells, the *I–V* characteristics of industrial bifacial busbarless silicon heterojunction (SHJ) solar cells were measured using three different industrial, commercially available systems. To further evaluate the effect of the resistivity of the front grid, solar cells with three different grid resistivity ranges were used. The measured conversion efficiencies of the SHJ cells are shown in Fig. 2. Note that the solar cells of the different resistivity groups originate from different production batches, which are based on very similar fabrication processes but vary slightly in rear-grid resistivity. The different groups can therefore not be directly compared with each other. A comparison of the measurement systems within a given group is, however, very conclusive.

Clearly, the difference in measured efficiency within a given group highly depends on the measurement system used. For low grid resistivity, the difference in $\eta$ between the systems is relatively small; however, the higher the grid resistivity, the larger the difference becomes.

This brief experiment shows that the choice of measurement system can significantly affect the measured performance of busbarless solar cells. In the

"No common procedure for the measurement of busbarless solar cells has so far evolved."

following section, the background to this effect is discussed in detail.

## Complexity of measuring busbarless solar cells

This section will provide insight into the complexity of measuring busbarless solar cells. It will deal with how measurement results need to be assessed, particularly in comparison to conventional, busbar-based solar cells.

### Shadow correction of the measurement unit

For conventional solar cells with busbars measured at calibration laboratories, correction of the shadow by the contact unit is generally done by means of measurements with Kelvin probes [7,9,20]. These probes contact the busbars only at the rim and cast negligible shadow. This way, the shadow-free short-circuit current density $j_{sc}$ of the solar cells can be easily measured.

For busbarless solar cells, however, the above well-established procedure cannot be used, because there are no busbars for contacting with the Kelvin probes. Instead, the shadow-free $j_{sc}$ needs to be determined by varying the number of contact bars or wires, which is more laborious. Fig. 3 shows the $j_{sc}$ values measured using a wire-based contact unit and different numbers of wires. Since each wire casts a certain amount of shadow onto the solar cell, the measured $j_{sc}$ decreases when the number of wires increases. By linear extrapolation to zero wires, the shadow-free $j_{sc}$ can then be determined.

For monocrystalline solar cells with pseudo-square rounding of the edges, the area covered by the wires may be a more precise measure for the shadow than merely the number of contacts.

### Influence of the voltage sensing position

Contacting busbarless solar cells is, from a metrology point of view, much more complex than contacting conventional solar cells with busbars. For busbarless solar cells, the contacting unit not only needs to ensure contact to every single grid finger, but also needs to provide independent current and voltage contacts, which are ideally located directly on the metal grid.

The positioning of the current and voltage contacts significantly affects the measured *I–V* characteristics [8,19]. Fig.4(a) shows a schematic of the contacting situation: the finger collects the current from the photoactive area and conducts it to the current contact. The cumulative current in the finger thus increases towards the current contact and is highest directly at the contact. As the finger exhibits a distinct resistivity, the current flow leads to a voltage drop along the finger. Fig. 4(b) shows voltage distributions in the finger, which have been iteratively calculated using a model of independent diodes interconnected by resistors [19] for the industrial SHJ solar cells measured in the previous section. Different voltage sensing positions were considered for the calculations, as well as a grid resistivity of 50mΩ/cm (finger resistivity of 4.0Ω/cm) and nine current contact wires or bars over the

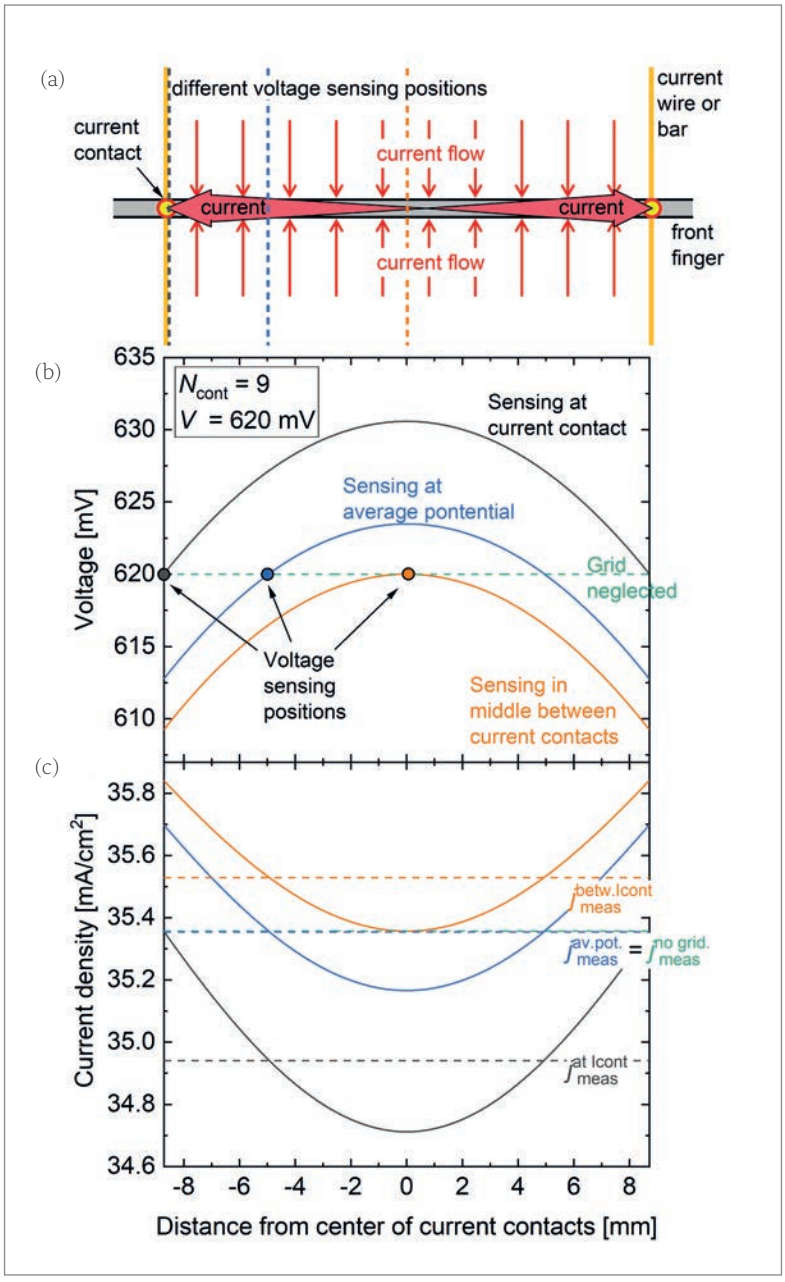


**Figure 4. (a) Schematic contacting of a grid finger with current wires or bars. A perpendicular current flow into the finger is assumed, which leads to an increase in cumulative current towards the current contact. The dashed lines represent three different voltage sensing positions. (b) Calculated voltage distributions in the contact finger (finger resistivity of 4Ω/cm, grid resistivity of 50mΩ/cm) for the three different voltage sensing positions. The measured voltage is the same for all configurations and is close to the maximum power point. (c) Calculated current density distribution for the different sensing configurations. The current density measured at the current contact is the average over the distribution and is indicated by the dashed lines.**

solar cell. For simplicity, the solar cells were assumed to be monofacial with a fully metalized rear. For the distributions shown in Fig. 4(b), it is assumed that the voltage source is set to the same voltage, so that a voltage of 620mV is measured at the voltage contact for all sensing configurations, i.e. one distinct voltage point on the *I–V* curves was regarded. This voltage is close to the maximum power point (mpp).

"Contacting busbarless solar cells is, from a metrology point of view, much more complex than contacting conventional solar cells with busbars."

The voltage distributions in the fingers generally exhibit a parabolic form, which results from the product of a – by first approximation – linear increase in cumulative current in the finger and a linear increase in finger resistance. The dashed green line additionally shows the distribution for the case when the resistance of the front grid is set to zero; this is referred to as the *grid-neglected* case, which leads to a flat distribution with homogeneous potential in the finger.

Although the voltages measured at the external voltage contact are identical for all sensing configurations, it is evident that the voltage distributions in the finger are very different. This also affects the current density distributions in the fingers, which are shown in Fig. 4(c). The current density measured at the external current contact is not the one occurring locally at the current contact, but the average over the entire distribution in the finger [8,19]. The dashed lines in Fig. 4(c) show that the measured current densities differ significantly for the different voltage sensing positions. This means that, although the measured voltages are the same, the measured current densities are highly dependent on the voltage sensing scheme.

For sensing at the current contact, the measured current density is lower than that measured for the grid-neglected case. This holds true not only for $V$ = 620mV but for all voltage points of the mpp region, which is shown in Fig. 5. The voltage points of the *I–V* curves around the short-circuit and open-circuit points are not affected, as there is no slope of the *I–V* curve and no current flowing, respectively. The effect of reduced current densities in the mpp region is known as a *distributed series resistance* of the finger grid [21,22] and reduces the measured *FF*. For sensing in the middle, between two current contacts, the current density in the mpp region is higher than that for the grid-neglected case; correspondingly, the measured *FF* is higher as well.

As Fig. 4 shows, there is one specific voltage sensing position, which is at approximately 22% of the distance between two current contacts [8], for which the measured current density equals the current density of a grid-neglected measurement. Setting the voltage contact to this position therefore corresponds to a measurement to which the resistivity of the front metal grid does not contribute. The *FF*s measured with this sensing configuration and with negligible metal grid resistivity are thus identical. This sensing position represents the position of the average voltage distribution, so that the averages of voltage and current distributions are measured by the voltage and current contacts, respectively.

These explanations show that the choice of voltage sensing scheme significantly affects the measured solar cell performance. It is important to note that the strong influence of the sensing positions on the measured *I–V* parameters is mainly caused by the fact that the resistivity of the fingers is orders of magnitude higher than the resistivity of the busbars.

### Influence of the number of current contacts

The differences in *FF* – and in efficiency $\eta$ – between the sensing positions discussed above intensify with increasing grid resistivity (linearly by first approximation) and with increasing distance between the current contacts (quadratically by first approximation). Therefore, the impact of the sensing position is noticeably greater for a small number of current contacts and less pronounced for a larger number. This can be seen in Fig. 6, in which *FF* and $\eta$ are shown as functions of the number of current contacts. For sensing at the current contact, *FF* and $\eta$ increase with increasing numbers of contacts because the influence of the distributed series resistance decreases. For sensing in the middle, between the current contacts, the overestimation of *FF* and $\eta$ is higher when there are fewer contacts, and decreases when the contact number increases. Sensing at the average potential in turn leads to *FF* and $\eta$ measurements that are independent of the number of contacts. With this configuration, the grid-free *I–V* parameters are always measured.

For large numbers of contacts, the three curves converge, as the voltage distribution in the fingers becomes so small that different sensing positions have negligible effects on the measurement. The convergence, however, is dependent on the grid resistivity: the spread of the curves increases considerably for higher grid resistivity, so that convergence occurs at larger numbers of contacts.

How does this impact the validity and assessment of measurement results of busbarless solar cells? Although the solar cell parameters used for the calculations are identical for all measurement configurations, the measured efficiencies can be very different and depend on the number of current contacts and the sensing design used. This explains why the different measurement systems from the previous section yield widely different results, and why the difference between them depends very much on the grid resistivity of the solar cells. For those solar cells, the effect is even twice as great, as it occurs on both the front and the rear side. Higher cell efficiencies therefore do not necessarily mean that the solar cells perform better – it could be that a different system was used for the measurement. For the sake of comparability, it is thus recommended to always specify the configurations used for the measurement of busbarless solar cells.

### Comparability with solar cells with busbars

Record solar cell efficiencies are essential yardsticks for highlighting outstanding achievements in solar cell research and industry. They can initiate new developments, but also decisions in opposition to apparently deficient concepts. It is therefore important to think about whether comparability exists for all solar cell concepts. In competition with conventional, busbar-based concepts, busbarless solar cell concepts in particular need to be critically assessed, given that the choice of measurement

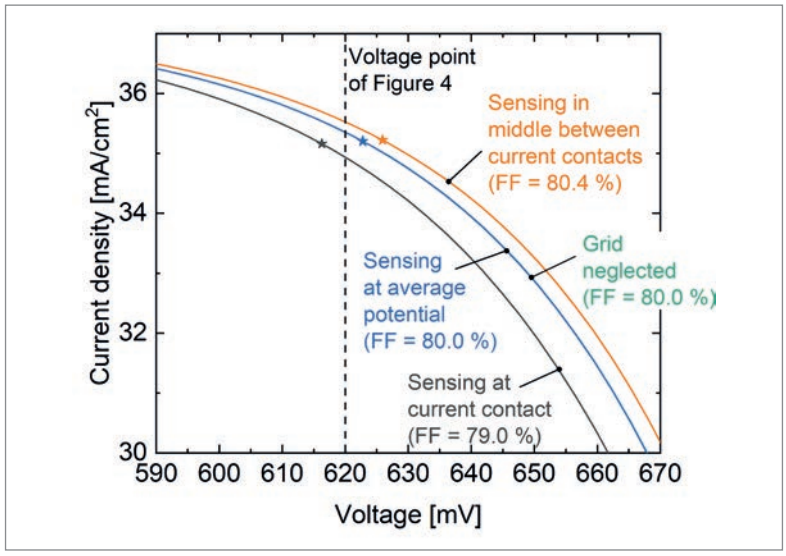


**Figure 5. Calculated *I–V* curves in the maximum power point region for different voltage sensing positions for the industrial SHJ solar cell (grid resistivity of 50mΩ/cm, nine current contacts). The dashed black line represents the voltage point for which the voltage and current density distributions in a grid finger are shown in Fig. 4. The voltage regions around short circuit and open circuit are not affected by the voltage sensing position. The stars indicate maximum power points.**

"The choice of voltage sensing scheme significantly affects the measured solar cell performance."

system has such a big impact on the measurement results of busbarless solar cells.

Further studies of the SHJ solar cells were therefore carried out. Front-grid resistivities in the range 5–100mΩ/cm were considered, and different busbar-based and busbarless configurations investigated: for the conventional solar cell concept with six busbars, a busbar shading of $1.1\%_{rel}$ (corresponding to a busbar width of 300µm) and shading by the finger grid were taken into account. Current and voltage sensing was implemented at the busbars, in conformance with IEC standards (Fig. 7(a)). For the busbarless solar cell concepts, only the shading of the finger grid was accounted for (Fig. 7(b–e)). Various sensing configurations were considered, ranging from six current contacts (b) and (c), to 30 current contacts (d) and (e), additionally assuming different voltage sensing positions. Measurement configurations (a) and (b) in Fig. 7 allow a direct comparison to be made of busbar-based and busbarless solar cell concepts with similar contacting schemes. The number of current contacts is assumed to be identical, as is the voltage sensing – only the extent of shading differs. Both measurement configurations are oriented towards the interconnection of the solar cells in the module, and thus represent *realistic* contacting conditions.

As Fig. 7 shows, the measured efficiency is very much dependent on the grid resistivity for both measurement configurations. Because of the sensing at the current contact, the distributed series resistance of the metal grid contributes for both configurations. Higher efficiencies are measured for the busbarless concept: the difference in $\eta$ amounts to as much as $1.1\%_{rel}$ for all grid resistivities, which is exactly the same as the shading percentage of the busbars.

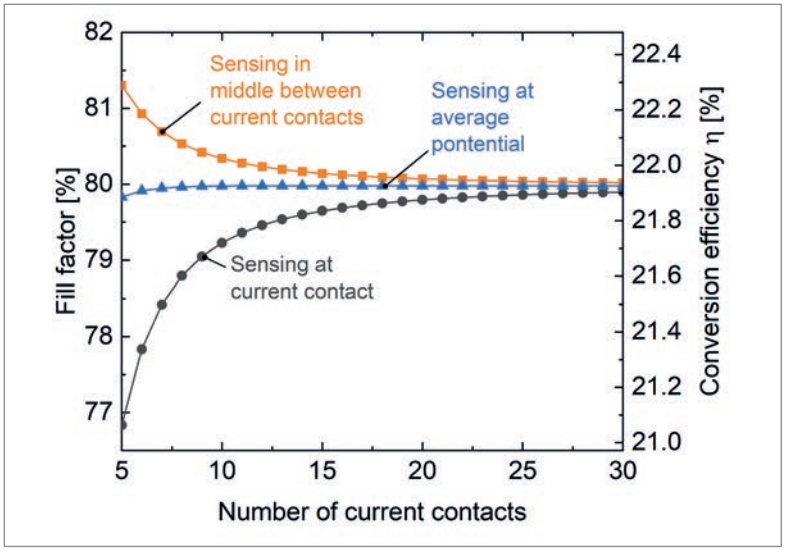


**Figure 6. Calculated *FF* and *η* for an industrial SHJ solar cell (grid resistivity of 50mΩ/cm), measured with a wire-based contacting unit, as a function of the number of current wires. The different colours represent the different voltage sensing positions discussed earlier. Note that for other grid resistivities, the influence of the sensing position can be smaller or larger.**

For the other busbarless measurement configurations (c–e), the efficiency of the busbarless solar cells is measured to be higher. By either sensing the voltage at the average potential (c), or applying a large number of current contacts (d) and (e), the influence of the distributed series resistance of the finger grid is minimized. The measured efficiencies depend only slightly on grid resistivity. The measurement configurations (c–e) thus represent *idealized* contacting of busbarless solar cells, or scenarios where module integration is performed using an untypically large number of interconnectors. The difference in efficiency when compared with conventional, busbar-based solar cells (configuration (a)) is heavily dependent on grid resistivity: whereas the difference for low grid resistivity is only caused by busbar shading, the additional contribution of the distributed series resistance significantly increases with higher grid resistivity. Most of the difference is then caused by the series resistance of the front grid.

In conclusion, higher efficiencies are measured for busbarless solar cell concepts than for conventional, busbar-based concepts – how much higher depends not only on busbar shading and grid resistivity, but also on the contacting scheme used for the measurement. Manufacturers and researchers therefore need to be aware of how to assess and compare the efficiency values reported for busbarless solar cells with each other, and especially with the efficiency values of conventional solar cells.

Measuring a high efficiency at the solar cell level does not automatically mean that the solar module assembled from these cells will also have a similar high efficiency. If the cell efficiency is overrated with regard to module application, the CTM loss will be considerably affected. This issue will be discussed in more detail in the following section.

"Higher cell efficiencies do not necessarily mean that the solar cells perform better – it could be that a different system was used for the measurement."

## Implications for CTM losses

In order to estimate the power of a solar module assembled using the industrial SHJ solar cells, the sophisticated calculation software SmartCalc.CTM [11,23] is applied. This software uses *I–V* parameters and spectrally dependent reflectance and quantum efficiencies of the solar cells, as well as geometric specifications of the cells, interconnectors and solar module stack as input data. A virtual twin of the solar module is created which can be analysed with respect to optical, electrical, thermal and geometrical loss channels.

### Model for calculating CTM losses

The solar cell specifications used for the CTM calculations are based on the same industrial SHJ solar cells examined in the previous sections. Spectral reflectance and quantum efficiencies are taken from measurements, and the *I–V* parameters are determined using the independent diode model. Different front-grid resistivities, ranging from 5 to 100mΩ/cm, were again considered, as well as the different sensing configurations in Fig. 7. For the conventional solar concept with six busbars, busbar widths of 300µm were again assumed. For larger numbers of busbars, a realistic grid layout consisting of 20 pads per busbar and a supporting grid line with a width of 100µm in between was employed. In order to be sensitive to the effects of front contacting only, all solar cells were considered to be monofacial.

For solar cell interconnection, advanced interconnector specifications were used: for the conventional solar cell concept with six busbars, rectangular, coated copper ribbons with a width of 0.6mm and a height of 0.25mm were utilized. For the busbarless solar cell concept with six interconnectors, six wires with a diameter of 0.4mm were assumed. In the case of solar cells with a larger number of interconnectors, wires with a slightly reduced diameter of 0.35mm were employed.

Typical module specifications were used: the module contains 60 solar cells, a polyolefin encapsulant, an aluminium backsheet and low-iron glass with an anti-reflective coating and a thickness of 3.2mm. The module dimensions are 1.70 × 1.00m$^2$.

With the use of these data, the optical and electrical gains and losses are calculated and the module power predicted. The CTM power ratio is calculated by comparing the module power with the summed power of the solar cells. CTM values greater than 100% represent a power gain of the solar cells as a result of module assembly with respect to the cell measurement, while values less than 100% represent a power loss.

### CTM losses for six interconnectors

Fig. 8 shows the calculated CTM power ratios for the industrial SHJ solar cells with six interconnectors

SNEC
PV POWER EXPO
Dialogue & Conference & Exhibition

www.snec.org.cn

# SNEC 15th (2021) International Photovoltaic Power Generation and Smart Energy Exhibition & Conference

## 2021 | June 3-5

## Shanghai·China

*Venue: Shanghai New International Expo Center (SNIEC)*

SNEC Homepage

◎Asian Photovoltaic Industry Association / Shanghai New Energy Industry Association

◎Show Management: Follow Me Int'l Exhibition (Shanghai), Inc.

Add： RM905-907 No 425 Yishan Rd, Xuhui District, Shanghai 200235, PRC

Tel： +86-21-33685117 / 33683167

◎For exhibition: info@snec.org.cn For conference: office@snec.org.cn

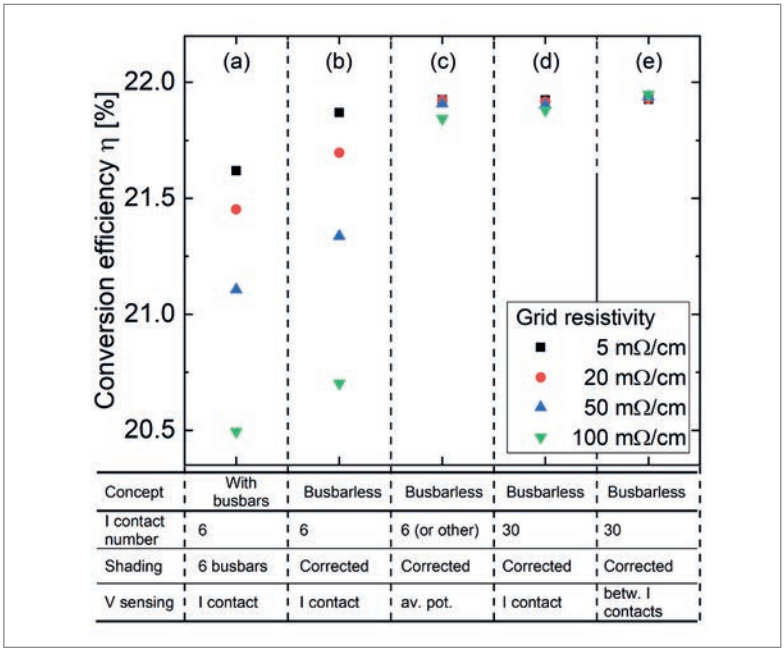


**Figure 7. Calculated conversion efficiencies $\eta$ for industrial SHJ solar cells with front-grid resistivities in the range 5–100mΩ/cm. Different measurement configurations were assumed, representing the same solar cell with (a) six busbars or (b–e) without busbars. For the busbarless configurations, different numbers of current contacts and voltage sensing positions were considered.**

and the busbar concepts and measurement configurations detailed in the previous section.

Solar modules assembled from solar cells of a certain grid resistivity yield practically the same power, no matter what the value of efficiency measured by the cell measurement. Only small differences between busbar-based and busbarless concepts result from slightly different optical and resistive losses. The solar module power is therefore nearly independent of the cell measurement configurations, and only depends on the grid resistivity: the module power decreases almost linearly with increasing grid resistivity as a result of the increasing distributed series resistance of the grid. Because the measured cell power is highly dependent on the cell measurement configurations (which are affected by the grid resistivity in different ways), the CTM ratios are significantly affected by the cell measurement configurations as well.

Configuration (a) in Fig. 8 represents a conventional solar cell concept with six busbars, configurations (b–e) busbarless solar cell concepts with different numbers of current contact and different voltage sensing position. It can be seen that all solar cell concepts suffer a loss in power as a result of module assembly, chiefly caused by optical losses – such as shading of the active solar cell area by the interconnectors, and front glass reflection – but also by ohmic losses within the interconnectors. The exact extent of the CTM loss depends very much on the specific measurement concept, the grid resistivity and interconnector design.

"Measuring a high efficiency at the solar cell level does not automatically mean that the solar module assembled from these cells will also have a similar high efficiency."

The conventional, busbar-based solar cell concept has CTM ratios closest to unity of all configurations. For this configuration, the measured solar cell power gives a significant and reliable prediction of the later module power. The CTM ratios are particularly not dependent on the grid resistivity, as the resistive losses of the front grid of the solar cells in the module are correctly considered by the cell measurement. Since the busbar already shades active solar cell area, additional shading from the rectangular interconnector ribbons protruding from the busbars is limited in module integration: parts of the shading loss are already incorporated in the cell measurement. Therefore, a higher CTM ratio is achieved.

The module power decreases with increasing grid resistivity because of the increasing distributed series resistance of the grid. Solar cell measurements with more *realistic* sensing conditions (b) consider this increasing resistive loss, so that the CTM ratio is virtually independent of the grid resistivity. Since the number of wires is the same in cell characterization and module integration, the grid losses are already incorporated in the cell characterization. Solar cell measurement and module output show the same decrease in power with increasing grid resistivity. As the cross sections of the interconnecting wires are smaller than the cross sections of the rectangular ribbons, the CTM ratios are further reduced because of resistive losses. Additionally, shading of active solar cell area, which is not taken into account in the cell measurement, leads to reduced CTM ratios. However, as the optically relevant diameter of the wires is only 60% of the total diameter because of reflection to the solar cell surface [24], this decrease is small. Realistic cell measurement configurations can therefore predict module performance fairly reliably.

Solar cell measurements with *idealized* sensing have yielded efficiencies that are almost independent of grid resistivity, because the influence of the distributed series resistance of the grid has been minimized by adapted contacting or voltage sensing. This now has a significant effect on the CTM ratios for these measurement configurations (c–e). For low grid resistivity, the resistive grid losses are small and only wire shading prevails. The CTM ratios are thus close to the measurements obtained with realistic sensing configurations. For high grid resistivity, however, the contribution of the distributed series resistance increases more and more. The CTM ratios thus decrease almost linearly to fairly low values with increasing grid resistivity. Idealized cell measurement configurations therefore provide a rather poor and unreliable estimate of the performance of the cells in a module.

### CTM losses for a larger number of interconnectors

For higher grid resistivity, it is often beneficial in terms of module performance to increase the number of interconnectors. An additional analysis was

therefore performed to assess the influence of the number of interconnectors on the CTM ratio. Fig. 9 shows the corresponding results for both realistic and idealized measurement of busbarless solar cells.

In the case of the realistic measurement configuration (b), the CTM ratios are virtually independent of the number of interconnectors and the grid resistivity, since cell measurements and module output power are similarly affected by resistive grid losses. For larger numbers of interconnectors, the loss caused by shading of interconnectors in the module, which increases quadratically with the shading fraction, becomes significant and the CTM is slightly reduced. The realistic cell measurement configuration reliably predicts module performance for various numbers of interconnectors and grid resistivities.

The CTM ratio for the idealized measurement configuration (e) is affected by two contrasting contributions: on the one hand, the resistive grid losses (which are not detected by cell measurement) decrease for increasing number of interconnectors, while, on the other hand, the shading losses increase. For low grid resistivity, shading losses prevail and the CTM ratios decrease with increasing number of interconnectors. For high grid resistivity, however, resistive losses are dominant and the CTM ratios are higher when more interconnectors are used. Although the quality with which the module performance is predicted by this idealized measurement configuration improves for a larger number of interconnectors, it is highly dependent on the number of interconnectors and on grid resistivity. Module power output is therefore only predicted to a limited extent by idealized cell measurements.

## The best way to measure busbarless solar cells

The range of possibilities for measuring busbarless solar cells raise the question as to what the most meaningful way of measuring these solar cells actually is. Two main approaches have become apparent from the above discussions: measuring busbarless solar cells according to (1) realistic or (2) idealized module application.

### (1) Measurements according to realistic module application

Measurements according to realistic module application means that the number of current contacts should be chosen identical to that of the later module application; for example, solar cells intended for interconnection with, say, 12 wires should also be measured using 12 current contacts. Voltage sensing should be carried out at the current contact in order to fully consider the distributed series resistance of the grid. Shading by the contact units should be corrected: although the obvious differences between busbar-based and busbarless concepts fuel the discussion about whether shading by contact bars or wires should be taken into account, in the authors' opinion the comparability

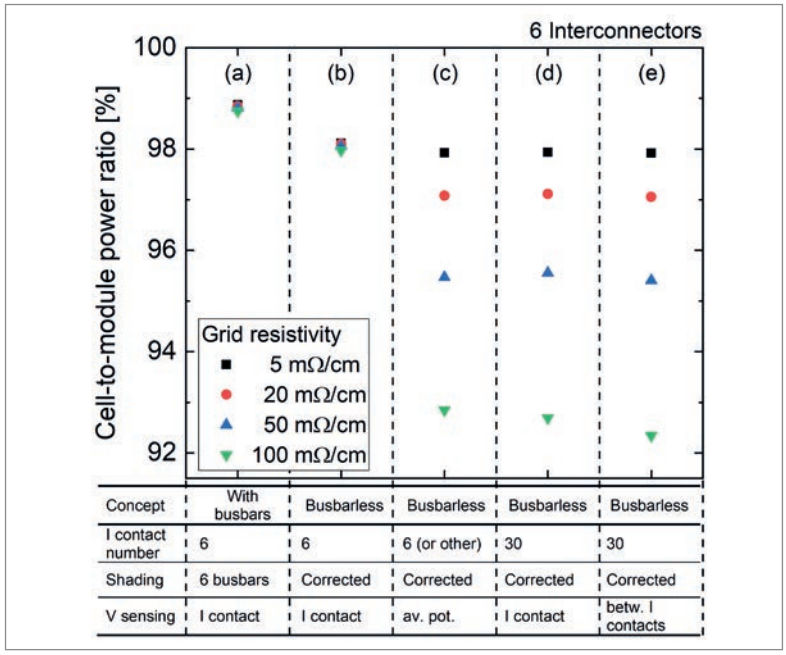


**Figure 8. Calculated CTM power ratios for industrial SHJ solar cells with front-grid resistivities ranging from 5 to 100mΩ/cm, assembled in modules with six interconnectors. The configurations in Fig. 7 were used for contacting and voltage sensing.**

"Realistic cell measurement configurations can predict module performance fairly reliably, whereas idealized configurations provide a rather poor and unreliable estimate."

of measurement results between different solar simulators needs to be ensured (dependence on the divergence). This can best be realized by correcting for shading. Moreover, and most importantly, the majority of measurement systems bear no resemblance whatsoever with interconnectors in the module and cast a very different shadow.

The *I–V* parameters of busbarless solar cells measured this way provide the best approximation of the values that can be expected in the module, because the CTM losses are minimized. However, the exact same cell can exhibit very different efficiencies depending on how the cell is integrated in the module. Moreover, how the cell will be interconnected in the module must already be known before the measurement of the cell takes place, which is not always the case. This approach furthermore poses tremendous requirements on measurement equipment, as various module layouts may need to be contemplated.

Implementing this measurement approach is rather complicated. To the authors' knowledge, there is currently no system commercially available on the market with current and voltage contacts located directly on the solar cell grid which are electrically isolated but close to each other. The complexity lies in the high finger resistivity, which requires either very low distances of the order of 100µm or less between adjacent current and voltage contacts, or the realization of isolated current–voltage–current contact triplets [19].

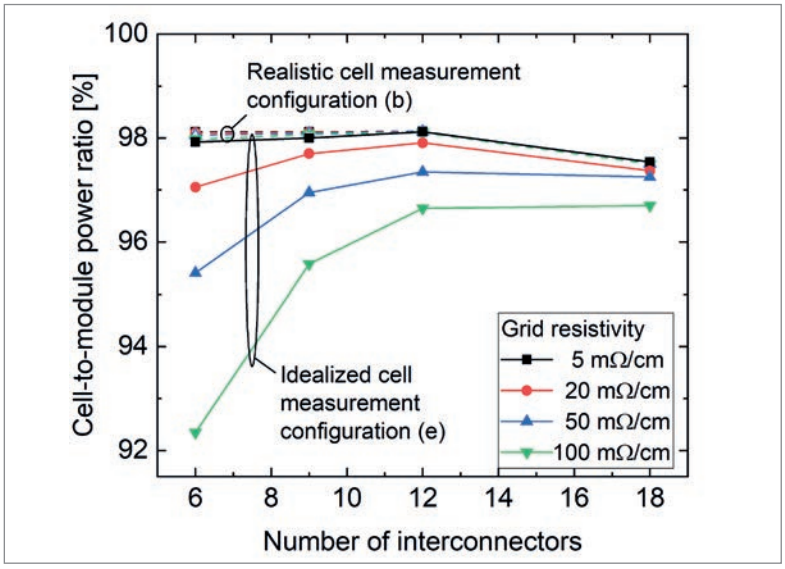


**Figure 9. Calculated CTM ratios as a function of the number of interconnectors, for busbarless SHJ solar cells measured with a realistic configuration (b) (open symbols) and with an idealized configuration (e) (closed symbols). Different front-grid resistivities ranging from 5 to 100mΩ/cm were considered. In configuration (b), the number of current contacts for the measurement was assumed to be equal to the number of interconnectors in the module.**

### (2) Measurements according to idealized module application

In idealized conditions, busbarless solar cells should be measured either with a large number of current contacts or with voltage sensing at the average potential. This way, the front-grid resistivity does not contribute to the measurement. Shading by the contact unit needs to be corrected. This measurement configuration thus resembles an idealized module interconnection with a large number of shadow-free contacts.

There are several systems available on the market that are well-suited to idealized measurements. This measurement approach has the advantage that only one cell efficiency is measured which is independent of module application and quantifies the potential of the solar cell. However, the measured *I–V* parameters are the same for solar cells with different front-grid resistivities, as this resistivity is not taken into account. This poses the danger of solar cell development decoupled from module applications – at least for non-vertically integrated manufacturers. An increase in solar cell efficiency could be accompanied by a similar increase in CTM losses and a stagnation, or even a decrease, in module efficiency. Moreover, in the race for the best solar cell efficiencies, the competition between busbar-based and busbarless solar cells is rather unbalanced, as the efficiencies of busbarless solar cells are clearly inflated. In extreme cases, for record cell devices, the finger widths of busbarless cells could be designed much smaller than necessary in the module, as the resistance is not relevant.

"For both realistic and idealized approaches it is highly recommended to report not only which efficiency value has been measured for a busbarless solar cell, but also *how* it has been measured."

The comparatively high efficiencies of busbarless solar cells also need to be regarded as critical in terms of costs: non-vertically integrated module manufacturers, who purchase solar cells from a cell producer for module assembly, need to be aware that they may pay an inflated price for the solar cells. The revenue for the modules might be significantly lower because of the high CTM losses – the idealized cell measurement has concealed relevant resistive grid losses. Module manufacturers need to be aware of the measurement conditions leading to the power labelling of their solar cell purchase. A solution to this issue could be transparency of the measurement conditions and a subsequent consideration of shading and resistive losses by the calculations.

It is evident that there are advantages and disadvantages associated with the two measurement approaches, both in terms of the significance and the comparability of the measurement results, and in terms of system availability. For both realistic and idealized approaches, it is highly recommended to report not only which efficiency value has been measured for a busbarless solar cell, but also *how* it has been measured. This facilitates the assessment and interpretation of the measurement results. In any case, manufacturers and investors should be well aware that there can be hidden losses associated with busbarless solar cells.

### Acknowledgements

The work reported in this paper was partly supported by the German Federal Ministry for Economic Affairs and Energy within the framework of the BiZePS-PLUS project (Contract No. 03EE1064). The authors would like to thank K. Bothe and D. Hinken for fruitful discussions.

### References

[1] Lorenz, A., Linse, M., Frintrup, H. et al. 2018, "Screen-printed thick film metallization of silicon solar cells – Recent developments and future perspectives", *Proc. 35th EU PVSEC*, Brussels, Belgium, p. 819.
[2] VDMA 2020, "International technology roadmap for photovoltaic (ITRPV): Results 2019", 11th edn (Apr.) [https://itrpv.vdma.org/en/].
[3] Walter, J., Tranitz, M., Volk, M. et al. 2014, "Multi-wire interconnection of busbar-free solar cells", *Energy Procedia*, Vol. 55, p. 380.
[4] Geipel, T., Huq, M. & Eitner, U. 2014, "Reliable interconnection of the front side grid fingers using silver reduced conductive adhesives", *Energy Procedia*, Vol. 55, p. 336.
[5] Söderström, T., Papet, P. & Ufheil, J. 2013, "Smart Wire Connection Technology", *Proc. 28th EU PVSEC*, Paris, France, p. 495.
[6] IEC 60904-1: 2006, "Photovoltaic devices – Part 1: Measurement of photovoltaic current-voltage characteristics", 2nd edn.
[7] Hohl-Ebinger, J., Grote, D., Hund, B. et al. 2008,

"Contacting bare solar cells for STC measurements", *Proc. 23rd EU PVSEC*, Valencia, Spain, p. 2012.
[8] Kruse, C., Wolf, M., Schinke, C. et al. 2017, "Impact of contacting geometries when measuring fill factors of solar cell current–voltage characteristics", *IEEE J. Photovolt.*, Vol. 7, No. 3, p. 747.
[9] Bothe, K. & Hinken, D. 2019, "Precise and accurate solar cell measurements at ISFH CalTeC", *Photovoltaics International*, 43rd edn, p. 44.
[10] Hädrich, I., Eitner, U., Wiese, M. et al. 2014, "Unified methodology for determining CTM ratios: Systematic prediction of module power", *Sol. Energy Mater. Sol. Cells*, Vol. 131, p. 14.
[11] Mittag, M. & Ebert, M. 2017, "Systematic PV module optimization with the cell-to-module (CTM) analysis software", *Photovoltaics International*, 36th edn, p. 97.
[12] Bassi, N., Clerc, C., Pelet, Y. et al. 2014, "GridTOUCH: Innovative solution for accurate IV measurement of busbarless cells in production and laboratory environments", *Proc. 29th EU PVSEC*, Amsterdam, The Netherlands, p. 1180.
[13] Ramspeck, K., Waleska, P., Schenk, S. et al. 2019, "Contacting new solar cell metallization layouts and contact quality surveillance in solar cell production", *Proc. 36th EU PVSEC*, Marseille, France, p. 443.
[14] Kamatani, K., Fujita, Y., Takeda, Y. et al. 2019, "Development of new probe bar for c-Si PV cells with unique electrode design such as busbar-less, multi busbar and complicated busbar", *Proc. 36th EU PVSEC*, Marseille, France, p. 384.
[15] Bothe, K. 2019, "Contacting busbarless (BB0) solar cells at ISFH CalTeC, Technical information" (description of pv-tools) [https://isfh.de/wp-content/uploads/2019/12/ISFH-CalTeC_BB0Contacting_19b.pdf].
[16] INGUN Pruefmittelbau, Personal communication.
[17] Braun, S. 2014, "Simulation, Analyse und Herstellung von kristallinen Si-Solarzellen mit Multi-Busbar-Verschaltung", Dissertation, University of Konstanz, Germany, p. 108.
[18] Raj, S., Wong, J., Ramprasad, S. et al. 2018, "Effective I-V measurement techniques for busbarless and multi-busbar solar cells", *Proc. 7th WCPEC*, Waikoloa, Hawaii, USA, p. 3294.
[19] Rauer, M., Kordelos, K., Krieg, A. et al. 2019, "Accurate measurement of busbarless silicon solar cells", *Proc. 8th Worksh. Metalliz. Interconn. Cryst. Sil. Sol. Cells*, Konstanz, Germany.
[20] Geisemeyer, I., Kallies, C., Hohl-Ebinger, J. et al. 2014, "Contacting bare silicon solar cells with advanced cell metallisation", *Proc. 29th EU PVSEC*, Amsterdam, The Netherlands, p. 1202.
[21] Fischer, B., Fath, P. & Bucher, E. 2000, "Evaluation of solar cell J(V)-measurements with a distributed series resistance model", *Proc. 16th EU PVSEC*, Glasgow, UK, p. 1365.
[22] Greulich, J., Glatthaar, M., Krieg, A. et al. 2009, "JV characteristics of industrial silicon solar cells: Influence of distributed series resistance and Shockley Read Hall recombination", *Proc. 24th EU PVSEC*, Hamburg, Germany, p. 2065.
[23] Fraunhofer ISE 2020, "SmartCalc.CTM" [www.cell-to-module.com].
[24] Mittag, M., Beinert, A.J., Rendler, L. et al. 2016, "Triangular ribbons for improved module efficiency", *Proc. 32nd EU PVSEC*, Munich, Germany, p. 169.

**About the Authors**

Michael Rauer received his Ph.D. from the University of Konstanz, Germany, in 2014, in collaboration with Fraunhofer ISE. In 2015 he was awarded the SolarWorld Junior Einstein Award for his research on aluminium-alloyed contacts. He is currently working at CalLab PV Cells on the measurement of novel silicon solar cells.

Alexander Krieg studied renewable energy systems at the University of Applied Sciences Berlin and received his master's in 2007. He is currently working as a scientist in the inline solar cell analytics and simulation group at Fraunhofer ISE.

Andrea Pfreundt holds degrees in physics and nanoscience. She obtained her Ph.D. in 2015 from the Technical University of Denmark, for research on nanowire biomedical devices. In 2017 she joined Fraunhofer ISE in the module technology department, where her focus is on model development for module efficiency analysis.

Max Mittag is the head of the PV module simulation team at Fraunhofer ISE. His current work includes analysis of power losses in PV modules (cell-to-system analysis), and techno-economical assessments as well as multi-physics simulation and development of new PV module concepts.

Sebastian Pingel received his Diploma in physics in 2006 from the University of Hamburg, in collaboration with Fraunhofer ISE. He held various positions at Solon R&D, First Solar and PI-Berlin, before joining Helmholtz Center Berlin (HZB), where he started working in the field of SHJ cells. Since 2018 he has been employed as a scientist at Fraunhofer ISE.

**Enquiries**

Michael Rauer
Fraunhofer Institute for Solar Energy Systems ISE
Heidenhofstraße 2, 79110 Freiburg, Germany

Tel: +49(0)761/4588-5564
Email: michael.rauer@ise.fraunhofer.de

# Do we really understand the failure mechanism of a PERC cell?

Haidan Gong[1], Minge Gao[1], Yiwei Guo[1], Jian Wang[1], Xiaogang Zhu[2], Jiayan Lu[2], Shan Yanyan[2] & Yi Liu[2]

[1]Wuxi Suntech Power Co., Ltd.; [2]National Center of Supervision & Inspection on Solar Photovoltaic Products Quality (CPVT), Wuxi, Jiangsu, China

## Abstract

Because it leads to higher efficiencies than aluminium back-surface field (Al-BSF) cells, passivated emitter and rear cell (PERC) technology is attracting more and more attention in the industry and gaining market share. However, PERC technology brings new challenges with regard to the phenomenon of degradation: some monofacial/bifacial PERC cell modules were found to demonstrate much higher power degradation than Al-BSF cell modules after damp-heat (DH: 85°C and 85% relative humidity RH, 1000h) and potential-induced degradation (PID: 85°C and 85% RH, –1,500V, 96h) tests, which will be the focus of this paper. The power degradation of PERC cell modules after DH and PID tests was also determined to be mainly caused by a decrease in short-circuit current. For bifacial glass–glass modules, PID failure can occur under either negative or positive bias voltage, but the power degradation can be recovered after conditioning the modules in a dry-heat climate chamber at 75°C for 48h and injecting forward $I_{sc}$ current. This result indicates that such a failure does not happen outdoors, because the conditions of high heat and absence of current do not occur in the field. Consequently, the deviations of standard IEC conditions from real field conditions might lead to drawing the wrong conclusions from lab test results.

## Introduction

Passivated emitter and rear cell (PERC) modules, because they demonstrate higher efficiency than aluminium back-surface field (Al-BSF) cell modules, are attracting more and more attention in the industry and starting to become a more promising candidate for reducing the levelized cost of electricity (LCOE). Furthermore, bifacial PERC modules fabricated using a glass–glass or glass–white backsheet configuration, which can lead to a higher power gain than that of monofacial PERC cell modules in the field, have increased their market share. Nevertheless, along the pathway of PERC cell technology development, the reliability problem has recently grabbed considerable attention from researchers, manufacturers and investors.

It has been found that the rear side of a bifacial glass–glass module is more sensitive to potential induced degradation (PID) than the front side, since the rear side of a PERC cell is not equipped with a full-area rear-side metallization [1,2]. The degradation on the rear side of a bifacial cell module has been shown to be fully or partially recoverable under illumination [1–3]. According to the research conducted by Sporleder et al. [1], the electrochemical formation of $SiO_2$ and the interfacial Na, K and Ca contaminations under cathodic conditions appear to play a major role in the degradation mechanism of the rear side. However, for modules incorporating PERC technology, except for the PID failure of bifacial PERC cells, other failure phenomena – such as continuous degradation in the dark at room temperature of bifacial PERC cell modules, and substantive degradation after damp-heat (DH) and PID tests of monofacial PERC cell modules – have not been explored yet.

**"The rear side of a bifacial glass–glass module is more sensitive to PID than the front side."**

This paper reports not only the results of PID tests on bifacial PERC cell modules fabricated using glass, transparent backsheet and white backsheet as the backboard, but also the results of DH and PID tests on monofacial PERC cell modules. The focus is on the recovery behaviour and how to reduce the degradation. The recovery test is conducted by conditioning the modules in a dry-heat climate chamber at 75°C and injecting a forward $I_{sc}$ current, which mimics the conditions of light and elevated temperature-induced degradation (LeTID) regeneration.

It is found that the power degradation of a bifacial cell module can be restored after the recovery test. The degradation of a monofacial PERC cell module after DH and PID test is also shown to be partially recoverable by injecting a forward $I_{sc}$ current. A bifacial PERC cell module fabricated with a glass–glass layout is more sensitive to PID than one with a glass–transparent backsheet layout. In addition, it is possible for PID failure to occur on a bifacial glass–glass PERC module under either negative or positive bias voltage. The PID degradation of a bifacial PERC cell module with a glass–white backsheet layout can be reduced by using white ethylene-vinyl acetate (EVA) instead of transparent EVA as an encapsulation material on the rear side.

## Experimental

### Monofacial PERC cell module test

Commercial monofacial PERC solar cells from four different manufacturers were used, abbreviated as cell type A, B, C and D. Types A and B were made from boron-doped monocrystalline silicon wafers, while types C and D were made from gallium-doped monocrystalline silicon wafers. All the modules

| Module no. | Cell type | Encapsulation material | Stressed | PID recovery | Forward $I_{sc}$ current injected | DH | High temperature |
|---|---|---|---|---|---|---|---|
| 1 | A | EVA | –1,000V | -- | 1 cycle (48h) | – | – |
| 2 | B | EVA | –1,000V | -- | 1 cycle (48h) | – | – |
| 3 | C | EVA | –1,000V | -- | 1 cycle (48h) | – | – |
| 4 | D | EVA | –1,000V | 96h | 1 cycle (48h) | – | – |
| 5 | D | EVA | – | – | 1 cycle (48h, after DH test) | 1000h | – |
| 6 | D | EVA | – | – | – | – | 200h |

**Table 1. Test items for modules 1–6.**

| Module no. | Cell | Fabrication type | Encapsulation | Stressed material | Dark storage | Forward $I_{sc}$ current injected | Light |
|---|---|---|---|---|---|---|---|
| 7 | E | Glass–glass | POE | –1,500V | 536 days | 4 cycles (each cycle 48h) | – |
| 8 | E | Glass–glass | POE | +1,500V | 536 days | 4 cycles (each cycle 48h) | – |
| 9 | E | Glass–glass | POE | –1,500V | 6 days | – | 530 days |
| 10 | E | Glass–glass | POE | +1,500V | 6 days | – | 530 days |
| 11 | F | Glass–glass | POE | –1,500V | 536 days | 1 cycle | – |
| 12 | F | Glass–glass | POE | +1,500V | 536 days | 1 cycle | – |
| 13 | E | Glass–transparent backsheet | POE | –1,500V | – | – | – |
| 14 | E | Glass–transparent backsheet | POE | –1,500V | – | – | – |
| 15 | E | Glass–glass | POE | –1,500V | – | – | – |
| 16 | E | Glass–glass | POE | –1,500V | – | – | – |

**Table 2. Test items for modules 7–16.**

| Module no. | Cell type | Encapsulation material | Stressed | Forward $I_{sc}$ current injected | EDS |
|---|---|---|---|---|---|
| 17 | E | Front side: transparent EVA<br>Rear side: white EVA | –1,000V | – | Y |
| 18 | E | Front side: transparent EVA<br>Rear side: transparent EVA | –1,000V | – | Y |
| 19 | F | Front side: transparent EVA<br>Rear side: white EVA | –1,000V | 2 cycles (96h) | – |
| 20 | F | Front side: transparent EVA<br>Rear side: transparent EVA | –1,000V | – | – |

**Table 3. Test items for modules 17–20.**

were fabricated with a glass–white backsheet and transparent EVA as the encapsulation material. Table 1 lists all the test specifications for the modules.

In the first part of the experiments, the degradation due to the PID test, as well as the recovery behaviour afterwards, was investigated for modules 1 to 4. The PID test was performed by using a high voltage of –1,000V applied to the frame at a module temperature of 85°C and a relative humidity (RH) of 85%. For the recovery test, stressed modules were injected with a forward $I_{sc}$ current for 48h at 75°C. In the case of cell type D, module 4 was stressed by the PID test and followed by the PID recovery procedure (a high voltage of +1,000V applied to the frame at a module temperature of 85°C and RH of 85% for 96h). The recovery behaviour was subsequently investigated.

In the second part of the experiments, the degradation due to high temperature and high humidity, as well as the recovery behaviour afterwards, was investigated for modules 5 and 6.

### Bifacial glass–glass / glass–transparent backsheet module test

Commercial bifacial PERC solar cells made from boron-doped monocrystalline silicon wafers from two different manufacturers were used, abbreviated as cell types E and F. All the modules were fabricated with a glass–glass or glass–transparent backsheet and polyolefin elastomer (POE) as the encapsulation material. Table 2 lists all the test specifications for the modules.

The degradation due to the PID test, as well as

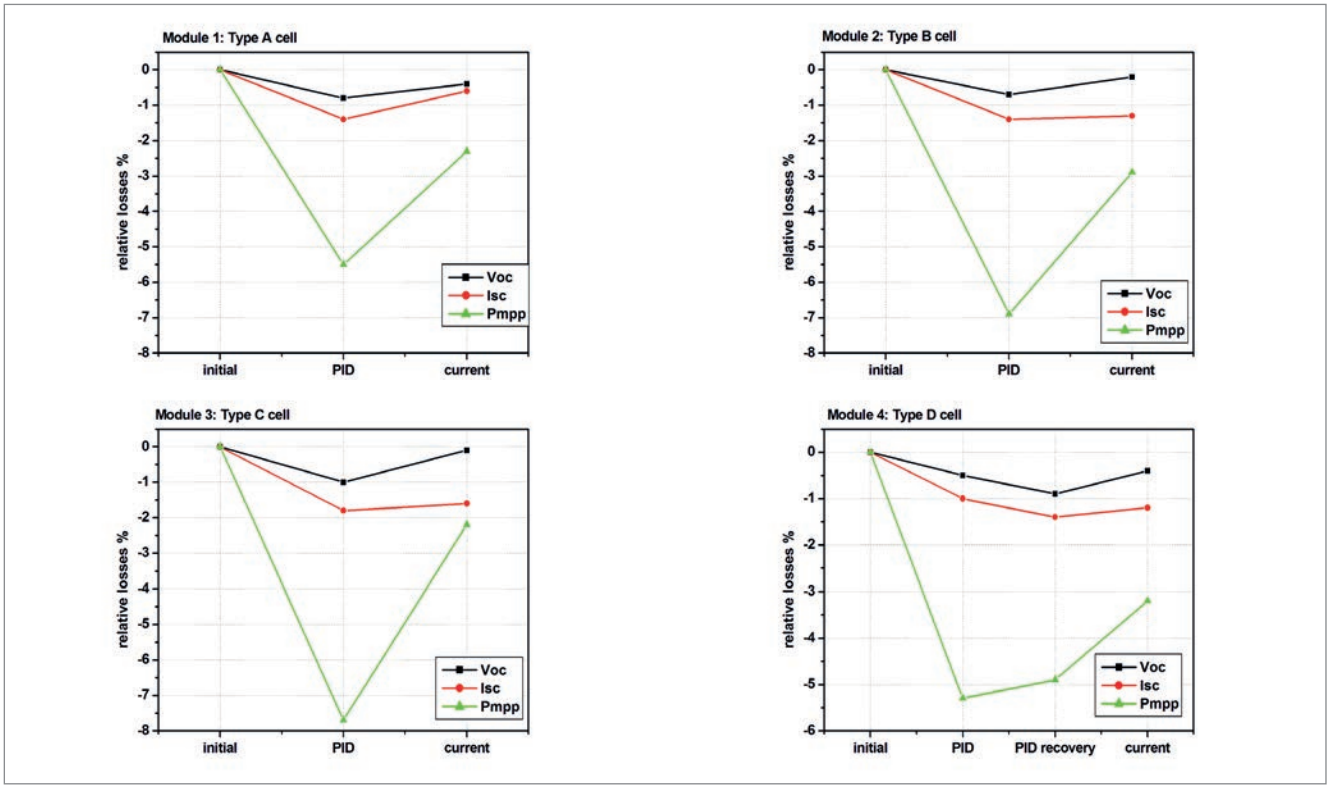


**Figure 1. Relative losses in short-current $I_{sc}$, open-circuit $V_{oc}$ and maximum power output $P_{mpp}$ of the modules under testing.**

the recovery behaviour afterwards, was investigated for modules 7–16. The PID test was performed by using a high voltage of –1,000V applied to the frame at a module temperature of 85°C and RH of 85% for 96h. For the recovery test, two methods were used. In method A, stressed modules were stored in the dark at room temperature for a period of 536 days and subsequently injected with a forward $I_{sc}$ current at 75°C until the power stabilized. In method B, stressed modules were stored in the dark at room temperature for a period of 6 days and then illuminated in the field for 530 days.

### Bifacial glass–white backsheet module test

Glass–white backsheet modules with cell types E and F were fabricated with white EVA or transparent EVA as the encapsulation material on the rear side. Table 3 shows all the specifications for the modules.

In the first part of the experiments, the degradation due to the PID test, as well as the recovery behaviour afterwards, was investigated in modules 17–20. The PID test was performed by using a high voltage of –1,500V applied to the frame at a module temperature of 85°C and RH of 85%. For the recovery test, stressed modules were injected with a forward $I_{sc}$ current for 96h at 75°C.

In the second part of the experiments, energy-dispersive spectroscopy (EDS) (ZEISS X-Max$^N$20 (51-XMX1121)) was employed to investigate the elemental changes of white EVA and transparent EVA before and after the PID test.

**"It is thought that LeTID may play a role during the PID test."**

## Results

### Characterization of monofacial PERC cell module degradation and recovery behaviour after PID and DH tests

#### After PID tests

Fig. 1 shows that all tested modules are prone to PID. The power losses of modules 1, 2, 3 and 4 are –5.5%, –6.9%, –7.7% and –5.3%, respectively, where the corresponding $I_{sc}$ losses of the same testing groups are –1.4%, –1.4%, –1.8% and –1.0%, and the $V_{oc}$ losses are –0.8%, –0.7%, –1.0% and –0.5%. It is clear that the $I_{sc}$ loss is the dominating loss factor here, which is different from the well-known shunting type PID (PID-s) of Al-BSF solar cell module, in which the $V_{oc}$ loss is the dominating loss factor.

Following the PID test, modules 1, 2 and 3 received the recovery test by injecting a forward $I_{sc}$ current. The results show that $P_{mpp}$ and $I_{sc}$ of all the modules recovers partially, whereas $V_{oc}$ shows almost a full recovery. For module 4, the PID recovery test was applied after the PID test, and the subsequent current recovery behaviour was studied. The relative power loss recovers from –5.3% after the PID test to –4.9% after the PID recovery test. In contrast to the power recovery behaviour, $I_{sc}$ and $V_{oc}$ show continuous losses. However, the relative power loss recovers significantly from –4.9% after the PID recovery to –3.2% after the forward $I_{sc}$

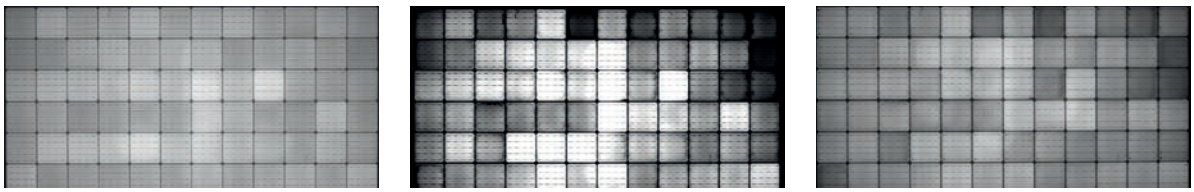

Module 1: cell type A (left: initial; centre: PID test; right: current injection)

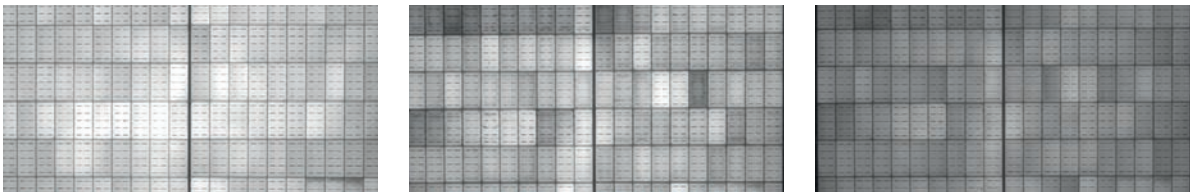

Module 2: cell type B (left: initial; centre: PID test; right: current injection)

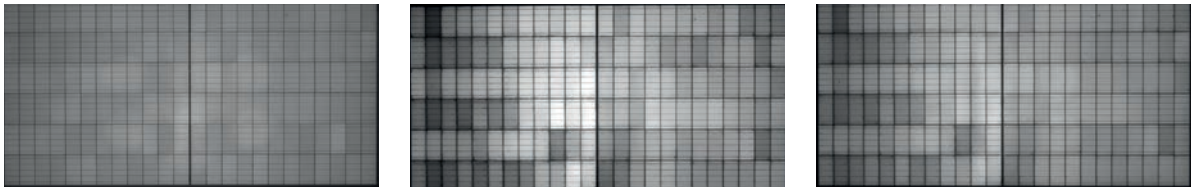

Module 3: cell type C (left: initial; centre: PID test; right: current injection)

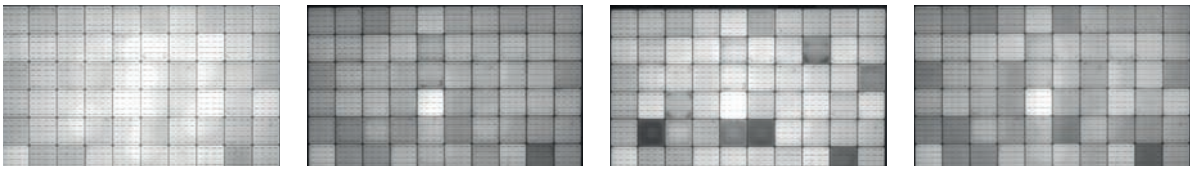

Module 4: cell type D (left: initial; centre left: PID test; centre right: PID recovery; right: current injection)

**Figure 2. EL images of the modules under testing (modules 1–4).**

| Module no. | State | $V_{oc}$ | $I_{sc}$ | $P_{mpp}$ | $V_{oc}$ loss [%] | $I_{sc}$ loss [%] | $P_{mpp}$ loss [%] |
|---|---|---|---|---|---|---|---|
| 5 | DH test | 49.26 | 9.76 | 382.75 | –0.5 | –4.6 | –5.4 |
| | Forward current injected | 49.44 | 9.88 | 390.51 | –0.1 | –3.4 | –3.5 |
| 6 | Initial | 49.03 | 10.08 | 395.19 | | | |
| | High-temperature test | 48.28 | 9.89 | 375.76 | –1.5 | –1.8 | –4.9 |

**Table 4. Electrical characterization of degradation and recovery behaviour.**

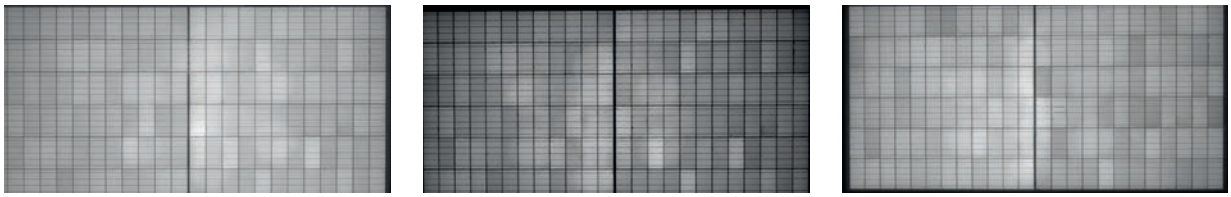

Module 5 (left: initial; centre: DH test; right: current injection)

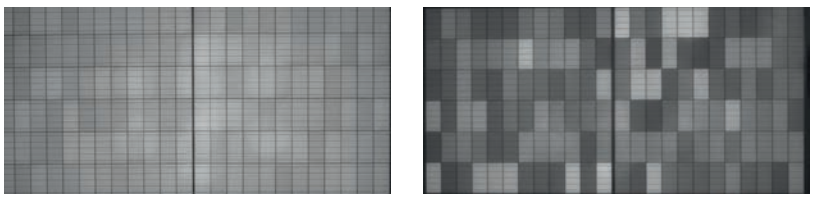

Module 6 (left: initial; right: high-temperature test)

**Figure 3. EL images of the modules under testing (modules 5 and 6).**

# PV MODULETECH CONFERENCE Online 2021

## 9-11 March 2021

Going into its fourth year, **PV ModuleTech** focuses on all aspects of PV modules, including manufacturing, module design, inspection and bankability.

- Understand key metrics behind module quality, reliability & bankability
- Hear from the key stakeholders in GW module supply, certification, testing & factory auditing
- Determine impact of module technology advances on site yield, monitoring & return-on-investments
- Find out which module suppliers are key to unlocking new end-market growth in utility-scale solar

> **Irma Pienaar, Scatec Solar**
> Great networking and technology "deep dive" showing the face of future PV.

> **Nikhil Nahar, SolarSquare Energy**
> The event was focussed, speakers were great, conference was organised very well and topics were relevant.

> **Christophe Inglin, Energetix**
> This event helps me evaluate the substance behind many manufacturers marketing claims.

Sponsors and exhibitors already confirmed:

GOLD SPONSORS

JINERGY · LONGi Solar · Q CELLS Engineered in Germany · RETC · risen solar technology · SERAPHIM

SILVER SPONSOR PVEL

BRONZE SPONSOR Phono Solar

To get involved either as a speaker, partner or attendee please email: **marketing@solarmedia.co.uk**

**moduletech.solarenergyevents.com**

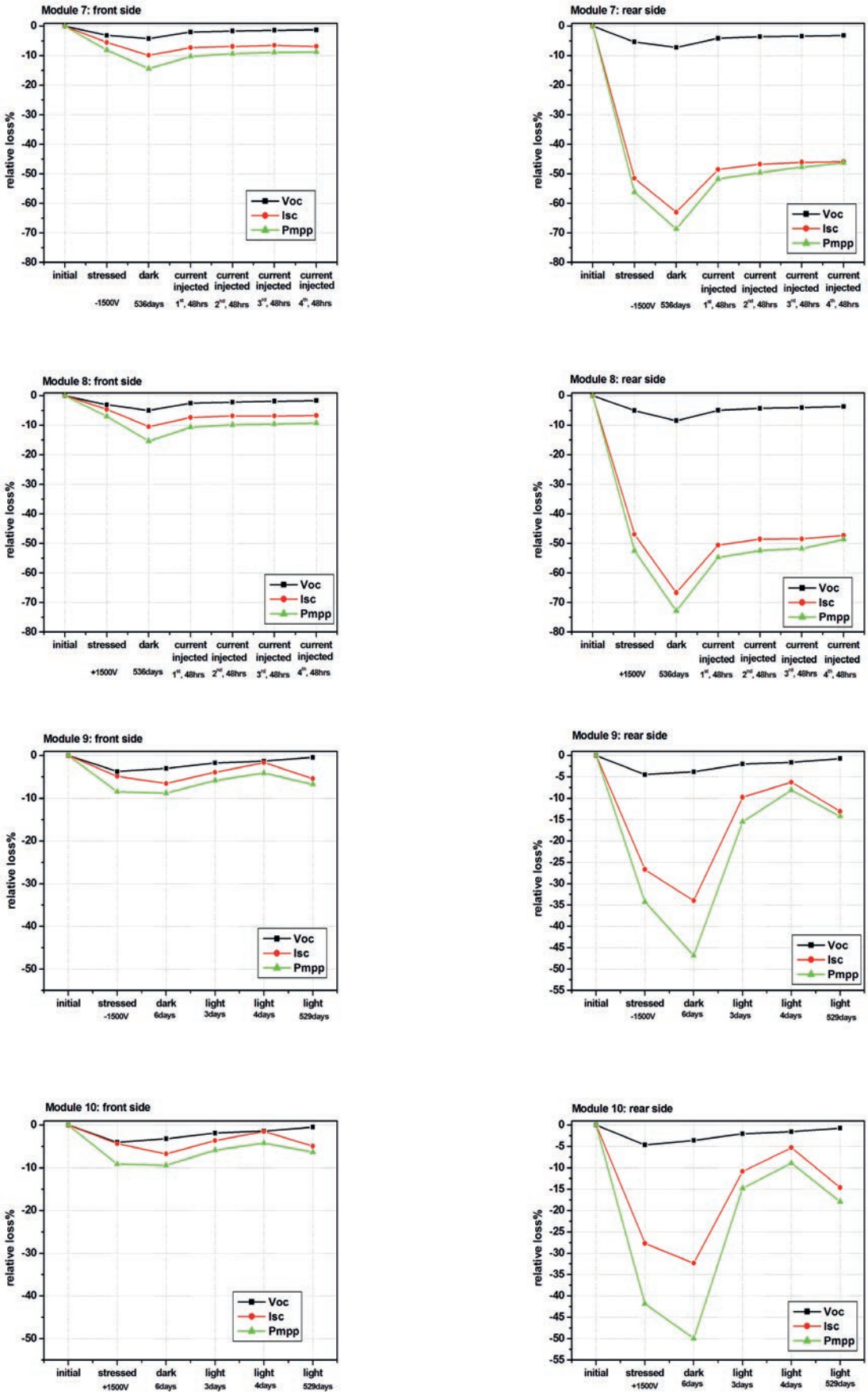


**Figure 4. Relative losses in short-circuit current $I_{sc}$, open-circuit voltage $V_{oc}$ and maximum power output $P_{mpp}$ of the modules using cell type E under testing. For modules 7 and 9, a negative 1,500V voltage was applied during the stress test, while for modules 8 and 10, a positive 1,500V voltage was applied during the test.**

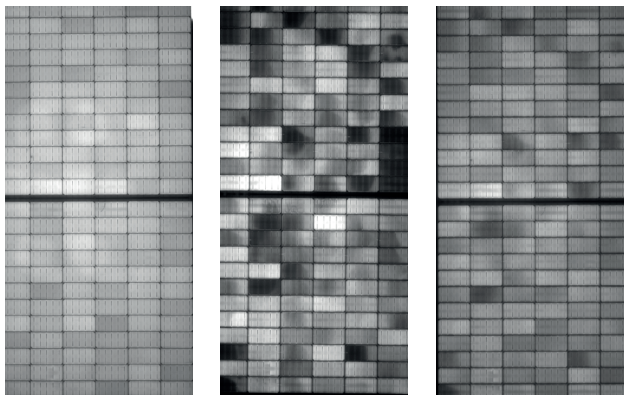

Module 10: front side (left: initial; centre: PID test; right: illumination)

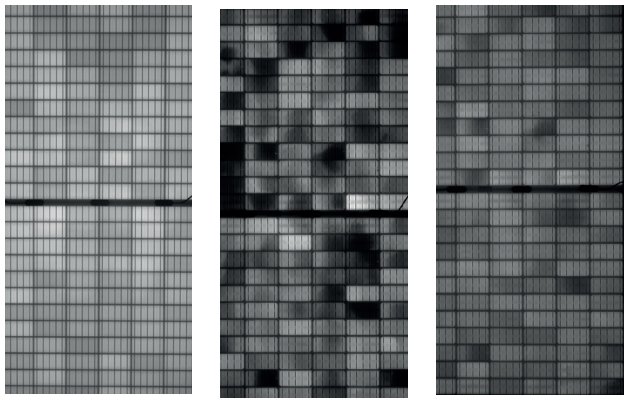

Module 10: rear side (left: initial; centre: PID test; right: illumination)

**Figure 5. EL images of the module under testing (module 10).**

current injection, and $I_{sc}$ also partially recovers, whereas $V_{oc}$ shows almost a full recovery.

Electroluminescence (EL) tests were carried out at each test stage (see Fig. 2). In the stressed state, dark cells can be observed, and the dark cells in modules 1, 2 and 3 can be recovered by injecting a forward $I_{sc}$ current. For module 4, even more dark cells can be observed after PID recovery, although they can also be recovered by injecting a forward $I_{sc}$ current. The changes in the EL images correspond to the changes in electrical characterization. It is therefore thought that LeTID may play a role during the PID test.

### After DH tests

DH (85°C and 85% RH, 1000h) and high-temperature tests (105°C, 200hrs) were conducted on two modules using cell type D and the same encapsulation materials; these underwent the current recovery test afterwards. From the results in Table 4 it can be seen that the tested modules are sensitive to high temperature and that this degradation can be recovered after the current recovery test. The $P_{mpp}$ and $I_{sc}$ of module 5 show partial recovery by injecting forward $I_{sc}$ current, while $V_{oc}$ shows almost a full recovery. An EL test was carried out at each test stage (see Fig. 3). The changes in the EL images correspond to the changes in electrical characterization. It is therefore thought that LeTID may also play a role during high-temperature and high-humidity tests.

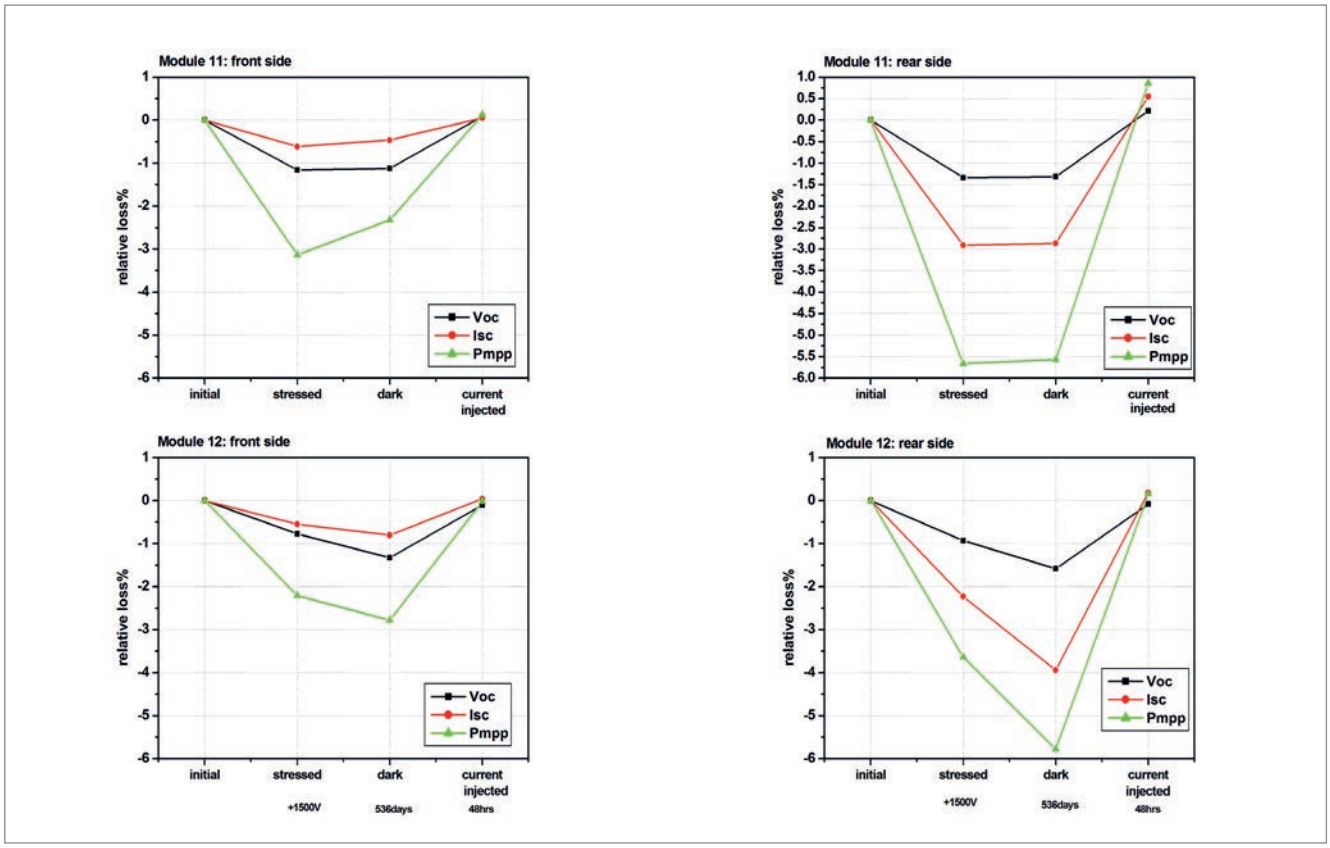


**Figure 6. Relative losses in short-circuit current $I_{sc}$, open-circuit voltage $V_{oc}$ and maximum power output $P_{mpp}$ of the modules using cell type F under testing. For module 11, a negative 1,500V voltage was applied during the stress test, while for module 12, a positive 1,500V voltage was applied during the stress test.**

### Characterization of bifacial glass–glass / glass–transparent backsheet module degradation and recovery behaviour

The rear side of the modules using cell type E (modules 7–10) was found to be more sensitive to PID than the front side; this phenomenon could be observed under either negative or positive voltage (see Fig. 4). The relative $P_{mpp}$ loss is mainly caused by the loss in $I_{sc}$. After the PID test, the modules were stored in the dark at room temperature. Further losses could be observed on the front and rear sides of all tested modules.

Subsequently, modules 7 and 8 exhibited a recovery behaviour after forward $I_{sc}$ current injection, whereas modules 9 and 10 showed illumination recovery behaviour (illumination of the rear side). The $P_{mpp}$ and $I_{sc}$ of these modules only recover partially, whereas $V_{oc}$ shows almost a full recovery after applying the two different recovery methods. Furthermore, the recovery behaviour by illumination on the rear side is more pronounced than that achieved by forward $I_{sc}$ current injection.

Fig. 5 shows the EL images of module 10 for each test stage. The changes in the EL images correspond to the changes in electrical characterization.

In contrast, for the modules using cell type F, a full recovery can be observed after forward $I_{sc}$ current injection (see Fig. 6).

The same difference in PID sensitivity mentioned earlier was observed for the bifacial modules from different manufacturers: the rear side was more sensitive to PID than the front side. However, it was found that the loss on the rear side can be reduced when using a transparent backsheet instead of glass, probably because of the fact that the backsheet has a higher insulation resistance than that of glass (see Figs. 7 and 8).

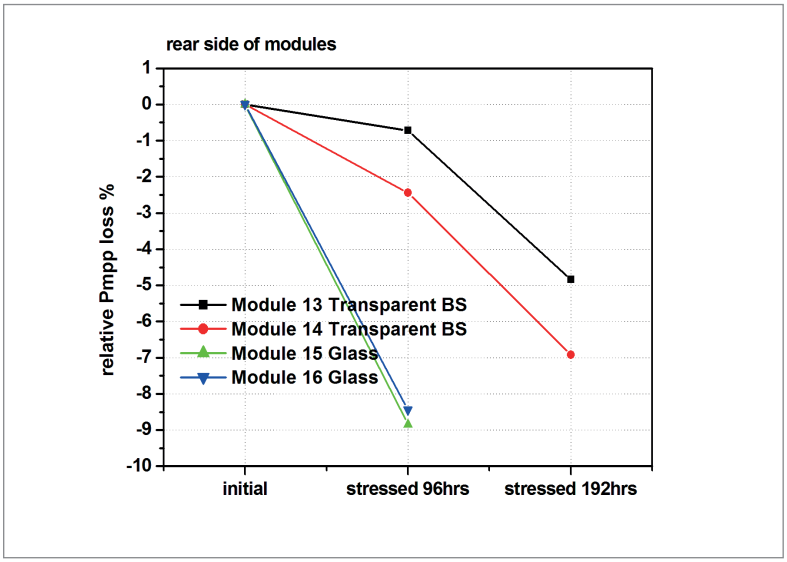


**Figure 7. Relative losses in maximum power output $P_{mpp}$ for modules using a transparent backsheet and glass as the backboard.**

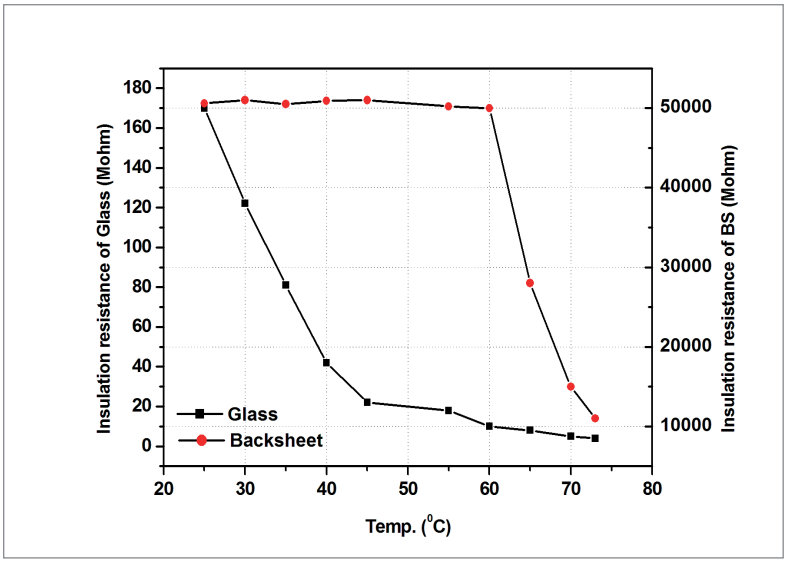


**Figure 8. Insulation resistance of glass and backsheet at different temperatures.**

### Characterization of bifacial glass–white backsheet module degradation and recovery behaviour

A bifacial PERC cell module with a glass–white backsheet layout can achieve higher power gains than a monofacial PERC cell module, and is therefore normally considered to be an alternative choice for a high-power module. Nevertheless, the PID phenomenon on the rear side still influences the power output of the module, although the power on the rear cannot be measured because of the use of a white backsheet. However, it was found that the degradation on the rear side of a bifacial PERC module can be reduced when using white EVA instead of transparent EVA as the rear-side encapsulation material (see Fig. 9). The difference between white EVA and transparent EVA is the inclusion of titanium dioxide ($TiO_2$), which can enhance the reflection of light on white EVA and therefore increase the power output.

The recovery test by the injection of a forward $I_{sc}$ current after the PID test was conducted on module 20 and followed by a PID recovery test. It was found that the module recovered partially after injecting forward $I_{sc}$ current: the relative $P_{mpp}$ loss decreased from –7.57% after the PID test to –1.66% after forward $I_{sc}$ current injection (Fig. 10). On the other hand, the module showed further power loss after the PID recovery test: the relative $P_{mpp}$ loss increased from –1.66% after forward $I_{sc}$ current injection to –2.83% after the PID recovery test.

EDS was carried out on modules 17 and 18 to analyse the difference between white EVA and transparent EVA after a 288h stress test. The result shows that Na, K and Cl can be found in white EVA after the PID test, compared with the initial state (see Fig. 11). No change in transparent EVA can be observed before and after the PID test. It is believed that the $TiO_2$ in white EVA can influence the movement of Na and K coming from the cell.

**"The loss on the rear side can be reduced when using a transparent backsheet instead of glass."**

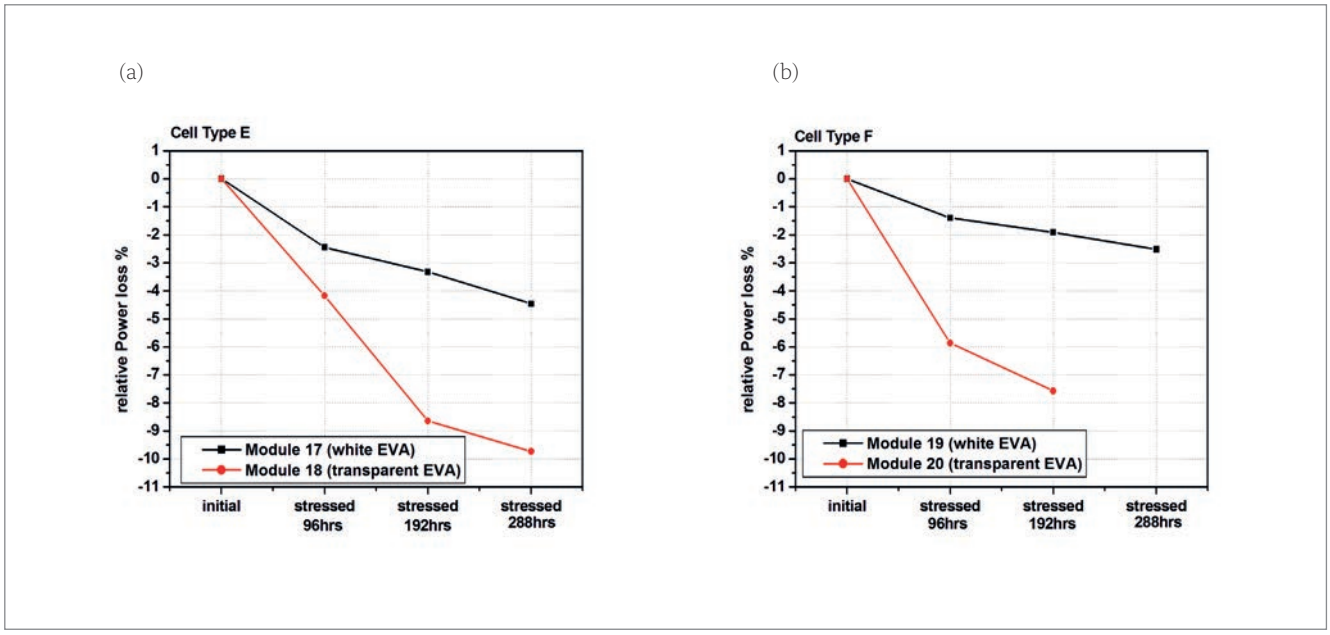


**Figure 9. Relative losses in maximum power output $P_{mpp}$ of a module using transparent EVA and white EVA as the encapsulation material: (a) module with cell type E; (b) module with cell type F.**

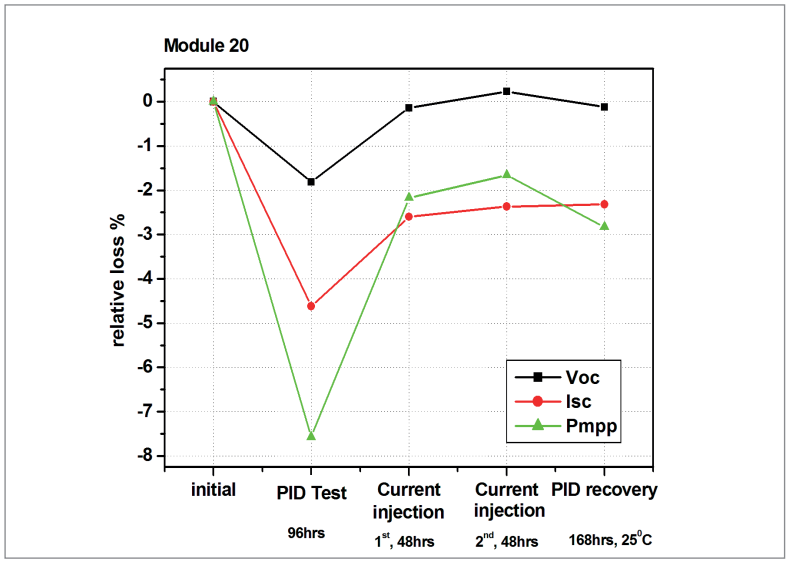


**Figure 10. Relative losses in maximum power output $P_{mpp}$ of module 20 after the forward $I_{sc}$ current injection recovery test and the PID recovery test.**

**"The degradation on the rear side of a bifacial PERC module can be reduced when using white EVA instead of transparent EVA as the rear-side encapsulation material."**

## Conclusions

Modules using monofacial PERC cells from four different manufacturers (cell types A, B, C and D) were found to be prone to PID. For modules using cell type D, high power loss was also observed after DH and high-temperature tests. The relative $P_{mpp}$ loss in all tested modules recovered partially by injecting forward $I_{sc}$ current at 75°C.

For bifacial glass–glass modules, PID failure can occur under either negative or positive voltage. The modules using cell type E or cell type F were found to be prone to PID on the rear side, which is in good agreement with the findings in the literature [1–3]. The relative $P_{mpp}$ loss can be recovered by injecting forward $I_{sc}$ current at 75°C or by subjecting to illumination. Different recovery behaviours were observed in cells from different manufacturers: the relative $P_{mpp}$ loss in modules using cell type E partially recovered, whereas modules using cell type F fully recovered.

In the case of bifacial PERC cell modules fabricated with a glass–white backsheet, the PID failure on the rear side can be reduced when using white EVA instead of transparent EVA as the encapsulation material. An EDS analysis showed that Na and K can be found in white EVA after the PID test, compared with the initial state.

The failure of PERC cells under PID and DH tests can be recovered by applying the LeTID regeneration method, where forward $I_{sc}$ current is injected at 75°C. It is therefore believed that LeTID may play a key role during PID and high-temperature tests.

## References

[1] Sporleder, K. et al. 2019, "Root cause analysis on corrosive potential-induce degradation effects at the rear side of bifacial silicon PERC solar cells", *Sol. Energy Mater. Sol. Cells,* Vol. 201, p. 110062.

[2] Luo, W. et al. 2018, "Elucidating potential-induced degradation in bifacial PERC silicon photovoltaic modules", *Prog. Photovolt: Res. Appl.*, Vol. 26, No. 10, pp. 859–867.

[3] Luo, W. et al. 2018, "Investigation of the impact of illumination on the polarization-type potential-induced degradation of crystalline silicon photovoltaic modules", *IEEE J. Photovolt.*, Vol. 8, No. 5, pp. 1168–1173.

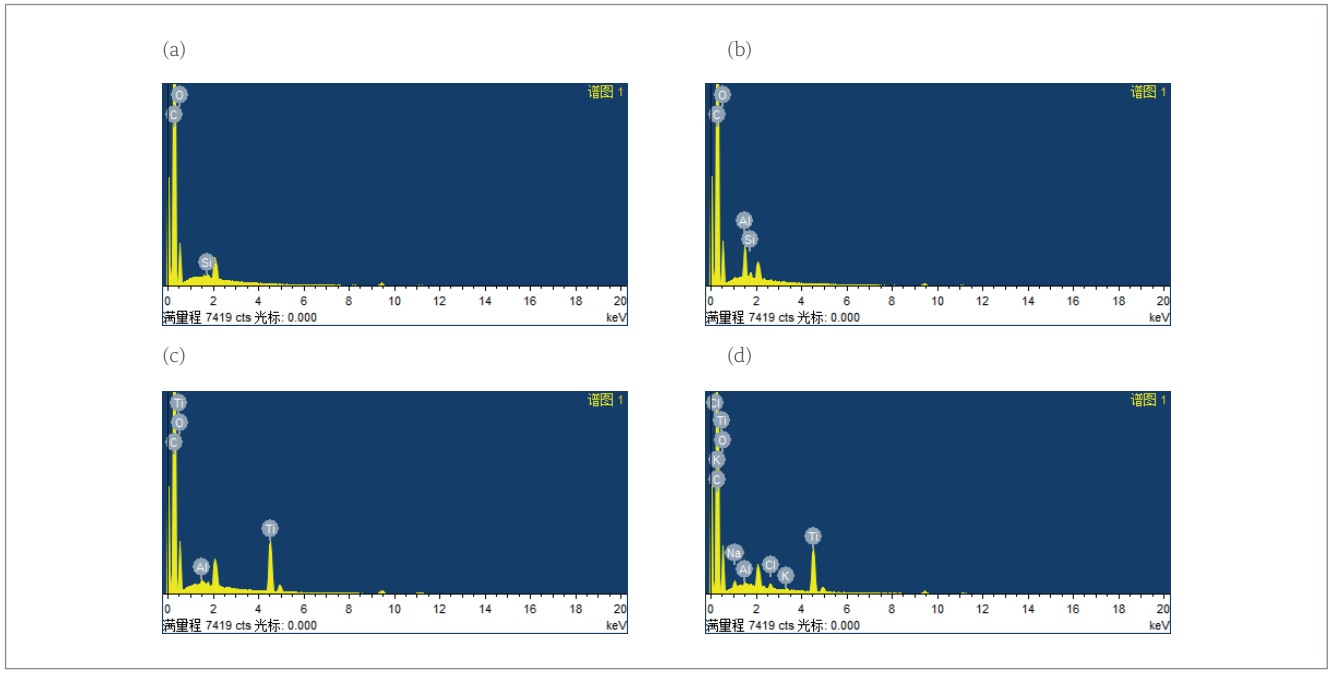


**Figure 11. EDS characterization of white EVA and transparent EVA: (a) transparent EVA in the initial state; (b) transparent EVA after the PID test; (c) white EVA in the initial state; (d) white EVA after the PID test.**

## About the Authors

Haidan Gong is the director of Suntech's PV test centre. She studied polymer materials at the Changzhou University of Jiangsu and received her master's in 2008. She has been with Suntech since 2008, where her current research interests include failure analysis of modules and materials.

Minge Gao is a material testing engineer at Suntech's PV test centre. She graduated in 2007 from Yangzhou University, majoring in polymer materials. She has been with Suntech since 2008.

Yiwei Guo is a material testing engineer at Suntech's PV test centre, focusing on testing and evaluation of PV material. He has been with Suntech since 2008.

Jian Wang is a module testing engineer at Suntech's PV test centre, focusing on testing and evaluation of PV modules. He graduated from Jiangnan University in 2005, majoring in biotechnology. He has been with Suntech since 2012.

Xiaogang Zhu is head of the PV material research and test department at CPVT. He focuses on quality appraisal and testing of PV product technical development. He has been with CPVT since 2009.

Jiayan Lu is the technical director of CPVT. She studied optical engineering and received her master's from Jiangnan University. She works on quality analysis and development of standards for PV products.

Shan Yanyan is a senior engineer at CPVT. Her current research interests include PV raw material technology development and testing certification, failure analysis and identification. She has been with CPVT since 2009.

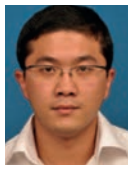

Yi Liu is the director of CPVT, focusing on the development of new detection methods. He has been with CPVT since 2012.

**Enquiries**
Haidan Gong
16 Xinhua Road
New District, Wuxi
China 214028

Tel: +86 15105192716
Email: haidan.gong@suntech-power.com
Website: http://www.suntech-power.com

# Both sides now: Optimal bifaciality with silicon heterojunction solar cells

Adrien Danel, Julien Eymard, Vincent Barth, Mathieu Tomassini, Eric Gerritsen, Armand Bettinelli & Charles Roux, CEA, LITEN, Department of Solar Technologies, INES, Grenoble, France

## Abstract

Silicon heterojunction (SHJ) solar cells are by nature bifacial, and their back-to-front ratio (bifaciality) can be easily tuned by means of the pattern of the metal grid on the front and back sides. This paper discusses, at both the cell and the module level, the balance between the advantages and drawbacks of increasing the cell bifaciality from a typical value of 90% towards 100%, or decreasing it towards that of monofacial cells (0%). For outdoor operation with extra light hitting the back side, the effective performance of bifacial systems was estimated with regard to the trade-off between cell efficiency and bifaciality. This work presents how very high bifaciality comes at a cost of lower (front-side) conversion efficiency, and discusses how the amount of silver paste per cell, a main contributor of cell cost, is strongly related to cell bifaciality and efficiency. The use of a symmetric grid pattern is one easy way of obtaining highly bifacial cells, but at the expense of high resistivity in the case of metal grids using a typical front-side pattern. On the other hand, a rear-side pattern used on the front and back sides can lead to a situation where there is excessive shading. Furthermore, the efficiency of a rear-emitter cell decreases at very high bifaciality with the use of thinner amorphous layers on the back side, necessary for symmetrizing the light absorbance of the cell. Thus, an optimum can be found for a given system design operating with a given irradiance at the back side. Similarly, for a given type of cell, systems can be specifically designed to optimize the benefits of the given cell bifaciality. The output of tilted modules is maximum when a large proportion of light comes from the back side, with cell bifaciality ranging from 85% to 95%. The use of an optimal metal grid can offer a relative gain in energy production, as high as 3%, and typically corresponds to a front-side metal grid pitch from 1.2 to 2mm and a back-side pitch from 0.6 to 0.9mm. When specific applications are considered where a symmetrical print is preferred for building-integrated or vertically oriented systems, the optimal grid pitch is around 1.5mm. For monofacial systems, the use of bifacial cells is beneficial, thanks to the internal reflection in glass-backsheet modules and because of the cost saving for additional rear-metallization.

*Reproduced, with permission, from Willocket et al. [8].*

**Figure 1. Pilot agri-PV in an orchard at Bierbeek, Belgium, illustrating the benefit of bifacial cells for high-transparency modules placed at a high elevation.**

## Bifacial is blooming

True bifacial PV systems are today entering real deployment with a 14-fold increase expected over the next five years, as forecast by ITRPV [1]. It is no longer a niche technology reserved for cells with the highest efficiencies, but a 'giant leap for kWh cost reduction' [2] applied to the main current and future cell technologies: PERC (passivated emitter rear cell), PERT (passivated emitter rear totally diffused), TOPCon (tunnel oxide passivated contact), SHJ (silicon heterojunction) and even IBC (interdigitated back contact). Accordingly, an estimation of the bifacial benefit of individual installations has recently been intensively studied [3], with simulations [4] and experimental field data [5], including the LCOE (levelized cost of electricity) [6,7]. These studies, based on a given type of cell and module, are very useful to PV installation companies for selecting the most relevant technologies and for optimizing their designs when considering operational conditions for particular projects, as illustrated in Fig. 1 [8]. However, ahead of this, the possibility of adapting the bifaciality of cells has so far been poorly taken into consideration.

With their symmetrical structure, SHJ solar cells made of very thin hydrogenated amorphous silicon layers (a-Si:H), transparent conductive oxides (TCO), and metallization grids deposited on both sides of the wafers are by nature bifacial [9]. This paper is a continuation of a study [10] in which the bifaciality of busbar and busbar-less SHJ cells ($BF_{cell}$) was varied using different metallization grid patterns; the subsequent impact on cell efficiency was investigated in order to estimate the system output versus the amount of light at the back side. Here, the way the differences in thin films deposited on the front and rear sides affect the bifaciality will also be presented, and the possibilities of approaching a cell bifaciality of 100% will be discussed.

## Experimental details and methodology

The cell manufacturing was performed on the CEA SHJ pilot line [11] located at INES, the French National Solar Energy Institute, using a rear-emitter double-side-contacted (screen printing with low-temperature Ag paste) configuration on full-size commercial n-type Cz wafers (M2 size, 244.3cm², from Longi). The bifaciality factor of each *I–V* parameter is the back-to-front ratio measured under standard test conditions (STC). $BF_{cell}$ is the lowest value coefficient, usually the power one.

The cell bifaciality was first varied using different finger pitches on busbar-less (BB-less) and busbar (BB) grid patterns. The configurations in this study range from a very dense grid on the back side for low bifaciality, to identical-spaced grids on the front side (FS) and the back side (BS) in order to achieve high bifaciality and symmetrical-looking cells. In practice, the finger pitch varied from 0.2 to 2.1mm. All *I–V* measurements were performed over the total area under AM1.5G STC using an *I–V* tester without back-side reflection, calibrated against sister cells certified by the FhG ISE CalLab and ISFH CalTeC. Each bifaciality experiment with a given design (BB-less or BB) was carried out on cells from the same production run using the CEA-INES baseline process flow. Sets of cells were randomly selected for each screen-printing batch, and labelled according to the FS and BS grid pitch (mm), as illustrated in Fig. 2 with an example of data for a BB design.

Next, similarly to the IEC 60904-1-2 standardization work [3,5], BB-less and BB cell efficiency as a function of $BF_{cell}$ (see Fig. 3) data were used to calculate a figure of merit for bifacial systems. Equation 1 represents tilted modules, where *BIFI* is the back-side irradiance relative to the front-side irradiance, in per cent. As an example, $BIFI_{20}$ corresponds to an equivalent of 200W/m² on the back side when the front side is illuminated by 1000W/m². Equation 2 represents vertical east–west-oriented modules (V-EW), for which direct sunlight shines for half the time on the front side and for

**"With their symmetrical structure, SHJ solar cells made of very thin a-Si:H layers, TCO and metallization grids deposited on both sides of the wafers are by nature bifacial."**

half the time on the back side, with the same irradiance on the rear of the panel, i.e. the same BIFI factor. In other words, first (i.e. in the morning) the back side is the 'true' rear side of the module, then (in the afternoon) the back side becomes the side of the module receiving mostly direct light. Possible differences between the average *BIFI* during the morning and the afternoon are not considered here.

$$\eta_{system} = \eta_{cell} \times CTM \times (1 + BF_{module} \times BIFI) \quad (1)$$

$$\eta_{system} = \eta_{cell} \times CTM \times [0.5(1 + BF_{module} \times BIFI) + 0.5\,(BF_{module} + BIFI)] \quad (2)$$

where,

$\eta_{system}$ is the system output (figure of merit),
$\eta_{cell}$ is the front-side STC power conversion efficiency,
*CTM* is the cell-to-module loss ratio,
$BF_{module}$ is the module bifaciality factor estimated from practical $BF_{cell}$,
*BIFI* is the average of the overall light input at the back side, levelled over one year. (Note that, strictly speaking, the back side of a V-EW system alternates for half the day between the true back side and the front side of the system.)

In this work, the intention is not to define bifaciality factors for particular cases. From the literature [3–6] and CEA's own field data for SHJ systems [7,12], the range of practical *BIFI* one can deal with worldwide is simply extracted: the $\eta_{system}$ as a function of $BF_{cell}$ for values of *BIFI* ranging from 0 to 40% was therefore studied in order to determine the optimal SHJ cell bifaciality factor for a given module technology operating at a specific bifaciality factor. This simple approach was taken, whatever the actual parameters determining the bifaciality factor, such as system design (module tilt and elevation above ground, number of modules and rows, spacing, etc.), system orientation, geographical location, typical meteorological year, ground albedo, surroundings, and so on, and whatever the temporary *BIFI* variations for different weather conditions [13].

The $BF_{module}$ coefficients are the experimental $BF_{cell}$ data corrected for the effective grid shading: 95% in air and around 72% in a module [14]; this important factor was verified in practice, as reported in Danel et al. [10]. Indeed, the effective bifaciality of cells in a module is always higher than that of bare cells in air, with the difference increasing as $BF_{cell}$ decreases.

Despite this approach possibly not strictly representing all applications (for example, new systems with very low cell coverage specifically designed for agriculture, where bifaciality is must, as illustrated in Fig. 1 [8]), the trend of $\eta_{system}$ as a function of $BF_{cell}$ allows the determination of an optimal cell design for a given system project.

In addition to the practical data, a two-diode model was developed in-house and used to simulate efficiency and power response at the cell and module levels for various bifaciality and *BIFI* conditions. Key electrical and optical parameters are assumed to fully represent module and cell design, including the material properties and heterojunction specificities. The series resistance ($R_s$) of the metallization is modelled from the resistivity of: 1) low-temperature silver paste; 2) electrically conductive adhesive; and 3) ribbons. This modelling takes into consideration the effective shape of each of the three resistivity elements.

The bulk resistance of the crystalline silicon substrate and the TCO layers is taken into account, so that changes in lateral transport of charges can be considered when the pattern of the metal grids varies [8]. This simulation also includes the losses

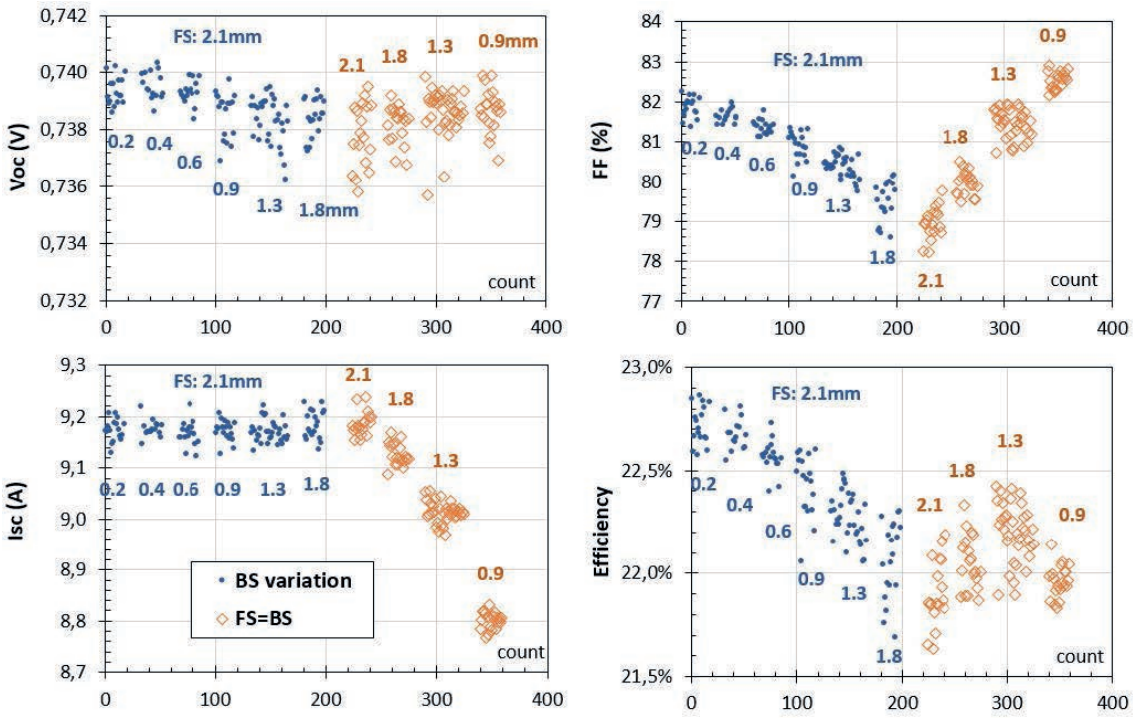


Adapted from Danel et al. [10].

**Figure 2. Bifaciality experiments on BB cells, where the back- and front-side metal grid pitch (noted in mm) was varied while keeping the same screen parameters (mesh, emulsion, opening, etc.). The cell-to-cell main *I*–*V* parameters are plotted using blue dots for asymmetric prints and orange diamonds for symmetric prints.**

in performance of cells after being cut in order to allow for modules with half-cells or third-cells. The effective shapes of the grids (number and shape of fingers and busbars), and the reflectivity, absorbance and transmittance of materials (cells, glasses, encapsulants, metal grids and ribbons), are measured and considered for assessing the optical behaviour of the modules [15,16].

## Cell efficiency versus bifaciality

The bifaciality factors of each *I–V* parameter were measured for the cells in Fig. 1, as well as for two other similar experiments in which the pitch of fingers in the BS grid were varied while keeping the same FS grid. The quantity $BF_{cell}$ is the power bifaciality, mainly driven by the short-circuit current ($I_{sc}$) bifaciality.

The average cell efficiency of each batch is plotted against $BF_{cell}$ in Fig. 3. The SHJ cell efficiency shows a steady decay from a monofacial to a highly bifacial design, with a significant drop in the highest cell bifaciality values being obtained when identical-spaced grids FS and BS are used (2.1mm and 2.1mm in this study for the splits of cells having an indium tin oxide (ITO) at the back side). For the BB-less and ITO BS experiment, a couple of reference cells (pitch 2.1mm FS and 0.6mm BS) received an additional plain metallization rear side by silver physical vapour deposition (PVD) to produce monofacial cells. In Fig. 3 and Table 1, this is the batch of cells with a bifaciality of 3.4% and a +0.16%$_{abs}$ efficiency compared with the reference batch.

The efficiency decay is similar for the BB and BB-less cell designs and is mainly related to the decrease in fill factor (*FF*) and increase in $R_s$, due primarily to the resistive contribution of the BS grid (as can be seen in Fig. 1). The test with $In_2O_3$-based TCO by PVD [17,18] at the back side illustrates how the lateral conduction of the TCO can also be an important limitation when increasing the pitch. Indeed, the very good material properties for charge collection on the p contact with a high transparency are counteracted by the limited lateral conduction. For this test, the good electrical properties of this material were intentionally degraded to boost the optical properties. Thus, if $In_2O_3$-based TCO can perform well with a dense grid BS, as well as offering significant improvement in FS cell efficiency, its integration in very high bifaciality cells is more delicate than when ITO is used.

It is worth noting that a bifaciality factor <100% is obtained for a symmetrical print as a result of the rear-emitter cell optimization for a maximum front-side efficiency at STC. This is achieved with different hydrogenated amorphous silicon stacks (a-Si:H) and TCO thicknesses and electro-optical properties on the FS and BS in order to ensure a high minority-carrier lateral conduction [19] in a good balance with transparency.

Conversely, a monofacial design offers a bonus

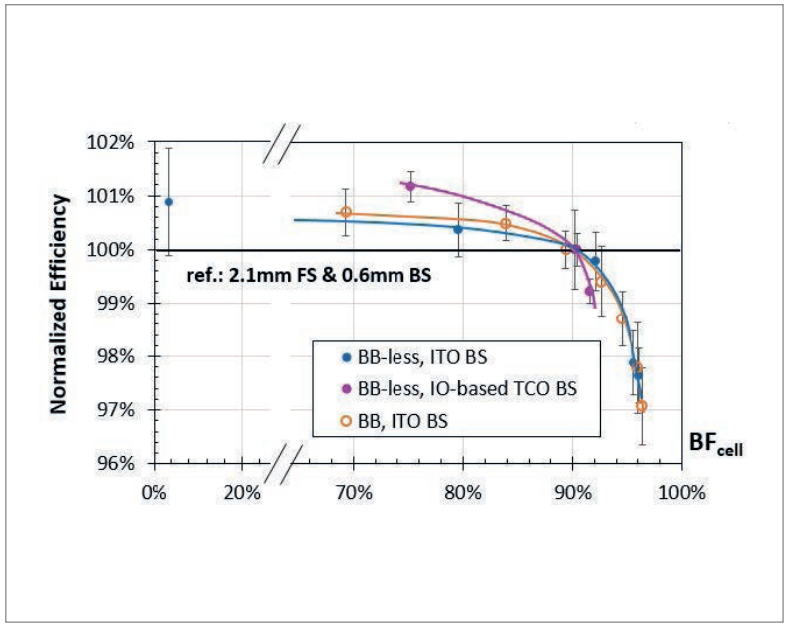


**Figure 3. BB and BB-less normalized cell efficiency as a function of cell bifaciality. The dots/circles represent the average, and the error bars the standard deviation of each cell batch. The reference is the 2.1mm FS and 0.6mm BS print. Two different TCOs are considered here. The solid lines have been added as a visual guide.**

for the FS *I–V* data of SHJ cells, but the +0.16%$_{abs}$ seen in practice requires an extra process step with associated costs. Furthermore, the use of monofacial cells for monofacial applications is not useful. In previous work carried out by CEA [10], a similar power output was obtained for glass-backsheet modules with white encapsulant and bifacial cells thanks to a better CTM coefficient using the reference print (90% $BF_{cell}$) compared with true monofacial cells. This result occurred by virtue of an 'embedded' bifaciality, with a good reflection onto the encapsulant and backsheet of both the incident light entering the module in between the cells and the near-infrared light passing through the cells.

Table 1 summarizes typical *I–V* values for CEA's SHJ cells with ITO on both sides and with processes optimized with the reference print. This illustrates the latitude one may have in optimizing cells for a given system application, taking into account efficiency, bifaciality and costs (amount of silver paste).

## Towards 100% bifaciality: virtues and vices

With symmetric ITO and prints on the FS and BS, a $BF_{cell}$ of around 95% is obtained. This 'intrinsic' cell bifaciality, the highest value in Fig. 3, is related to the asymmetry between the a-Si:H layers, with a thicker and less transparent intrinsic (i) and p-doped stack at the BS, and an i and n-doped stack at the FS. As studied in Danel et al. [10] and shown in Fig. 4, $BF_{cell}$ can be pushed above 98% using a very thin i and p a-Si:H stack. Layers that are too thin, however, can cause *FF* or $V_{oc}$ degradation, as plotted in Fig. 4(a). Starting from the plasma-enhanced chemical vapour deposition (PECVD) recipes normalized to 1 in Fig. 4 (blue arrows), an analysis was performed to find a good

| Metal | $\eta$ [%] | $V_{oc}$ [mV] | $J_{sc}$ [mA/cm$^2$] | *FF* [%] | Bifaciality [%] | Ag paste [mg] |
|---|---|---|---|---|---|---|
| Reference: 2.1/0.6mm | 22.70 | 737.4 | 38.33 | 80.26 | 90.2 | 117 |
| Monofacial | 22.86 | 738.2 | 38.47 | 80.46 | 3.4 | 117 + PVD Ag |
| 2.1/0.3mm | 22.74 | 737.6 | 38.31 | 80.46 | 79.6 | 212 |
| 2.1/0.9mm | 22.57 | 738.2 | 38.32 | 79.78 | 92.1 | 86 |
| Symmetric: 2.1/2.1mm | 22.13 | 737.7 | 38.30 | 78.32 | 96.1 | 44 |
| Optimized: 1.5/1.5mm | 22.40 | 737.2 | 38.39 | 79.10 | 96.1 | 56 |

**Table 1. Main *I–V* parameters of SHJ cells having various metallization patterns.**

"A bifaciality factor <100% is obtained for a symmetrical print as a result of the rear-emitter cell optimization for a maximum front-side efficiency at STC."

balance between the i and p layer thicknesses and tune the electrical properties. A 17%-thinner back-side stack was developed and ensures a 95–96% intrinsic bifaciality, without affecting FS cell efficiency (0.83 normalized point and the grey arrow in Fig. 4).

If $BF_{cell}$ >98% can be easily achieved by experimenting with a BS pitch larger than the FS pitch, or by using a thicker a-Si:H stack at the FS, this will be to the detriment of cell efficiency. Therefore, for very high bifaciality cells dedicated to applications, such as planar connections [16,20,21] or V-EW systems, where similar electrical performance is preferred in order to avoid electrical mismatch, the case of a symmetric print was considered and the pitch of the fingers varied.

As shown in the plots in Fig. 5, the use of a dense grid (typically a BS design) leads to an $I_{sc}$-limited cell efficiency, while the use of a large pitch (FS design) results in an *FF*-limited situation, mainly related to grid $R_s$ and lateral conduction in the TCO limitation on the rear side. Specific to CEA's printing process, an optimal pitch of about 1.5mm balances the $I_{sc}$ and *FF* limitation scenarios. It is worth noting

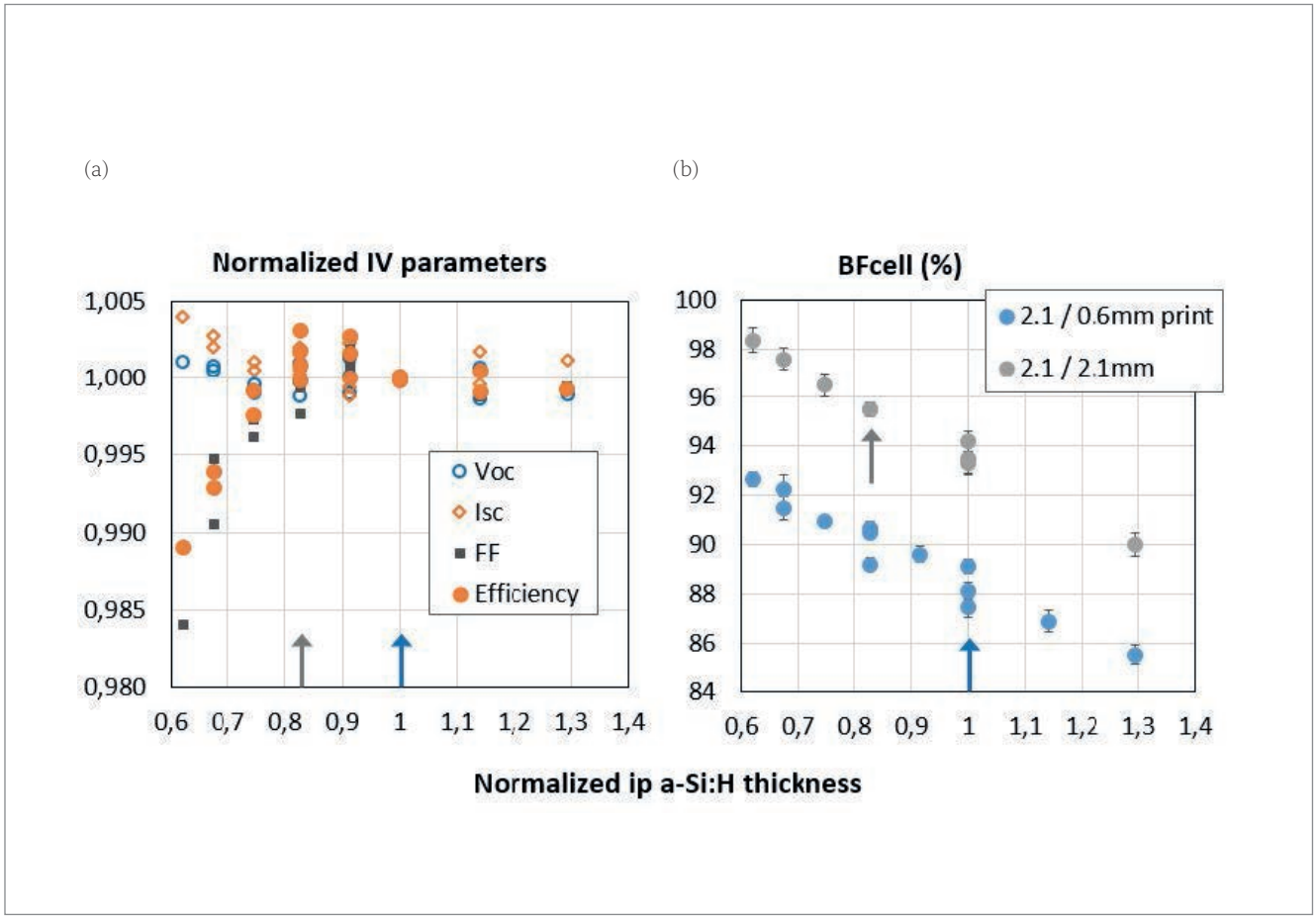


**Figure 4. i and p a-Si:H stack optimization to enhance cell bifaciality: (a) *I–V* data normalized to 1 for CEA's pilot line reference recipes; (b) corresponding cell bifacialities. Each point is the average of a multiple cell batch, and the error bars on graph (b) represent standard deviations.**

that all points in Fig. 5 have a bifaciality of about 95%, driven by the a-Si:H stacks asymmetry, as mentioned in the discussion of Fig. 4.

### Estimation of system output

The experimental cell data in Fig. 3 are used in the proposed figure of merit (Equations 1 and 2) to estimate the system energy output as a function of cell bifaciality, with the following assumptions:

1. A constant *CTM* of 0.98 (2% loss) for glass–glass industrial SHJ modules [22], independent of the value of $BF_{cell}$ (a hypothesis validated by experimental data from two mini-modules).

2. A bifaciality factor ranging from 0 to 40% in order to cover any practical system design and operating conditions.

3. A constant cell efficiency (STC value), whatever the value of the bifaciality factor. This simple hypothesis disregards possible average efficiency changes with different module temperatures in the morning and the afternoon, or with variations in *BIFI*. It might also not be valid for a precise estimation of system equivalent efficiency, since when the *BIFI* increases, the current increases by a factor $(1 + BIFI \times BF_{module})$, and accordingly the resistive losses might become important. However, thanks to the module simulation taking this into account, and with the aim of determining the optimal $BF_{cell}$ for a given bifaciality factor, the assumption can be considered to be valid.

Fig. 6 shows the estimation of system output, i.e. the equivalent efficiency of (a) tilted and (b) V-EW systems for various *BIFI*, for cells with ITO FS and BS and an 'intrinsic' bifaciality of about 96%. The arrows on the charts highlight the estimation of the optimal cell bifaciality for a given bifaciality factor. For the tilted module situation (Fig. 6(a)), the higher the *BIFI*, the higher the cell bifaciality. This is accompanied by a fairly strong dynamic for low *BIFI*: the optimal $BF_{cell}$ moves quickly from about 80% for $BIFI_5$ to 91% for $BIFI_{20}$. Then, interestingly, from a practical point of view, at higher *BIFI* the optimal $BF_{cell}$ increases more slowly and tends to saturate at about 92%. This typically corresponds to prints with a FS pitch of 2.1mm and a BS pitch between 0.6 and 0.9mm.

Compared with the tilted system in Fig. 6(a), the optimal $BF_{cell}$ for V-EW systems (Fig. 6(b)), is higher, at 93%, and almost constant, regardless of the value of *BIFI*. A symmetrical print offering

the highest cell bifaciality and nice aesthetics for vertical modules is not the best option for system output in this example with a 2.1mm pitch. However, as reported in Danel et al. [10] and illustrated in Fig. 5, with an intermediate pitch of around 1.5mm to optimize the FS cell efficiency, a very good equivalent efficiency for V-EW modules can be obtained with a symmetrical print.

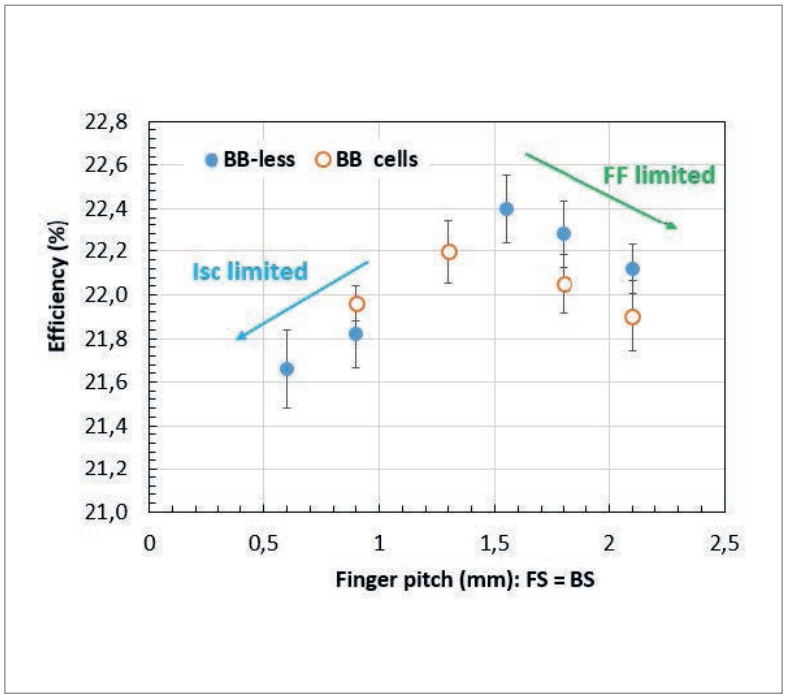


**Figure 5. Conversion efficiency of symmetrical cells.**

## Simulation of optimal bifaciality

To see more precisely how optimal cell bifaciality varies with *BIFI*, the data in Fig. 6(a) were normalized, as shown in Fig. 7(a), to find out the maximum equivalent efficiency for each *BIFI* value. The optimal cell bifaciality is plotted against *BIFI* in Fig. 7(b), which can then be used to select the best print design during cell manufacturing in order to optimize system output.

It is worth noting that the optimal $BF_{cell}$ becomes almost constant for high *BIFI* (92% in this example), while the relative loss rapidly increases for high *BIFI* when using a non-optimal cell bifaciality. The opposite is true at low bifaciality factors. As an example, for $BIFI_5$ the optimal $BF_{cell}$ is 82%, which is very different from the 92% at $BIFI_{40}$. However, if non-optimal cells are used, the relative loss is moderate for low *BIFI* applications, but significant at high *BIFI*. Given this, the best choice for mass production with a single design (or only a few designs) clearly leans towards high bifaciality, or, more precisely, the optimal value for high *BIFI*. Furthermore, this point goes hand in hand with cost reduction, with less silver paste being used on the back-side grid, as reported in Table 1.

In addition to the cell experiments, the module

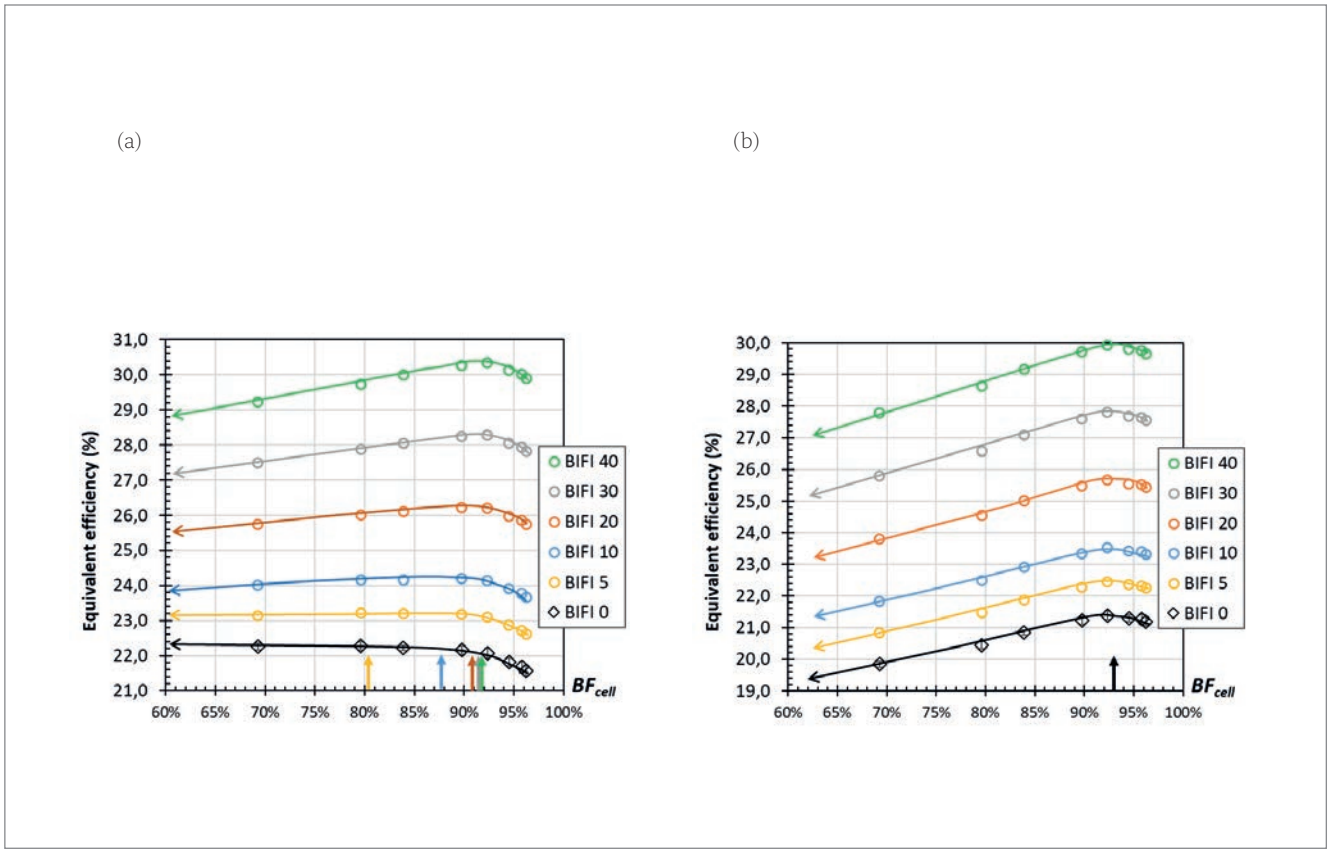


**Figure 6. System output variation as a function of cell bifaciality ($BF_{cell}$) for different percentage of back-side irradiance relative to the front-side irradiance (*BIFI*): (a) tilted system (Equation 1); (b) V-EW system (Equation 2). The solid lines have been added as a visual guide. The arrows indicate the optimal cell bifaciality for each *BIFI*.**

simulation developed in-house was applied to some practical situations. Fig. 8 summarizes the main outputs for 144 half-cell modules incorporating six-busbar M2 cells. For applications without light striking the back side of the cell (*BIFI* = 0), disregarding the silver paste cost issue, the higher the FS cell efficiency, the better the nominal power at STC. As shown in Fig. 8, the optimal grid pattern at $BIFI_0$ is 1.5mm FS and 0.1mm BS, giving 439.5Wp and a module bifaciality of 68.6%. With 300W/m² of light shining on the back side of the module ($BIFI_{30}$), the best cell design is a 1.2mm grid FS and 0.7mm BS. This corresponds to a 92.1% bifacial module delivering 554.5Wp. This design, with a fairly dense grid on the front side, ensures a situation favourable to *FF*. The current remains at a good value thanks to: 1) the 45µm-width fingers considered here; 2) the cell grid shading being lower inside the module; and 3) the significant contribution from the back with a $BIFI_{30}$ factor.

If the 0.1mm pitch for the BS grid is not used when systems with light on the back side are considered, the difference between the best and the worst grid patterns, for both $BIFI_{10}$ and $BIFI_{30}$, corresponds to around a 3% relative difference to the module Wp at STC multiplied by (1 + *BIFI*). As seen on the plot in Fig. 8, at $BIFI_{30}$ this corresponds to 554Wp using a 1.2mm FS/0.7mm BS pattern, and to 538Wp with 2.4/1.3mm. For $BIFI_{10}$, the best output is 477Wp, obtained with 1.5/0.4mm or 1.2/0.4mm grids, and drops to 464Wp with 2.4/1.3mm.

"The best choice for mass production with a single design (or only a few designs) clearly leans towards high bifaciality."

## Conclusion and perspectives

SHJ cells are inherently bifacial and their bifaciality factor ($BF_{cell}$) can be easily tuned, from 0% for a monofacial cell to typically 90% for bifacial cells, and even 100%, but at the expense of front-side efficiency.

For outdoor operation with extra light at the back side (BIFI factor), the effective performance of bifacial systems increases with cell bifaciality ($BF_{cell}$), provided the efficiency decay remains limited. Up to a cell bifaciality of about 90% considered in this work, the precise value depends mainly on the asymmetry of the a-Si:H stacks. The rate of decrease is more pronounced for very high bifaciality because of the drop in front-side (FS) cell efficiency with an increase in $R_s$ (related to both the longer lateral conduction in TCO and the increase in resistivity of the back-side (BS) metal grid), or to the shading of the FS grid.

Thus, an optimal $BF_{cell}$ can be found for a given ratio of back-side to front-side irradiance. From practical cell and module data, when the system bifaciality is varied by means of the screen-printed grid asymmetry, the system output is maximum

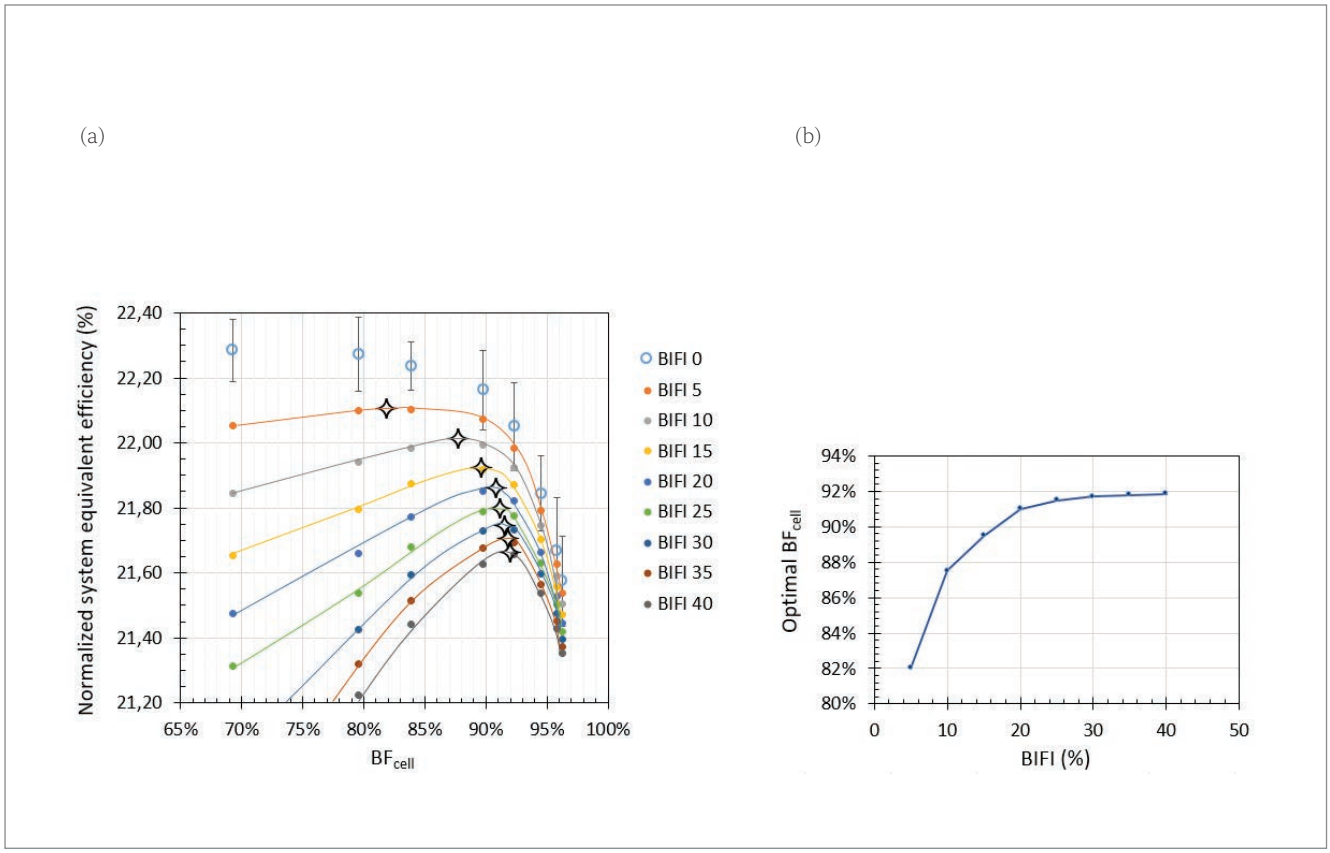


**Figure 7. Cell efficiency without back-side irradiance ($BIFI_{10}$) and estimation of equivalent system efficiency (from the chart in Fig. 6(a)), normalized to the *BIFI* as a function of cell bifaciality. The interpolated lines on graph (a) help to determine the optimal SHJ cell bifaciality, indicated by black stars. This optimal cell bifaciality is plotted against the relative back-side irradiance of the system in graph (b).**

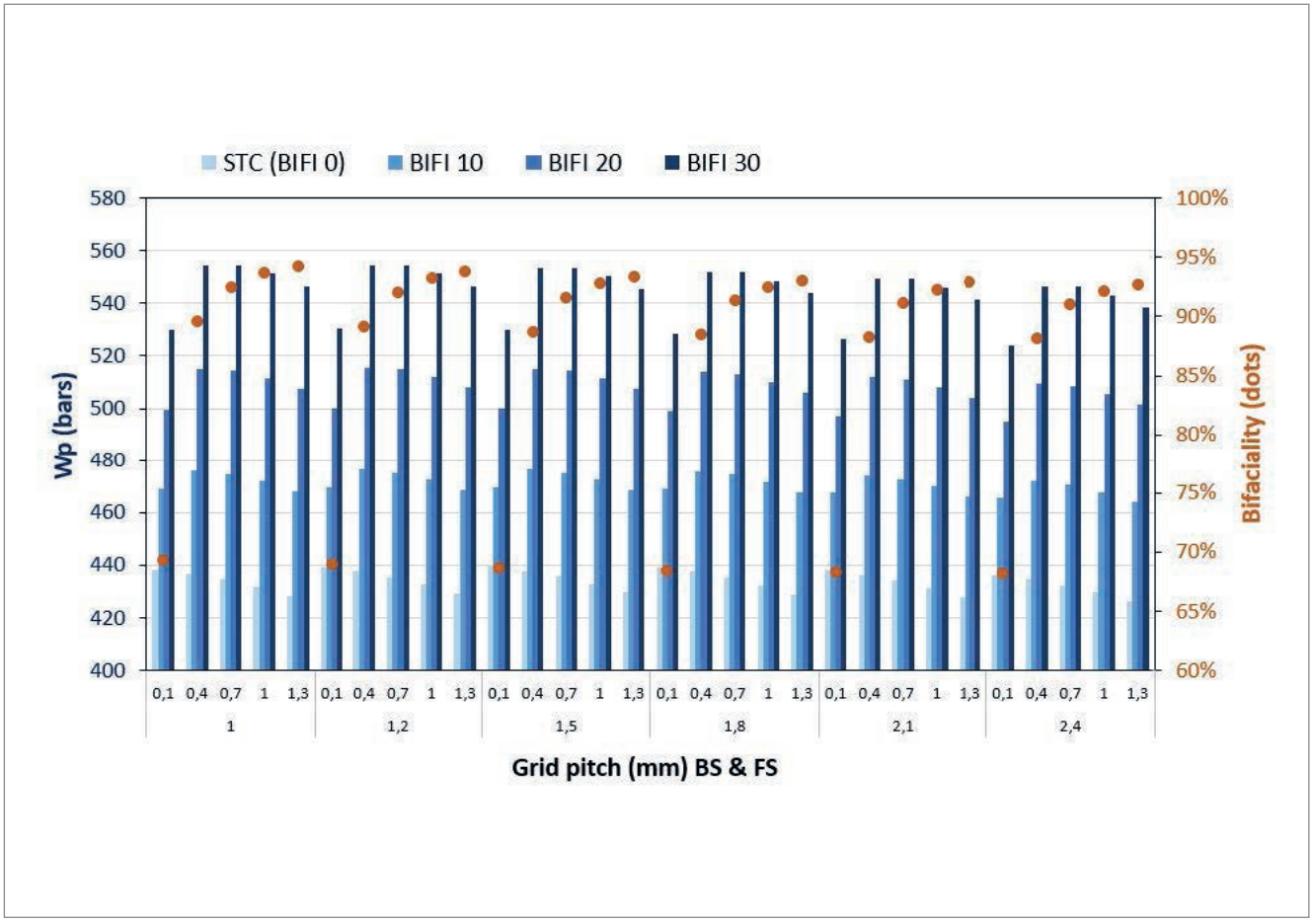


**Figure 8. Simulation data for 144 half-cell (M2) modules with six-busbar prints and various finger pitches (45µm-width considered in all cases), with the power output at STC on the front side and additional *BIFI* on the back side (left scale), and module bifaciality (right scale). The reference cells used in this simulation were processed with PECVD and ITO stacks, optimized for an intrinsic bifaciality of 96.3%, and received a 2.1/0.7mm print, giving an average *I–V* performance of $\eta$ = 22.55%, $V_{oc}$ = 739mV, $I_{sc}$ = 9.342A, *FF* = 79.8% and $BF_{cell}$ = 91.2%.**

for $BIFI_5$ to $BIFI_{30}$, with $BF_{cell}$ ranging from 85% to 95%. This typically corresponds to a FS metal grid pitch from 1.2 to 2mm and a BS pitch from 0.4 to 1mm. With the right optimization of both metal grids for cells with given thin layers, a relative energy gain greater than 1% can be achieved.

For V-EW applications, the optimal cell bifaciality is higher, around 95%, and almost constant, independent of *BIFI*. When considering symmetrical printing, the optimal grid pitch is around 1.5mm, and cell bifaciality is mainly driven by amorphous layer asymmetry.

For monofacial systems, the use of bifacial cells can offer benefits thanks to internal reflection in a glass-backsheet module. The optimization of bifacial SHJ cells for monofacial systems was not experimentally explored in this study, but the model developed to fit and simulate bifacial situations could be used for monofacial applications.

Despite silver printing being the key parameter for $BF_{cell}$, it is important to keep in mind that any progress on layer symmetry, mainly a-Si:H stacks (but also TCO to a lesser extent), can give a global system gain, whatever the type or condition of implementation (bifacial tilted, V-EW, variable *BIFI*, planar connections, monofacial).

Last, but not least, the optimal trend of cell bifaciality ($BF_{cell}$) against relative back-side irradiance (*BIFI*) is reinforced when considering the savings in silver paste when moving to high-bifaciality cells [23]. As an example (see Table 1), for cells optimized with 2.1/0.6mm pitch grids, the average total amount of silver is 127mg/cell. Moving to 2.1/0.9mm grids, cell bifaciality increases by about $2\%_{abs}$ and silver consumption per cell is reduced to 86mg – a 26% saving. For V-EW systems, with the use of an optimized 1.5/1.5mm grid design, cell bifaciality goes to 96.1% and silver consumption is cut to 56mg/cell – a 225% saving!

## Acknowledgement

The authors would like to thank the cell and module R&D teams and pilot production lines at CEA-INES for their contributions (and Joni Mitchell for inspiring the title of this article).

## References

[1] ITRPV 2019, "International technology roadmap for photovoltaic (ITRPV): Results 2018", 10th edn (Mar.) [https://itrpv.vdma.org/en/].

[2] Kopecek, R. et al. 2014, "Bifaciality: One small step for technology, one giant leap for kWh cost reduction", *Photovoltaics International*, 26th edn., pp. 32–45.
[3] 2012–2020, *Proc. Bifi PV Workshops*.
[4] Rodriguez-Gallegos, C.D. et al. 2019, "On the grid metallization optimization design for monofacial and bifacial Si-based PV modules for real-world conditions", *IEEE J. Photovolt.*, Vol. 9-1, pp 112–118.
[5] Kopecek, R. & Libal, J., Eds, 2018, *Bifacial Photovoltaics: Technology, Applications and Economics*. IET.
[6] Rodriguez-Gallegos, C.D. et al. 2018, "Monofacial vs bifacial Si-based PV modules: Which one is more cost-effective?", *Solar Energy*, Vol. 176, pp. 412–438.
[7] Haffner, F. et al. 2020, "The Atacama Desert in Chile as a bifacial hotspot: Yield modelling within the ATAMOSTEC project", *PV Tech Power*, Vol. 24.
[8] Willockx, B. et al. 2020, "Technico-economic study of agrivoltaics systems focusing on orchard crops", *Proc. 37th EU PVSEC* (virtual event).
[9] De Wolf, S. et al. 2012, "High-efficiency silicon heterojunction solar cells: A review", *Green*, Vol. 2, pp. 7–24.
[10] Danel, A. et al. 2019, "Bifaciality optimization of silicon heterojunction solar cells", *Proc. 36th EU PVSEC*, Marseille, France, pp. 224–228.
[11] Danel, A. et al. 2017, "Versatile pilot line to support the heterojunction solar cell industrial development: Busbar and busbar-less configurations", *Proc. 33rd EU PVSEC*, Amsterdam, The Netherlands, pp. 447–450.
[12] Colin, H. et al. 2017, "Energy yield field data of heterojunction-smartwire PV modules", *Proc. 33rd EU PVSEC*, Amsterdam, The Netherlands, 5BV.4.25, poster.
[13] Eisenberg N. & Kreinin, L. 2017, "Understanding energy gain in bifacial PV systems", *PV Tech Power*, Vol. 12, pp. 23–26.
[14] Rodriguez-Gallegos, C.D. et al. 2015, "Analysis and performance of dispensed and screen printed front side contacts on cell and module level", *Proc. 31st EU PVSEC*, Hamburg, Germany, pp. 883–990.
[15] Basset, L. et al. 2018, "Series resistance breakdown of silicon heterojunction solar cells produced on CEA-INES pilot line", *Proc. 35th EU PVSEC*, Brussels, Belgium, pp. 721–724.
[16] Eymard, J. et al. 2019, "Influence of SHJ solar cell bifaciality on the performance of monolithic PV modules", *Proc. 36th EU PVSEC*, Marseille, France, 4AV1.40, poster.
[17] Han, C. et al. 2019, "High-mobility hydrogenated fluorine-doped indium oxide film for passivating contacts c-Si solar cells", *ACS Appl. Mater. Interfaces*, Vol. 11, pp. 45586–45595.
[18] Erfurt, D. et al. 2020, "Aiming for an industrially relevant high-performance TCO for silicon heterojunction solar cells", *Proc. 37th EU PVSEC* (virtual event).
[19] Bivour, M. et al. 2014, "Silicon heterojunction rear emitter solar cells: Less restrictions on the optoelectrical properties of front side TCOs", *Sol. Energy Mater. Sol. Cells,* Vol. 122, pp. 120–129.
[20] Schulte-Huxel, H. et al. 2016, "Flip-flop cell interconnection enabled by an extremely high bifacial factor of screen-printed ion implanted n-PERT Si solar cells", *Proc. 32nd EU PVSEC*, Munich, Germany, pp. 407–412.
[21] Augusto, A. et al. 2016, "Series connection front-to-front and back-to-back of silicon heterojunction solar cells", *Proc. 43rd IEEE PVSC*, Portland, Oregon, USA, pp. 2631–2634.
[22] Favre, W. et al. 2019, "Recent results on the deployment of silicon heterojunction production lines at ENEL Green Power: Influence of the busbar quantity", *Proc. 36th EU PVSEC*, Marseille, France, pp. 235–238.
[23] Faes, A. et al. 2018, "Metallization and interconnection for high-efficiency bifacial silicon heterojunction solar cells and modules", *Photovoltaics International,* 41st edn, pp. 65–76.

"For V-EW systems, with the use of an optimized 1.5/1.5mm grid design, cell bifaciality goes to 96.1% and silver consumption is cut to 56mg/cell – a 225% saving!"

## About the Authors

Adrien Danel holds an M.Sc. in physics and a Ph.D. in microelectronics from INP-Grenoble. From 2004 to 2008 he led the metrology and trace analysis activities at CEA-LETI cleanrooms. He joined CEA-INES in 2009 as the process integration leader on the CEA-INES heterojunction pilot line.

Julien Eymard studied optics, microelectronics and sustainable development at Grenoble INP Phelma and the Institute of Political Studies. Since 2017 he has been a Ph.D. student at CEA-INES, working on the modelling of performance losses in SHJ modules.

Vincent Barth received his Ph.D. in 2014 from the Sorbonne University in the field of organic photovoltaics. He joined CEA-INES in 2017 to work on PV module technology with a focus on interconnection.

Mathieu Tomassini studied physics and chemistry at Joseph Fourier University (Grenoble) before joining 44Solar SARL (Nantes) to work on thin-film solar cell deposition, for which he received his Ph.D. from Nantes University in 2013. He then worked in different areas, from crystalline silicon solar cell defect characterization to PVD process metallization evaluation for organic solar cells. In 2018 he joined CEA-INES, where he works as a process research engineer on the PVD – TCO heterojunction pilot line.

Eric Gerritsen studied physics at Twente University (Netherlands) before joining Philips Research Labs (Eindhoven, NL) in 1985 to work on ion implantation, for which he received his Ph.D. from Groningen University in 1990. He then held various positions at Philips (Lighting, Semiconductors) in Germany, The Netherlands and France, before joining CEA-INES in 2008 to work on PV module technology and applications.

Armand Bettinelli received his Ph.D. in 1987 from Strasbourg University. He worked in industry as a technical manager in the field of high and low cofired ceramics, and then in plasma display panels. In 2005 he joined CEA-INES, where he holds a senior expert position in c-Si solar cell metallization and interconnection.

Charles Roux, head of the CEA-INES HJT lab and pilot line, holds a Ph.D. in II-VI semiconductors from Grenoble University. Prior to joining CEA-INES in 2009, he worked at AMAT as a process engineer in PECVD, PVD, and dry etch for semiconductors. In 2007 he contributed to the start-up of thin-film PV turnkey SunFab at T-Solar in Spain.

## Enquiries

CEA, LITEN
Department of Solar Technologies
INES, F-38000 Grenoble, France

Tel: +33 (0)4 79 79 28 03
Email: adrien.danel@cea.fr

# tandemPV: A review of c-Si-based tandem technology and what is needed to bring it into production

Radovan Kopecek[1], Lejo J. Koduvelikulathu[1], Daniel Tune[1], Daniel Kirk[2], Chris Case[2], Michael Rienäcker[3], Henning Schulte-Huxel[3], Emily Warren[4], Adele Tamboli[4], Robby Peibst[3], Bart Geerligs[5], Sjoerd Veenstra[6] & Gianluca Coletti[5,7]

[1]ISC Konstanz, Germany; [2]Oxford PV, Brandenburg an der Havel, Germany; [3]ISFH, Emmerthal, Germany; [4]NREL, Golden, Colorado, USA; [5]TNO Energy Transition, Solar Energy, Petten, The Netherlands; [6]TNO Energy Transition, partner in Solliance, Eindhoven, The Netherlands; [7]School of Photovoltaic and Renewable Energy Engineering, UNSW, Sydney, Australia

## Abstract

In the last decade the field of PV has become extremely dynamic in terms of implementation of innovations within solar cell development and module production. Al-BSF devices are beginning to fade out as more-advanced and higher-efficiency solar cells and modules enter the PV market. It is believed that c-Si-based tandem solar cells will also be commercially available within three to five years (possibly sooner), as also confirmed in the ITRPV roadmap. This paper provides a concise overview of existing c-Si-based 2-, 3- and 4-terminal tandem technologies, summarizes the current development status, and sets out the future roadmap. In addition, a discussion is included of what will be required over the coming years to bring these promising technologies to market, enabling commercial efficiencies above 30%.

## Introduction

It has become universally accepted that PV will be one of the main technologies to mitigate global warming. Considering that PV has only become cost effective in the last two years – meaning that it is now possible to install PV systems reaching values of levelized cost of energy (LCOE) of US$30/MWh and below without subsidies – we are only at the beginning of this success story. The total worldwide installed power of PV systems up until Q2 2020 was about 650GWp, and it is expected that this figure will reach 1TWp by the end of 2022 [1]. The current module price is around US$0.2/Wp, and there is the potential to reduce this to US$0.1/Wp in the coming years [1]. By 2050 about 30–50TWp of installed PV power is anticipated, which will be about 30–50% of total electricity generation [1]. Which PV technology has been responsible for this magic? It was, and currently still is, crystalline silicon (c-Si)-based PV technology.

In 2009/10 Martin Green proposed that c-Si technology (G1: Generation 1) was a good start for PV but that in the future, Generation 2 (i.e. thin film) and later Generation 3 (i.e. tandem applications) will be needed in order to achieve 'low-cost module regions' below US$0.5/Wp (Fig. 1). Already by 2013 it had become apparent that c-Si technology was more powerful than expected because of rapid technology improvements coupled with the move to mass production in China. Moreover, instead of pursuing further development in different generations, the PV market adopted thousands of small evolutionary innovations in production, reaching lower and lower production cost. Now, in 2020, we are in the middle of the proposed 'G3 area', and it is clear that c-Si will

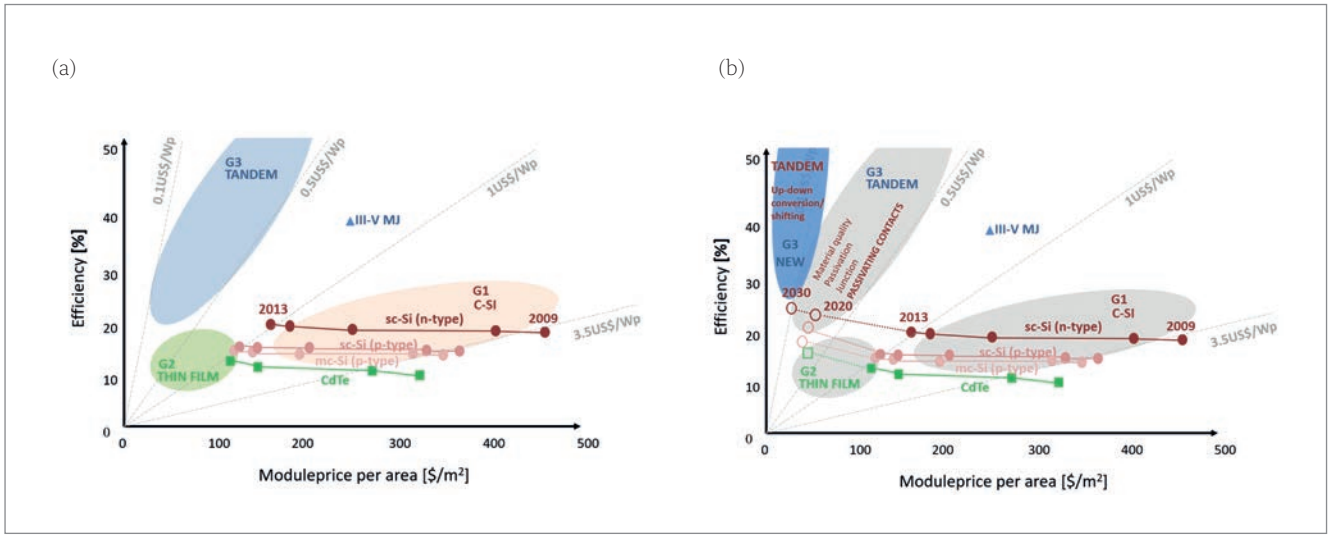


**Figure 1. (a) Forecast from Martin Green [2] for different PV technologies. (b) Reality in 2020 and forecast for 2030.**

"Over the next 10 years it is expected that c-Si technology will be driven to its efficiency and cost limits."

continue to be the leading technology in the near future. Over the next 10 years it is expected that c-Si technology will be driven to its efficiency and cost limits, with modules reaching a low cost of the order of US$0.1/Wp.

At the moment, the lowest cost technology is the so-called standard *passivated emitter and rear contact (PERC)*, but this technology is getting close to its practical efficiency limit of around 23% (with a $V_{oc}$ of about 685mV). Final efforts are being made to break through the 23% ceiling with the inclusion of selective emitters and by using Ga-doped c-Si wafers as standard. The drive to reduce costs further, however, is now being tackled mostly by increasing the substrate sizes from M2–M6 up to M10 and perhaps M12 in the future. Higher module efficiencies for PERC technologies are being achieved with more advanced layouts and interconnection concepts, such as shingling or zero-space connections. In 2020 more n-type concepts have been gaining importance, since efficiencies well above 23% are possible using passivating contacts, including silicon heterojunction (SHJ) technology, but the practical limit of 27% of such concepts is also getting closer. On a fundamental level, the only practical ways to exceed the Shockley-Queisser thermodynamic limit of single-junction photovoltaics is either through the use of up/down conversion layers, or by combining multiple solar cell junctions into so-called *tandem configurations*, which have the potential to achieve commercial efficiencies above 30% in the near term [3].

In this context, many consortia in the EU now believe that the next big step in PV is not an evolution but a small *revolution* – heading towards c-Si-based tandems using standard technology as the low-band-gap bottom cell, different absorbers for the high-band-gap top cell, and different interconnection schemes for the top and bottom cells. Fig. 2 shows the International Technology Road Map for PV (ITRPV) forecast for future c-Si-based technologies.

In the ITRPV roadmap, the fading out of Al-BSF technology can be clearly seen as it is replaced first by standard PERC, and then later by more advanced technologies, such as 'TOPCon' (e.g. the latest record of Jinko of 24.8% [4]), which can produce voltages of over 700mV, and silicon heterojunction reaching 25% efficiency [5]. From 2024/25 onwards, it is anticipated that c-Si-based tandem technologies will begin to appear, but precisely which tandem technologies, and what will be required for this to really happen, will be discussed in the following paragraphs. In order to further support these promising technologies to come onto the market, the first c-Si-based tandem workshop – tandemPV – is also being organized from 2020 onwards (see www.tandemPV-workshop.com).

Apart from economic and market factors, c-Si also exhibits a range of other characteristics that make it suitable as the bottom cell in a tandem architecture; for example, it is abundantly available, inexpensive and efficient, and has a near-ideal band gap for achieving the maximum power conversion efficiency of a tandem solar cell. Last, but not least, there have been impressive industrial developments and achievements in relation to single-junction photovoltaics that are fundamental to the deployment of tandem technology as well. If c-Si solar cells are used just for the bottom cells, many costs can be reduced significantly, with potential savings in, for example, metal paste consumption.

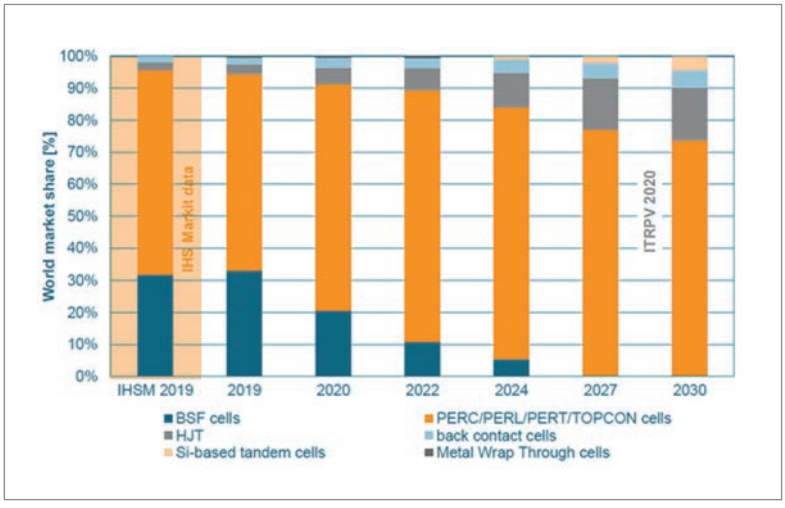


**Figure 2. ITRPV roadmap for future c-Si-based solar cell technologies [1].**

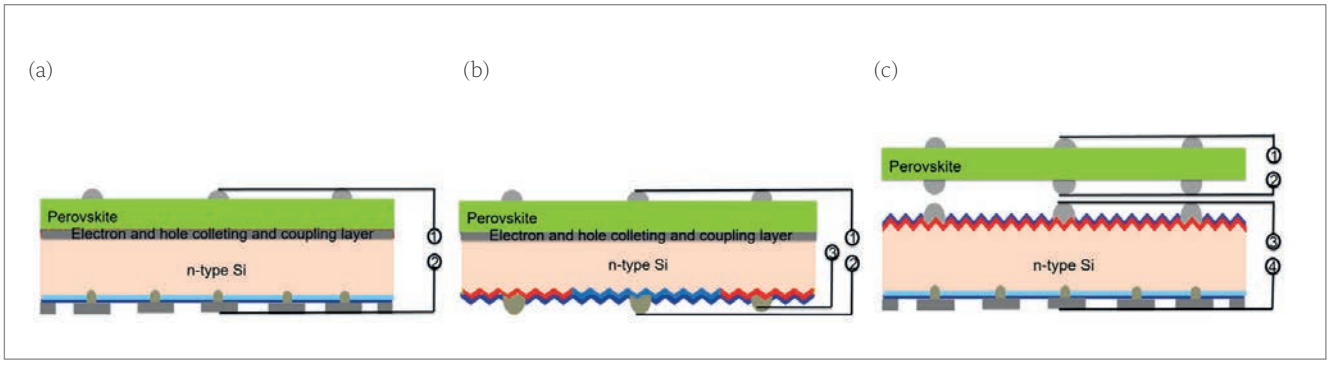


**Figure 3. Schematic cross sections of different tandem geometries: (a) 2-terminal (2T); (b) 3-terminal (3T); (c) 4-terminal (4T).**

## Tandem terminal geometries

For c-Si-based tandem technologies there are several basic geometries that can be used, namely 2-teminal (2T), 3-terminal (3T) and 4-terminal (4T) tandem approaches, as depicted in Fig. 3.

The selection of the c-Si devices best suited to the corresponding technologies is fairly straightforward and depends on the targeted application. However, this concept brings with it the challenge of identifying an efficient top cell.

## Suitable technologies for top cells

As candidates for a thin-film top cell absorber there are many possibilities, including perovskites, GaAs and other III-V devices, CdTe and CIGS, of which some are better and some worse in many respects. The most promising options these days for top cells are metal-halide perovskites and GaAs, with both having their respective advantages and disadvantages. For example, perovskites can be made at low cost but improving the stability is still a major focus of R&D efforts; in contrast, GaAs layers are highly stable but the deposition techniques are still not sufficiently cost effective. There are many groups, however, that are tackling these challenges. In the following paragraphs, the status of the most promising candidate – the perovskite top cell – will be briefly summarized.

Perovskite photovoltaics have been proved to enable silicon to go beyond its single-junction limit. Since their solar absorber properties were first discovered in 2009, perovskites have become one of the most prominent research topics in the PV research community. With exceptionally rapid improvements in efficiency, stability and scalability over the last five years, the potential of perovskite photovoltaics has been grasped and they are now entering their commercial phase. Certified efficiencies are now as high as 25.5% for perovskite single junctions, and 29.15% for 2T perovskite–silicon (PVSK–Si) tandem cells [6]. Advances in efficiency have been supported more and more by progress in

> "The most promising options these days for top cells are metal-halide perovskites and GaAs."

device stability under accelerated ageing tests [7]. A range of deposition techniques exists – from solvent-based to entirely solvent-free coating techniques, and any combination in between – that can be employed to fabricate a perovskite solar cell on top of a silicon bottom cell to form a PVSK-Si tandem solar cell. Perovskites are therefore well suited to conformal deposition on a variety of surface textures [8] and over large areas [9], which is necessary for successful tandem fabrication on a commercial scale.

For PVSK-Si tandems, it is crucial that the overall module stability approaches the level of stability of silicon-only modules, otherwise the benefits of the higher initial efficiency of tandem modules is reduced or eliminated. To ensure this, the continued focus of the PV community on advancing the stability of these cells, and on their evaluation by accelerated ageing tests already in use in the silicon industry, is essential (e.g. IEC 61215). Ultimately, however, extended outdoor testing must be undertaken to verify such testing. Fig. 4 shows the normalized weekly output of two monofacial modules installed at Oxford PV GmbH's manufacturing site in Germany. One module is an industrial 60-cell PERC module and the other, a 60-cell 2T PVSK-Si module. Thus far in the six months of data collected, there is no visible divergence between the performance of the two module types. If anything, the tandem module has increased in performance relative to the PERC module during the year, probably because of the superior high-temperature performance of the tandem module. Clearly, the work of fully validating the reliability and bankability of any new technology takes time, but for 2T PVSK-Si tandems, the signs are good.

## Suitable c-Si technologies for bottom cells

In addition to the quest for a suitable top cell material for the Si-based tandem, the type of c-Si bottom cell and the scheme used to interconnect the

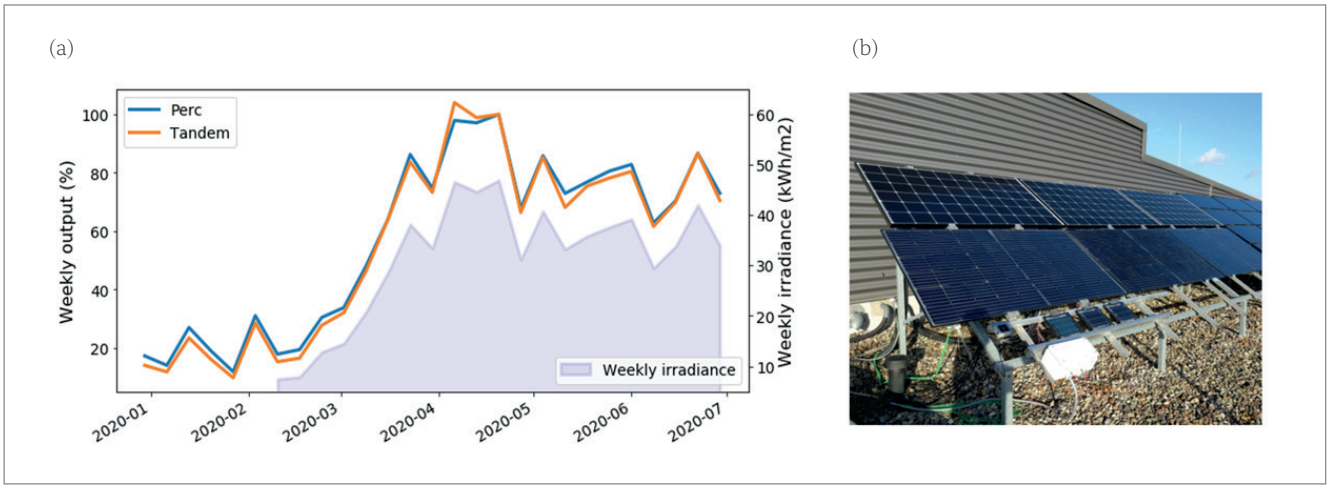


**Figure 4. (a) Normalized weekly output of standard PERC vs. 2T PVSK-Si modules at Oxford PV GmbH's manufacturing site in Germany. (b) The outdoor testing site.**

top and bottom cells are important aspects requiring careful consideration. All interconnection schemes come with their pros and cons, and for c-Si-based tandems these can be summarized as follows.

In a *2T tandem*, the different absorbers are connected in series. This facilitates an easy and straightforward implementation of the tandem solar cells into modules similar to a standard two-side-contacted c-Si module. In *2T and 3T tandems* the top and bottom cells are monolithic in nature. On the one hand, this is beneficial in terms of saving any additional fabrication costs (e.g. glass substrate for the top cells). On the other hand, this quite likely requires process adaptations of a high-temperature c-Si PERC process to incorporate the low-temperature-processed top cell. Additionally, in order to avoid major power losses in *2T tandems*, the series-interconnected top and bottom cells must have their currents closely matched at their maximum power points and this requires thorough band-gap engineering of the top cell's absorber. However, in *3T and 4T tandems*, the top and bottom cells do not need to be current matched, and therefore provide a more flexible choice in band gap for top and bottom cells.

From an industrialization point of view, it is beneficial for any bottom cell technology to be as close as possible to the dominant PERC technology in order for existing production capacities to be upgraded. From a technical point of view, the best-suited bottom solar cells for the 2T approach are two-side-contacted cells with passivating contacts, e.g. SHJ or poly-Si solar cells [10–11], with open-circuit voltages exceeding 720mV. One possible PERC-like bottom cell with a passivating poly-Si front contact with an integrated tunnelling junction was proposed by Peibst et al. [12].

In a *4T tandem*, the two absorbers are physically connected but their electrical operations are independent. This necessitates a relatively complex module implementation – basically having two separate modules on top of each other, which could make this configuration quite costly. On the other hand, this provides the greatest flexibility for achieving the highest efficiency as well as an easy implementation of bifaciality, and without any of the current mismatch losses of the two-terminal configuration. Here, an ideal bottom cell could be the very low-cost but high-efficiency rear emitter passivated emitter rear totally diffused (nPERT) solar cell, since the rear emitter is best suited to red/IR absorption, as well as offering the best use of bifaciality. However, a PERC cell with a poly-Si emitter also has the potential to be a suitable bottom cell for both 2T and 4T tandems [13], with good near-infrared (NIR) response, in particular when Ga doped for good bulk lifetime; moreover, PERC cells can be produced for bifacial operation.

Recently, the *3T tandem* configuration has attracted increasing interest, as it combines the positive aspects of both 2T and 4T tandems. Thus, with a potentially higher energy yield, due to better optics from the monolithic structure and without the intermediate grid of the 4T, the 3T tandem could provide a path towards lower LCOEs. Here, the natural choice is an interdigitated back-contact (IBC) solar cell, since the rear-contact design allows the use of just an interconnection layer(s) between the top and bottom cells.

## 2T tandem technology

Oxford PV is pursuing the commercialization of perovskite technology in a 2T approach for the following reasons:

1. It provides the silicon industry with a viable route to achieving efficiencies beyond 25%.

2. Integration at the cell level minimizes optical and resistive losses.

3. It yields a final module product with higher power, which can be indistinguishable from a standard silicon module in terms of installation and integration.

4. Finally, and most importantly, a cost of ownership analysis has shown that silicon solar cells enhanced with Oxford PV's perovskite solar cell technology will lower the LCOE of a solar installation – a critical consideration for delivering more affordable clean energy and accelerating the adoption of solar energy, thus mitigating the impact of climate change.

Moving from record-efficiency lab-scale devices to a commercially viable product requires the ability to produce perovskite cells on a full-wafer scale. This can be achieved by an appropriate choice of deposition processes. Additional processes are also required – ones that are not used on a small scale. One of the key drivers of efficiency for conventional silicon solar cells has been improvements in metallization technologies – 2T tandem cells similarly require low shading and low resistivity interconnects, with the additional requirement of low process temperature.

Fig. 5 shows that from a subset of the wide variety of pastes available for SHJ cell metallization there are very different responses of resistivity to temperature. Paste D, for example, shows very little difference in resistivity, whether baked at 60°C or 150°C, whereas paste C changes by two orders of magnitude over the same range. As well as the resistivity, which must be low to maximize fill

"The best-suited bottom solar cells for the 2T approach are two-side-contacted cells with passivating contacts, e.g. SHJ or poly-Si solar cells, with open-circuit voltages exceeding 720mv."

factor, the shading must be kept low to maximize current output.

As a demonstration of the scalability, a 4cm² cell was created with screen-printed front electrodes; the device parameters are shown in Table 1, compared with a previously certified 1cm² cell, which does not require a front grid. As can be seen, in contrast to the record cell, there is no change in fill factor, signifying that the electrical properties of the metallization are sufficiently good. There is a slight loss in $J_{sc}$, which is accounted for by the 2.5% shading resulting from the silver fingers. Overall, this yields a high-efficiency cell fabricated using standard industrial metallization techniques.

As is well understood, bifacial cells and modules consistently offer an advantage over their monofacial counterparts. It is often mistakenly thought that, because of their requirements for current matching, 2T tandem cells are incompatible with such energy-yield-enhancing approaches. By using an equivalent circuit model to elucidate the change in response of the device to different photocurrent generation in the two subcells, it is possible to quantify the effects of this divergence from matching, as well as the gains from rear illumination. Since the requirement for current matching exists in these tandem cells, any gain in current from rear illumination is constrained by the top cell current. The model reveals (Fig. 6) that there is always a gain in fill factor as current mismatch increases (as previously reported in Koehnen et al. [14]), which leads to a gain in performance; to maximize the boost in output, it is preferred to adjust the band gap of the PVSK to capture more of the front illumination so that an increase in rear illumination increases the current in the device. Adjusting the band gap of PVSK materials is possible over a very wide range, as shown in Fig. 6, which draws on data from Oxford PV and data from Bush et al. [15]; such tandem cells can therefore take advantage of a bifacial design.

In summary, the 2T terminal approach is compatible with highly efficient, reliable modules, is able to use standard industrial metallization and interconnection approaches, and can demonstrate high energy yield, with the ability to benefit from bifaciality in much the same way as standard silicon modules.

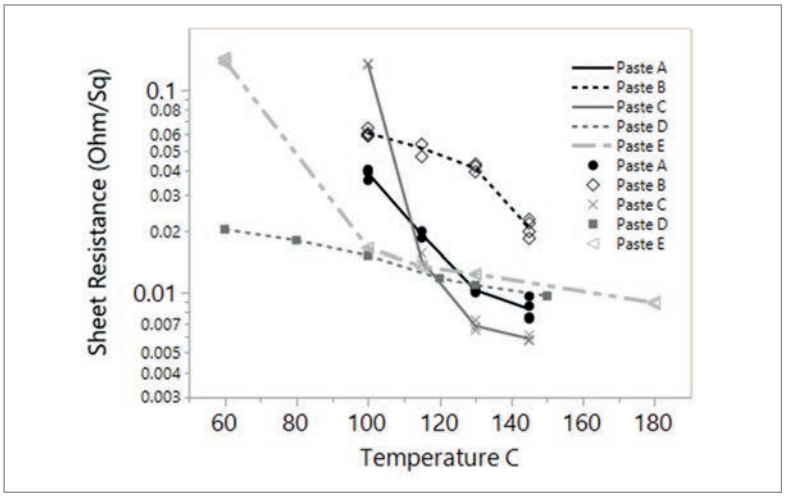


**Figure 5. Measured sheet resistance for various metallization pastes.**

| Cell type | $V_{oc}$ [mV] | $J_{sc}$ [mA/cm²] | *FF* [%] | $\eta$ [%] |
|---|---|---|---|---|
| 1cm² 2T tandem | 1.801 | 19.8 | 78.7 | 28.0 |
| 4cm² 2T tandem | 1.818 | 19.4 | 78.8 | 27.8 |

**Table 1. *I–V* parameters for PVSK-Si tandem cells of different areas.**

## 3T tandem technology

There are many possible ways to construct a tandem solar cell with three terminals from a particular 2T top cell and a 3T interdigitated back-contact bottom cell (3T-IBC). The 3T-IBC cell is the heart of the 3T tandem cell, as it enables the 3T operation, and it is essential to understand the physics and operation principles of the 3T-IBC cell in order to understand the whole tandem cell's operation. Fig. 7 illustrates the operation principles of 3T tandem cells.

The 3T-IBC bottom cell in Fig. 7 has an n-type (silicon) absorber and three carrier-selective contacts. Two of the contacts – the front contact F

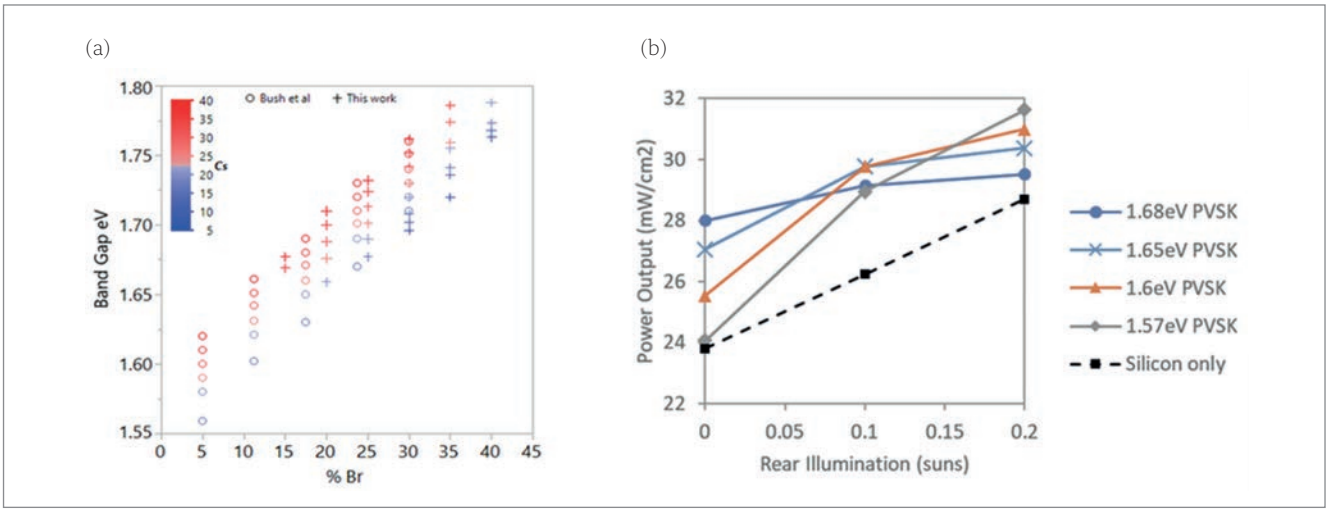


**Figure 6. (a) Control of band gap in PVSK films, and (b) impact on bifacial performance [15].**

inter solar

connecting solar business

The World's Leading Exhibition Series for the Solar Industry

# INTERSOLAR EVENTS 2021

www.intersolar-events.com

## MARCH 22–24, 2021, DUBAI, UAE
www.intersolar.ae

## JUNE 9–11, 2021, MUNICH, GERMANY
www.intersolar.de

## JULY 14–16, 2021, LONG BEACH, USA
www.intersolar.us

## AUGUST 24–26, 2021, SÃO PAULO, BRAZIL
www.intersolar.net.br

## SEPTEMBER 7–9, 2021, MEXICO CITY, MEXICO
www.intersolar.mx

## DECEMBER 2021, MUMBAI, INDIA
www.intersolar.in

## INTERSOLAR SUMMITS WORLDWIDE
www.intersolar-summit.com

FOLLOW US

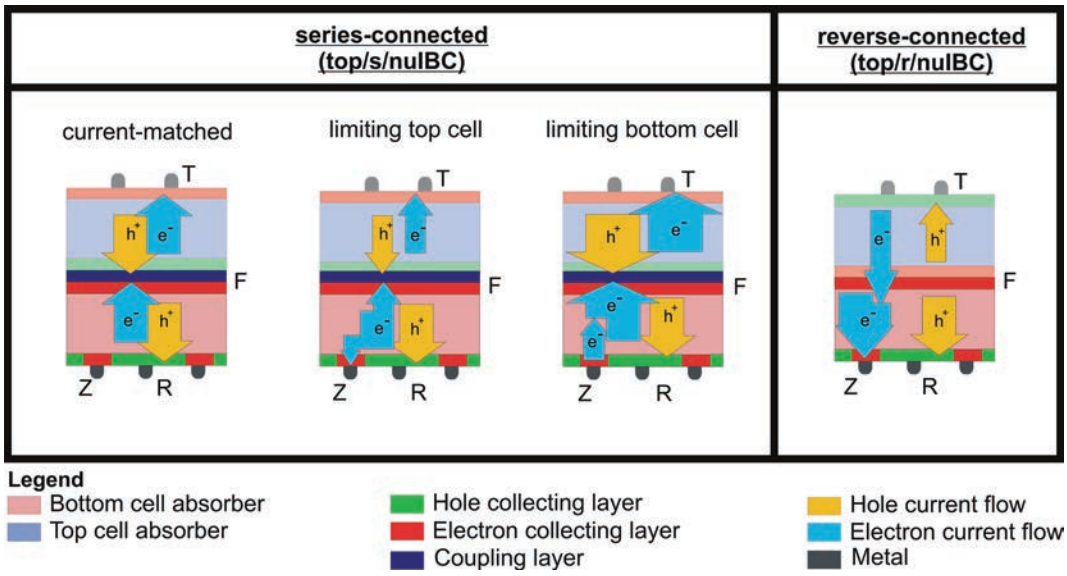


**Figure 7. Different operation regimes of an n-type unijunction 3T-IBC bottom cell (nuIBC) in a series-connected tandem cell (top/s/nuIBC) with current-matched subcells, with current-limiting top cell and with current-limiting bottom cell, or in a reverse-connected tandem cell (top/r/nuIBC). The yellow arrows represent hole current flow and the blue arrows indicate electron current flow.**

and rear contact Z of the bottom cell – are always of the same polarity, e.g. electron-selective in Fig. 7, and the remaining bottom cell's rear contact R has the opposite polarity, e.g. hole-selective in Fig. 7. If the absorber polarity matches that of the two contacts F and Z (as in Fig. 7), then the contacts F and Z are selective for the majority-charge carrier in the absorber. This 3T-IBC cell exhibits two majority-carrier contacts and a single minority-carrier contact, and is referred to as a *unijunction bottom cell* (according to the taxonomy in Warren et al. [16]). In contrast to the unijunction bottom cell, a 3T-IBC bottom cell with two minority-carrier-selective contacts F and Z and a single majority-carrier-contact R is denoted as a *bipolar junction bottom cell* because of its structural similarity with a bipolar junction transistor.

Despite the different architectures and physical descriptions of the unijunction and bipolar junction bottom cells, details of which can be found elsewhere [17–21], both types of bottom cell can be implemented in a 3T tandem solar cell in a similar way. Fig. 7 summarizes the different operation mode of 3T tandem cells comprising a unijunction bottom cell as an example, but which is also applicable to 3T tandems with a bipolar junction bottom cell [16–19].

In a 3T tandem solar cell, the top cell and bottom cell can be series connected as in a usual 2T tandem cell, where the selective contacts of the top and bottom cells with opposite polarity have to be interconnected by a coupling layer – typically a tunnelling or recombination junction. The series connection of the top and bottom cells implies that the current of the top cell's front contact T matches the current of the bottom cell's rear contact R. In a 2T tandem, meeting this current-matching constraint requires an adjustment of the photogeneration currents of the top and bottom cells. For the current-matched example in Fig. 7, this means that each photogenerated hole from the top cell finds a photogenerated electron from the bottom cell at the coupling layer, such that the whole photogenerated electron and hole current in the bottom cell is collected at the respective contacts F and R of the bottom cell. Since no surplus photogenerated electron current remains or is missing in the bottom cell, the additional contact Z is not required.

On the other hand, if the currents of the top and bottom cells are not matched (e.g. because of a varying illumination spectrum or because of mismatched band gaps), the current of a 2T tandem cell would be limited by the cell with the lower current, and the 2T tandem cell would underperform compared with a current-matched tandem cell. In a tandem cell with a limiting top cell (Fig. 7), the hole current of the top cell is less than the electron current from the bottom cell, such that surplus electrons remain in the bottom cell of a 2T tandem and recombine. In a 3T tandem cell, the additional contact Z enables the bottom cell to collect the surplus electrons and to generate extra power.

In a tandem cell with a limiting bottom cell, the photogenerated hole current from the top cell exceeds the electron current from the bottom cell, such that surplus holes remain and recombine in the top cell of a 2T tandem. However, the additional contact Z of a 3T tandem enables the bottom cell to balance the mismatched photogenerated currents of the top and bottom cells at the coupling layer by injecting surplus electrons into the bottom cell, allowing extra power to be extracted from

"A series-connected 3T tandem cell provides a technology platform for maximizing the power output of a tandem cell with current-matched and current-mismatched subcells."

the tandem cell. Ultimately, a series-connected 3T tandem cell provides a technology platform for maximizing the power output of a tandem cell with current-matched and current-mismatched subcells.

To demonstrate the proposed 3T concept, a collaboration of the National Renewable Energy Laboratory (NREL) in the USA and the Institute of Solar Energy Research Hamelin (ISFH) in Germany was able to fabricate the first series-connected 3T GaInP//Si tandem solar cell with an efficiency of 27.3% [22], and a series-connected 3T GaAs//Si tandem cell with 22.3% [23]. The former demonstrates the operation regime of a top-cell-limited tandem cell; the latter, that of a bottom-cell-limited one. Furthermore, Tayagaki et al. [24] have demonstrated a similar 3T GaAs//Si tandem cell.

Besides the series connection of the top and bottom cells, a 3T architecture provides another opportunity – the *reverse connection*, which is unique to the 3T tandem concept and was proposed by Nagashima et al. [25] more than two decades ago. To obtain the reverse-connected 3T tandem cell, the polarity of the top cell in Fig. 7 is flipped, and the top cell exhibits a hole-collecting front contact T and an electron-collecting rear contact. Since the top cell's electron-collecting rear contact meets the electron-collecting contact F of the bottom cell, this architecture does not require a tunnelling or recombination junction and might save the effort of implementing such a junction. Furthermore, it was proposed to use a single charge-carrier-selective layer between the two cells instead of a selective contact for each subcell [26]. The photogenerated electrons from the top cell are injected into the bottom cell, and the additional rear contact Z of the bottom cell collects the injected electrons from the top cell and the photogenerated electrons of the bottom cell. The corresponding holes are collected by the top cell's front contact T and the bottom cell's rear contact R. Even though this device architecture was proposed over two decades ago, Helmholtz Zentrum Berlin in Germany have only just recently managed to fabricate such a reverse-connected 3T perovskite/Si tandem cell, yielding an efficiency of 17.1% [27].

Interestingly, all experimentally demonstrated 3T devices in the literature have so far utilized 3T unijunction bottom cells, probably because of their intuitive operation principles. However, the 3T bipolar junction bottom cell is an attractive alternative, as recently pointed out by Rienäcker et al. [19]; it allows the construction of a lean fabrication process flow for a screen-printed and bifacial 3T-IBC bottom cell which is as simple as that for a PERC cell and reuses most of the fabrication tools for a PERC cell (Fig. 8).

Aside from the 3T cell architecture and technology, an important issue with 3T tandem technology is the integration of this type of cell into PV modules and systems. Interconnecting 3T cells is more complex than 2T or 4T cells, because of the wide variety of configurations and the lack of a simple repeatable unit cell. Gee [28,29], Borden [30], Schulte-Huxel [31,32] and McMahon [13] have shown that voltage-matching 3T devices can produce strings with two terminals and well-understood losses.

## 4T tandem technology

In a 4T tandem configuration the two absorbers are optically coupled and electrically isolated from each other. Because the two solar cells operate independently, there are consequential advantages but at the same time new challenges associated with the deployment of this configuration. The main advantage is that the two devices can be manufactured separately and therefore make use of the best specialized expertise and best specialized cost structure available on the market. In other words, the module manufacturer is free to select a

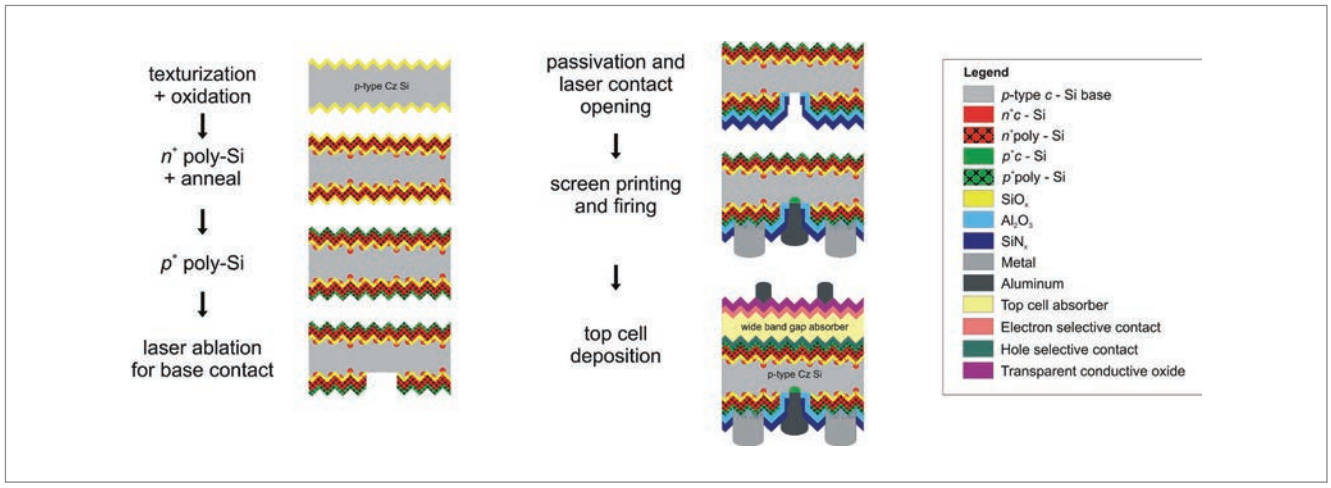


*Reprinted with permission from Rienäcker [21].*

**Figure 8. Proposed fabrication process for a 3T tandem cell comprising a PERC-like 3T bipolar junction bottom cell [19,21].**

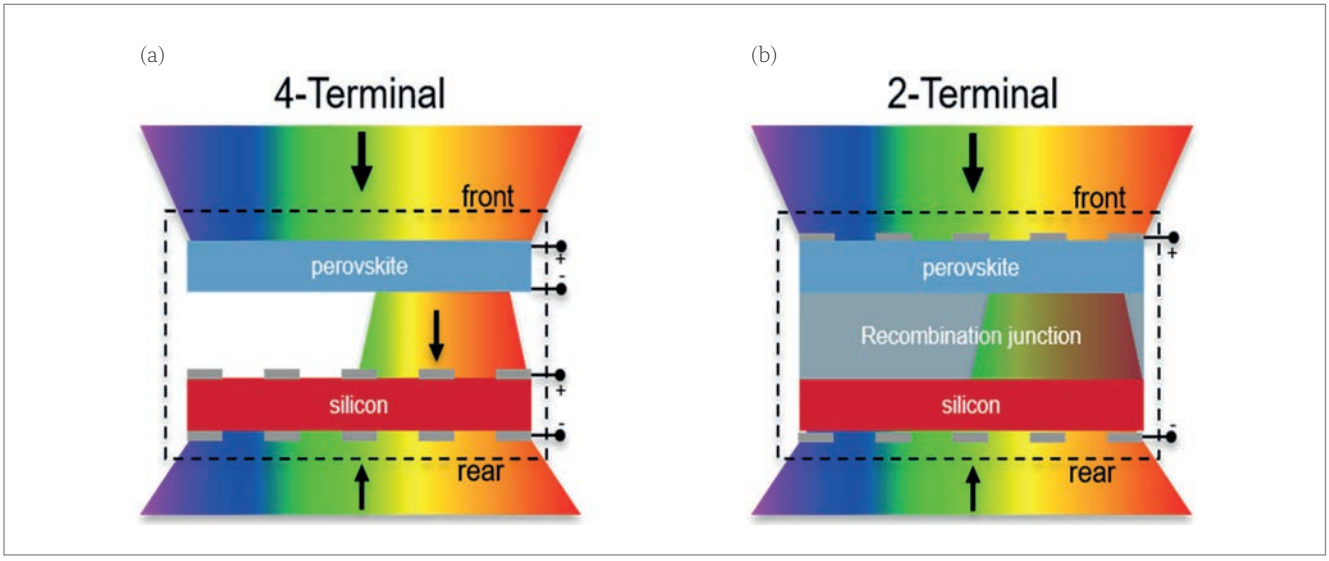


*Reprinted with permission from Coletti et al. [34].*

**Figure 9. Comparison of (a) 4T and (b) 2T bifacial tandem configurations. Photons incident on the front, and possessing energy below the perovskite band gap, reach the silicon bottom device and can be absorbed, while the entire photon spectrum incident on the rear is absorbed by the silicon bottom device. In a 4T tandem the extra rear incident light results in extra power being linearly generated. In contrast, the 2T terminal tandem device needs to be redesigned in order for there to be current matching of the two devices.**

combination of silicon and perovskite devices for hybrid tandem modules. In a market where both technologies are rapidly developing, this can be a major advantage. In addition, the manufacturing operations are simplified because the two devices are optimized and classified separately, avoiding the propagation of any yield problems to the final tandem device.

The drawback is that the complexity is transferred from the manufacturing of the combined devices, as in a 2T configuration, to the module and system levels. Indeed, the interconnection of the respective separate arrays of the bottom and top devices in a module must take into consideration the characteristics of the two cell technologies: among others, silicon cell having high current and low voltage, while thin film having low current and high voltage as well as a different interconnection technology. It is likely that 4T tandems will require new module- and/or system-level power electronics. This explains how the complexity is transferred from the single-cell manufacturing to the module and to the system, which requires increased competencies during the system design and installation as well.

One of the advantages of a 4T configuration is the ease in building on major innovations in state-of-the-art perovskite and silicon PV technologies, such as bifaciality features. In a bifacial tandem module [33–34], the bottom solar cells (i.e. the silicon solar cells in this case) receive light from both sides. While the light received on the front of the bottom cell is 'filtered' (short wavelengths removed) through the perovskite top cell, the light entering from the rear is not. Nevertheless, its spectrum is affected by atmospheric scattering and reflection from surrounding surfaces. The rear incident light can have a dramatic impact on the design and operation of the tandem device.

"The 4T bifacial tandem module can be considered a natural evolution of the performance limit of single-junction silicon-based module technology."

Consider the two major configurations: a 4T tandem and a 2T tandem (see Fig. 9).

Naturally, because of the absence of the need for current matching, 4T (and 3T) devices have the advantage of being suitable for bifacial operation [11]. In a 4T configuration the extra power generated by the bifacial bottom device scales linearly with the rear irradiance, and comes at almost no extra cost compared with a monofacial bottom device, except for the adaptation of the power electronics to the higher power. In a 2T configuration, however, the power production is limited by the requirement for current matching of the top and bottom cells. The performance of 4T and 2T bifacial modules in real-world operation (i.e. in yearly energy yield) has been compared by modelling [33]. While the bifacial 2T tandem device can be designed in such a way that the top device absorbs more photons in order to match the extra current generated in the bifacial bottom device (i.e. for approximate current matching in bifacial operation), this design is then only suitable for a limited range of rear irradiance levels (i.e. for a limited range of environment albedos and system geometries).

Several research groups have recently been working on 4T tandem cells and have reported impressive new findings. The degree of technology development varies, with device areas ranging from a few $mm^2$ to hundreds of $cm^2$. See Table 2 for a list of high-efficiency 4T tandem cells made of a single perovskite cell, typically of area $3\times3mm^2$. The top thin-film device (usually deposited on glass, as in the case of perovskite) is interconnected with typical thin-film module technology [35] combining

| 4T tandem | Description | Size [cm²] | Efficiency top device [%] | Efficiency bottom device [%] | 4T efficiency [%] | Power density Bifi200 | Ref. |
|---|---|---|---|---|---|---|---|
| Solliance – TNO | Pk with MWT-SHJ – Bifacial | 0.09 | 17.0 | 9.5 | 26.5 | 30.5 | [34] |
| UoT – KAUST | Pk with SHJ | 0.049 | 19.0 | 9.2 | 28.2 | - | [37] |
| ANU | Pk with IBC Si | 0.21 | 17.0 | 10.7 | 27.7 | - | [38] |
| Solliance – imec | Pk with IBC Si | 0.13 | 13.8 | 13.3 | 27.1 | - | [39] |
| Solliance – TNO | Pk with MWT-SHJ | 0.09 | 17.0 | 10.0 | 27.0 | - | [40] |
| CAS | Pk with SHJ | 0.1 | 18.3 | 8.7 | 27.0 | - | [41] |
| FAU | Pk with PERL | 0.1 | 17.1 | 9.6 | 26.7 | - | [42] |
| Georgia-Tech | Pk with Topcon | 0.06 | 17.8 | 8.9 | 26.7 | - | [43] |
| KIT – ISFH | Pk with POLO-IBC | 0.06 | 17.5 | 8.2 | 25.7 | - | [44] |
| EPFL | Pk with SHJ | 0.25 | 16.4 | 8.8 | 25.2 | - | [45] |

**Table 2. High-efficiency 4T perovskite/silicon tandem cells.**

laser isolation and conductive layer deposition and resulting in a thin-film module with very high voltage and low current. On a 100cm² aperture area, a perovskite module efficiency of 12% has been achieved in Solliance [36], resulting in a 4T tandem efficiency of about 20% when combined with an MWT-SHJ solar cell.

Despite the performance of the large-area tandem stacks not yet matching the performance of single-junction silicon devices, these initial large-area 4T tandem minimodules demonstrate the promising progress in scalability to industrially relevant areas. Most of the loss observed in the bottom device is due to the relatively lower transparency in the NIR region of the scaled-up device, since the highly transparent conducting oxides (TCOs) of the single cell reported in Table 2 have not yet been implemented in the top minimodule.

Challenges still remain; for example, a major hurdle to overcome is the integration of the bottom and top devices in a module that is capable of lasting at least 25 years, which is the minimum requirement in order to compete with state-of-the-art bifacial silicon modules. The manufacturing of stable, large-area, highly NIR-transparent and high-efficiency perovskite solar modules is the main challenge for the top device. Perovskites, because of the low cost of the constituent materials and the processing (e.g. solution-processed slot die coating, ALD and sputtering), are considered an ideal technology that can be produced at relatively low cost. When combined with the extra energy yield from bifacial configurations, the 4T bifacial tandem module can be considered a natural evolution of the performance limit of single-junction silicon-based module technology.

## Industrial implementation

It is extremely challenging to bring new PV technologies to the market, even if only a few changes are made to the new product, compared with the standard. This has been the experience with bifacial PV. Since the start of the industrial workshop bifiPV2012, work has continued on several related aspects: developing standards, improving bifacial yield simulations, and carrying out more reliable calculations of bankability. These aspects will be targeted during the upcoming TandemPV workshops, but with a slightly different focus. Module lifetime and understanding of degradation mechanisms, as well as recyclability, will also be important aspects to consider when using more complex devices. Coupled assessments of energy yield and additional cost will allow effective evaluations of new tandem architectures [46,47].

The PV industry is a very special one in terms of bringing new products onto the market, because it is not only the cost but also the ongoing increase in lifetime and performance stability of the modules that must be considered. The recent consensus statement on the testing of perovskite solar cell stability [48] provides guidelines and reporting procedures based on the International Summit on Organic Photovoltaic Stability (ISOS) protocols, and represents a key milestone on the way to achieving a rapid industrialization pathway. As in the case of bifacial PV, in order to make the new tandem modules bankable, investors will first have to bring them into large PV fields themselves to prove to the banks that the promised theoretical yield and lifetime simulated through accelerated ageing tests can be validated under real-world conditions in large-scale systems. Only then will banks be willing to invest in large c-Si-based tandem PV systems, which will then allow a real commercial breakthrough of this promising technology.

## Summary and outlook

A brief summary has been provided of some of the most important c-Si-based tandem structures with perovskites as the top cell absorber material. Depending on the evolution of the highly dynamic c-Si market, these tandem technologies will only have the chance to enter the PV market in the

future if the most critical aspects are tackled now. For the roof-top market, the resulting modules do not have to be bifacial; however, if these tandem technologies are to enter the utility-scale and commercial roof-top market, bifaciality will undoubtedly be required. In the coming years, PV for the rapidly expanding field of commercial space applications will be revolutionized by using increasingly low-cost but high-efficiency modules, and c-Si-based tandem technology exceeding 30% efficiency could well be the winning choice in this case (using a p-type c-Si substrate because of better stability in space).

Whatever the future may hold for the dynamic and ever-evolving PV market, one thing is certain – c-Si-based tandem PV will play an important role, and it is anticipated that through this technology, PV cell and module production in Europe will be reinvigorated as well. With that in mind, the authors hope to see you at the TandemPV workshops (www.tandemPV.workshop.com) in the coming years, and look forward to working with you on creating the future of PV technology.

**"Tandem technologies will only have the chance to enter the PV market in the future if the most critical aspects are tackled now."**

## References


[1] VDMA 2020, "International technology roadmap for photovoltaic (ITRPV): Results 2019", 11th edn (Apr.) [https://itrpv.vdma.org/en/].

[2] Green, M. 2009, "Where do we need to go" [http://cleanenergywiki.org/index.php?title=File:Cost-efficiency_pv.jpg].

[3] De Vos, A. 1980, "Detailed balance limit of the efficiency of tandem solar cells", *J. Phys. D: Appl. Phys.*, Vol. 13, p. 839.

[4] Bellini, E. 2020, "Jinko claims 24.79% efficiency for n-type monocrystalline cell", *pv magazine* (Jul.) [https://www.pv-magazine.com/2020/07/20/jinko-claims-24-79-efficiency-for-n-type-monocrystalline-cell/].

[5] TaiyangNews 2020, "25% efficiency for heterojunction solar cell", News report [http://taiyangnews.info/technology/25-efficiency-for-heterojunction-solar-cell/].

[6] Green, M.A. 2020, "Solar cell efficiency tables (Version 56)", *Prog. Photovolt: Res. Appl.*, Vol. 28, pp. 629–638.

[7] Wang, R. et al. 2019, "A review of perovskites solar cell stability", *Adv. Funct. Mater.*, Vol. 29, 1808843.

[8] Nogay, G. et al. 2019, "25.1%-efficient monolithic perovskite/silicon tandem solar cell based on a p-type monocrystalline textured silicon wafer and high-temperature passivating contacts", *ACS Energy Lett.*, Vol. 4, pp. 844–845.

[9] Kamino, B.A. et al. 2019, "Low-temperature screen-printed metallization for the scale-up of two-terminal perovskite–silicon tandems", *ACS Appl. Energy Mater.*, Vol. 2, No. 5, pp. 3815–3821.

[10] Luxembourg, S.L. et al. 2017, "Crystalline silicon solar cell with front and rear polysilicon passivated contacts as bottom cell for hybrid tandems", *Energy Procedia*, Vol. 124, pp. 621–627.

[11] Zhang, D. et al. 2018, "Four-terminal perovskite/c-Si tandem PV technology", *Photovoltaics International*, 40th edn, pp. 66–76.

[12] Peibst, R. et al. 2019, "From PERC to tandem: POLO- and p+/n+ poly-Si Tunneling junction as interface between bottom and top cell", *IEEE J. Photovolt.*, Vol. 9, No. 1, pp. 49–54.

[13] McMahon, W.E. et al. 2020, "Voltage-matched strings using 3-terminal tandems: Fundamentals and end losses", *Proc. 47th IEEE PVSC* (virtual event).

[14] Koehnen, E. et al. 2019, "Highly efficient monolithic perovskite silicon tandem solar cells: Analyzing the influence of current mismatch on device performance", *Sustain. Energy Fuels*, Vol. 3, pp. 1995–2005.

[15] Bush, K.A. et al. 2018, "Compositional engineering for efficient wide band gap perovskites with improved stability to photoinduced phase segregation", *ACS Energy Lett.*, Vol. 3, No. 2, pp. 428–435.

[16] Warren, E.L. et al. 2020, "A taxonomy for three-terminal tandem solar cells", *ACS Energy Lett.*, Vol. 5, No. 4, pp. 1233–1242.

[17] Warren, E.L. et al. 2018, "Maximizing tandem solar cell power extraction using a three-terminal design", *Sustain. Energy Fuels*, Vol. 2, No. 6, pp. 1141–1147.

[18] Rienäcker, M. et al. 2019, "Back contacted bottom cells with three terminals: Maximizing power extraction from current mismatched tandem cells", *Prog. Photovolt: Res. Appl.*, Vol. 27, No. 5, pp. 410–423.

[19] Rienäcker, M. et al. 2019, "Three-terminal bipolar junction bottom cell as simple as PERC: Towards lean tandem cell processing", *Proc. 46th IEEE PVSC*, Chicago, Illinois, USA, pp. 2169–2175.

[20] Stradins, P. et al. 2019, "A simple physical model for three-terminal tandem cell operation", *Proc. 46th IEEE PVSC,* Chicago, Illinois, USA, pp. 2176–2178.

[21] Rienäcker, M. [in preparation], Ph.D. thesis.

[22] Schnabel, M. et al. 2020, "Three-terminal III–V/Si tandem solar cells enabled by a transparent conductive adhesive", *Sustain. Energy Fuels*, Vol. 4, No. 2, pp. 549–558.

[23] VanSant, K.T. et al. [under review], "Design flexibility of 3-terminal tandems: A performance comparison between GaInP//Si and GaAs//Si".

[24] Tayagaki, T. et al. 2019, "Three-terminal tandem solar cells with a back-contact-type bottom cell bonded using conductive metal nanoparticle arrays", *IEEE J. Photovolt.*, Vol. 10, No. 2, pp. 358–362.

[25] Nagashima, T. et al. 2000, "Three-terminal tandem solar cells with a back-contact type bottom cell", *Proc. 28th IEEE PVSC*, Anchorage, Alaska, USA, pp. 1193–1196.

[26] Djebbour, Z. et al. 2019, "Bandgap engineered smart three-terminal solar cell: New perspectives

towards very high efficiencies in the silicon world", *Prog. Photovolt: Res. Appl.*, Vol. 27, pp. 306– 315.
[27] Tockhorn, P. et al. 2020, "Three-terminal perovskite/silicon tandem solar cells with top and interdigitated rear contacts", *ACS Appl. Energy Mater.*, Vol. 3, No. 2, pp. 1381–1392.
[28] Gee, J.M. 1986, "Novel two- and three-junction monolithic multijunction solar cells", *Proc. 2nd Int. PVSEC*, Beijing, China, p. 584 (1986)
[29] Gee, J.M. 1988, "A comparison of different module configurations for multi-band-gap solar cells", *Sol. Cells*, Vol. 24, No. 1–2, pp. 147–155.
[30] Borden, P.G. 1984, "Three-terminal solar cell circuit", US Patent 4,513,168.
[31] Schulte-Huxel, H. et al. 2018, "String-level modeling of two, three, and four terminal Si-based tandem modules", *IEEE J. Photovolt.*, Vol. 8, No. 5, pp. 1370–1375.
[32] Schulte-Huxel, H. et al. 2018, "Energy yield analysis of multiterminal Si-based tandem solar cells", *IEEE J. Photovolt.*, Vol. 8, No. 5, pp. 1376–1383.
[33] Geerligs, L.J. et al. 2018, "4-terminal and 2-terminal tandem modules in bifacial operation model analysis and comparison", *Proc. 35th EU PVSEC*, Brussels, Belgium, pp. 676–680.
[34] Coletti, G. et al. 2020, "Bifacial four-terminal perovskite/silicon tandem solar cells and modules", *ACS Energy Lett.*, Vol. 5, No. 5, pp. 1676–1680.
[35] Di Giacomo, F. et al. 2018, "Up-scalable sheet-to-sheet production of high efficiency perovskite module and solar cells on 6-in. substrate using slot die coating", *Sol. Energy Mater. Sol. Cells*, Vol. 181, pp. 53–59.
[36] Zardetto, V. et al. 2019, "Towards large area stable perovskite solar cells and modules", *Proc. 46th IEEE PVSC*, Chicago, Illinois, USA, pp. 838–840.
[37] Chen, B. et al. 2020, "Enhanced optical path and electron diffusion length enable high-efficiency perovskite tandems", *Nat. Commun.*, Vol. 11, p. 1257.
[38] Duong, T. et al. 2020, "High efficiency perovskite silicon tandem solar cells: Effect of surface coating versus bulk incorporation of 2D perovskite", *Adv. Energy Mater.*, Vol. 10, 1903553.
[39] Jaysankar, M. et al. 2018, "Minimizing voltage loss in wide-bandgap perovskites for tandem solar cells", *ACS Energy Lett.*, Vol. 4, No. 1, pp. 259–264.
[40] Najafi, M. et al. 2019, "Highly efficient and stable rigid perovskite/c-Si and flexible perovskite/CIGS 4-terminal tandems", *Proc. IPEROP-19, Perov. Organ. Photovolt. Optoelectron. Int. Conf.*
[41] Wang, Z. et al. 2020, "27% efficiency four terminal perovskite/silicon tandem solar cells by sandwiched gold nanomesh", *Adv. Funct. Mater.*, Vol. 30, 1908298.
[42] Quiroz, C.O.R. et al. 2018 "Balancing electrical and optical losses for efficient 4-terminal Si–perovskite solar cells with solution processed percolation electrodes", *J. Mater. Chem. A*, Vol. 6, No. 8, pp. 3583–3592.
[43] Rohatgi, A. et al. 2020, "26.7% efficient 4-terminal perovskite–silicon tandem solar cell composed of a high-performance semitransparent perovskite cell and a doped poly-Si/$SiO_x$ passivating contact silicon cell", *IEEE J. Photovolt.*, Vol. 10, No. 2, pp. 417–422.
[44] Gharibzadeh, S. et al. 2020, "2D/3D heterostructure for semitransparent perovskite solar cells with engineered bandgap enables efficiencies exceeding 25% in four terminal tandems with silicon and CIGS", *Adv. Funct. Mater.*, Vol. 30, 1909919.
[45] Werner, J. et al. 2016, "Efficient near-infrared-transparent perovskite solar cells enabling direct comparison of 4-terminal and monolithic perovskite/silicon tandem cells", *ACS Energy Lett.*, Vol. 1, No. 2, pp. 474–480.
[46] Sofia, S.E. et al. 2018, "Economic viability of thin-film tandem solar modules in the United States", *Nature Energy*, Vol. 3, pp. 387–394.
[47] Yu, Z.J. et al. 2016, "Selecting tandem partners for silicon solar cells", *Nature Energy*, Vol. 1, 16137.
[48] Khenkin, M.V. et al. 2020, "Consensus statement for stability assessment and reporting for perovskite photovoltaics based on ISOS procedures", *Nature Energy*, Vol. 5, pp. 35–49.

## About the Authors

Radovan Kopecek obtained a Master of Science from Portland State University, Oregon, USA, in 1995, and received his Diploma in physics from the University of Stuttgart in 1998. He finalized his Ph.D. dissertation in Konstanz in 2002. One of the founders of ISC Konstanz, he has been working at the institute as a full-time manager and researcher since 2007, and is currently the head of the Advanced Solar Cells department. Since 2016 he has also been on the board of directors of EUREC.

Lejo J. Koduvelikulathu received his B.Tech. degree in electronics and telecommunication engineering from Dr. Babasaheb Ambedkar Technological University, Raigad, India, in May 2005. He then obtained his master's in telecommunication engineering and a professional master's in nano–micro systems, both from the University of Trento, Italy, in 2009 and 2010. Since 2018 he has been group leader of the Industrial Solar Cells department at ISC Konstanz.

Daniel Tune is a project manager at ISC Konstanz and holds an honours degree in nanotechnology from Flinders University and a doctorate for his work on carbon nanotube contacted silicon solar cells. He joined ISC Konstanz in 2019 as a project leader, managing and contributing to various national- and European-level projects on next-generation silicon PV modules and technologies.

Daniel Kirk completed his doctoral work in Oxford and joined Oxford PV in 2014. Since 2015 he has been heavily involved in optimization of both perovskite and silicon cells for tandem applications. More recently he has focused on supporting the scaling up the technology to full-wafer scale at Oxford PV, as well as on optimization of the product for commercial realization.

Chris Case is the chief technology officer at Oxford PV. Before that, he ran his own consultancy, providing high-level strategic technology commercialization advice to global companies. He began his career as an assistant professor of engineering at Brown University, and has since worked for a number of companies globally – from large corporates to small start-ups. He has a strong scientific background in patents and IP management.

Michael Rienäcker is a Ph.D. student at the Institute of Solar Energy Research Hamelin, Germany. His work includes the development, characterization and implementation of poly-Si-based passivating, carrier-selective contacts in single-junction and tandem solar cells, and the design, characterization and modelling of 3T IBC cell architectures for tandem applications.

Henning Schulte-Huxel studied physics in Leipzig, Germany, and Bucharest, Romania, as well as laser technology in Jena, Germany. He joined ISFH in 2010, and became a project manager in 2014, with a focus on the module integration of high-efficiency solar cells. Since the end of 2016 he has been the vice head of the module technologies workgroup.

Emily Warren received her Ph.D. from Caltech in 2013 and is currently a staff scientist at the National Renewable Energy Laboratory in Golden, Colorado, USA. Her current areas of research include the design and simulation of high-efficiency tandem solar cells, and the heteroepitaxial growth of III-V semiconductors on Si and other low-cost substrates.

Adele Tamboli received her Ph.D. in materials from the University of California, Santa Barbara, in 2009. She currently works in the Materials Science Center at the National Renewable Energy Laboratory, and holds a joint appointment at the Colorado School of Mines. Her research focuses on improved device architectures for multijunction solar cells, including 3- and 4-T tandems.

Robby Peibst received his Diploma in technical physics in 2005 from the Technische Universität Ilmenau, Germany, and his Ph.D. in the field of microelectronics in 2010 from the Leibniz University of Hanover, Germany. He then joined the Institute for Solar Energy Research Hamelin, where he has headed the Emerging Solar Cell Technologies group since 2013. His research interests include techniques for producing high-efficiency silicon solar cells, such as passivating contacts, silicon-based tandem cells and special applications of PV.

L.J. (Bart) Geerligs is a senior scientist at TNO Energy Transition. Since 2000, he has set up several research programmes at ECN Solar Energy. From 2004 to 2011 he was in charge of n-type cell technology projects, including the transfer to industrial pilot production of nPERT and nMWT technologies. From 2014 he led research on polysilicon passivating contacts, and since 2016 has been in charge of the work on hybrid tandem technology.

Sjoerd Veenstra received his Ph.D. from the University of Groningen, The Netherlands. Since 2018 he has been working for TNO Energy Transition, partner in Solliance, where he is the programme manager of perovskite solar cells and leads the perovskite solar cell team. As of 2019, he is coordinating the perovskite solar cell activities of Solliance.

Gianluca Coletti has a master's in physics from the University of Rome 'La Sapienza', and obtained his Ph.D. from the University of Utrecht in the Netherlands. He is the programme manager of PV tandem technology and applications at TNO Energy Transition, partner in Solliance, as well as an adjunct professor at UNSW Sydney. His research focuses on the development and technology transfer of innovative cell and module technologies.

## Enquiries

Radovan Kopecek
ISC Konstanz
Rudolf-Diesel Straße 15
78467 Konstanz, Germany

Email: radovan.kopecek@isc-konstanz.de

PV TECH TECHTalk Product Series

# A DIFFERENT TYPE OF WEBINAR

## The new way to launch your PV products via the industry's preferred digital platform

**Benefits include**

- Access to the entire audience on the leading PV site
- Proven, popular format of both Product Review and TechTalk webinar
- Brand recognition via co-branded banners online and on PV Tech Newsletter in build up to webinar
- Ongoing exposure via recording of webinar and slides on PV Tech and your own website/social media channels.
- Product Review online and edited version in PV Tech Power journal
- Generation of sales leads
- PV Tech's expertise in marketing in both upstream and downstream – the team has 40 years collective experience in PV marketing

See examples of previous TechTalk Product Series here:
**www.pv-tech.org/on-demand-webinars/list**

For more information and to register your interest in sponsoring your own **TechTalk Product Series webinar** email marketing@solarmedia.co.uk

# Industrial PERC+ solar cell efficiency projection towards 24%

Thorsten Dullweber, Maximilian Stöhr, Christian Kruse, Felix Haase, Birgit Beier, Philip Jäger, Verena Mertens, Robby Peibst & Rolf Brendel, Institute for Solar Energy Research Hamelin (ISFH), Emmerthal, Germany

## Abstract

Monofacial passivated emitter and rear cells (PERC) and bifacial PERC+ solar cells have become the mainstream solar cell technologies in today's PV industry, with conversion efficiencies of around 22.5% being demonstrated in mass production. Ten years ago, the PV market was dominated by monofacial Al-BSF solar cells, with conversion efficiencies around 18%, while the first industrial prototype PERC cells reached 19% efficiency. This paper reviews the key technology improvements which have enabled a continuous 0.5%$_{abs}$/year increase in efficiency of industrial PERC and PERC+ cells. Most importantly, all saturation current density contributions of PERC cells have been steadily reduced, thereby enabling a noteworthy increase in $V_{oc}$ from 620mV in 2010 to 685mV today. A breakdown of all $J_o$ contributions of current industrial PERC+ cells is presented on the basis of actual measurements at ISFH, and a projection is provided of the improvements in $J_o$ of industrial PERC+ cells which are feasible within the next two years, supported by published research results. These $J_o$ values are used as input parameters for Quokka simulations of PERC+ solar cells, according to which an increase in efficiency towards 23.8% within the next two years is predicted. A main limitation of these future PERC+ cells will be the specific saturation current density $J_{o,Ag}$ = 1,400fA/cm² of the screen-printed Ag front contact. When carrier-selective poly-Si on oxide (POLO) fingers are used below the screen-printed Ag contacts, the Quokka simulations predict a further efficiency increase to 24.1% for these so-called *PERC+POLO* solar cells. The simulation results are in good agreement with published efficiencies of the first R&D-type PERC+POLO cells. However, the challenge remains of how to cost-effectively manufacture local poly-Si fingers. The local plasma-enhanced chemical vapour deposition (PECVD) of poly-Si fingers through a shadow mask is proposed as a possible manufacturing solution.

## Introduction

The monofacial passivated emitter and rear cell (PERC) and bifacial PERC+ solar cell [1] have become the mainstream solar cell technologies in the PV industry, exhibiting conversion efficiencies in mass production of around 22.5% and in pilot production of up to 23.0% [2]. For more than a decade, the conversion efficiency of industrial PERC and PERC+ solar cells has continuously increased by approximately 0.5%$_{abs}$ per year [2,3]. As will be described in detail in the following section, the key technology improvements enabling steady increases in efficiency have been:

1. A change from the Al-BSF to the PERC design, applying an $AlO_x$/SiN surface passivation and the continuous optimization of local Al rear contacts, thereby minimizing carrier recombination at the rear ($J_{o,rear}$).
2. Continuous improvements of the phosphorus emitter, including local laser doping, thereby reducing the emitter saturation current density ($J_{o,E}$).
3. Advanced monocrystalline Cz wafers, which have only recently incorporated Ga doping, thereby enabling high and long-term-stable bulk carrier lifetimes.
4. Continuous improvement of the screen-printed front Ag fingers, with significant decreases in fingers widths over the past 10 years, thereby reducing front shadowing and front-contact recombination and enabling the contacting of advanced emitter designs.
5. The bifacial PERC+ design, which enables light harvesting from the rear side of industrial solar cells, thereby further increasing the energy yield of bifacial PV power plants. This has led to record low electricity price tenders below US$0.02/kWh in recent PV power plant auctions.

To predict future PERC and PERC+ efficiency improvements, a previous simulation study suggested that up to 24%-efficient industrial PERC cells could be developed in the future by continuous process improvements [4]. In order to suppress Ag contact recombination, the study assumed that a selective emitter with a very deep doping profile below the Ag contacts can be obtained by a deep phosphorus diffusion followed by a selective etch-back process. However, such a process combination is so far too expensive for industrial production and has therefore not yet been adapted to mass production by PERC cell manufacturers. Instead, several solar cell manufacturers fabricate selective emitters using laser doping [5]; this, however, only slightly increases the phosphorus concentration at the surface of the emitter [6], which is not sufficiently deep to have a strong effect on reducing contact recombination.

Another promising approach to achieving higher industrial cell efficiencies is the use of carrier-selective contacts by implementing a polycrystalline silicon (poly-Si) layer on a thin interfacial oxide layer, called *POLO* [7] or *TOPCon* [8] and their industrial solar cell variants, in particular *PERPoly* [9], *TOPCon* [10] and *monoPoly* [11] solar

cells. These solar cells demonstrate conversion efficiencies of around 23.0% [11] when production-type processing sequences are used. Nevertheless, the processing costs are substantially higher than those for PERC, since TOPCon-like solar cells utilize silver (Ag) contacts on both wafer sides, thus almost doubling the metallization costs compared with PERC [12]. Furthermore, the n-type Cz wafers used for TOPCon are still a bit more expensive than the p-type wafers for PERC, and the boron diffusion takes longer and hence has a lower throughput than a phosphorus diffusion [12]. These may be the reasons why the PV industry has not yet adopted TOPCon, PERPoly and monoPoly as mainstream technologies in multi-GWp production volumes.

This paper shows that the conversion efficiency of today's industrial PERC and PERC+ solar cells is still mainly limited by charge-carrier recombination, and provides a detailed up-to-date breakdown of all Jo contributions. Looking forward, near-term feasible $J_o$ improvements are extrapolated, and the near-term efficiency potential of industrial PERC+ solar cells is simulated. A solar cell design, referred to as *PERC+POLO*, is also simulated, in which 70µm-wide poly-Si fingers located below the Ag metal contacts should drastically reduce charge-carrier recombination. The numerical simulations demonstrate an efficiency potential of up to 24.1% for PERC+POLO solar cells, assuming industrial process technologies. A very similar type of solar cell was presented in 2018 by JinkoSolar and in 2019 by LONGi Solar, with experimental conversion efficiencies of 23.9% [13] and 24.1% [14], respectively, both obtained in R&D. However, JinkoSolar and LONGi did not present any process technology information about the poly-Si finger formation for these solar cells.

A very cost-efficient PERC+POLO manufacturing process is proposed, which implements the well-established PERC+ process and incorporates only one additional process step, specifically the plasma-enhanced chemical vapour deposition (PECVD) of a-Si fingers through a shadow mask. This paper is a shortened version of a recent publication [3], in which details related to the proposed PERC+POLO process sequence, and promising preliminary results of experimental 70µm-wide poly-Si fingers deposited by PECVD through a shadow mask, can be found.

"The conversion efficiency of today's industrial PERC and PERC+ solar cells is still mainly limited by charge-carrier recombination."

## $J_o$ analysis of past, present and future PERC and PERC+ solar cells

In order to predict future technology developments, a common approach in semiconductor technology is to try to extrapolate the technology trends from the past into the future, as (for example) in the case of the regularly published ITRPV Roadmap [15]. Fig. 1(a) shows the record efficiencies of industrial PERC solar cells from 2010 till 2019. The best PERC+ cell efficiencies since their first publication in 2015 [1] are shown as well, with front-side efficiencies

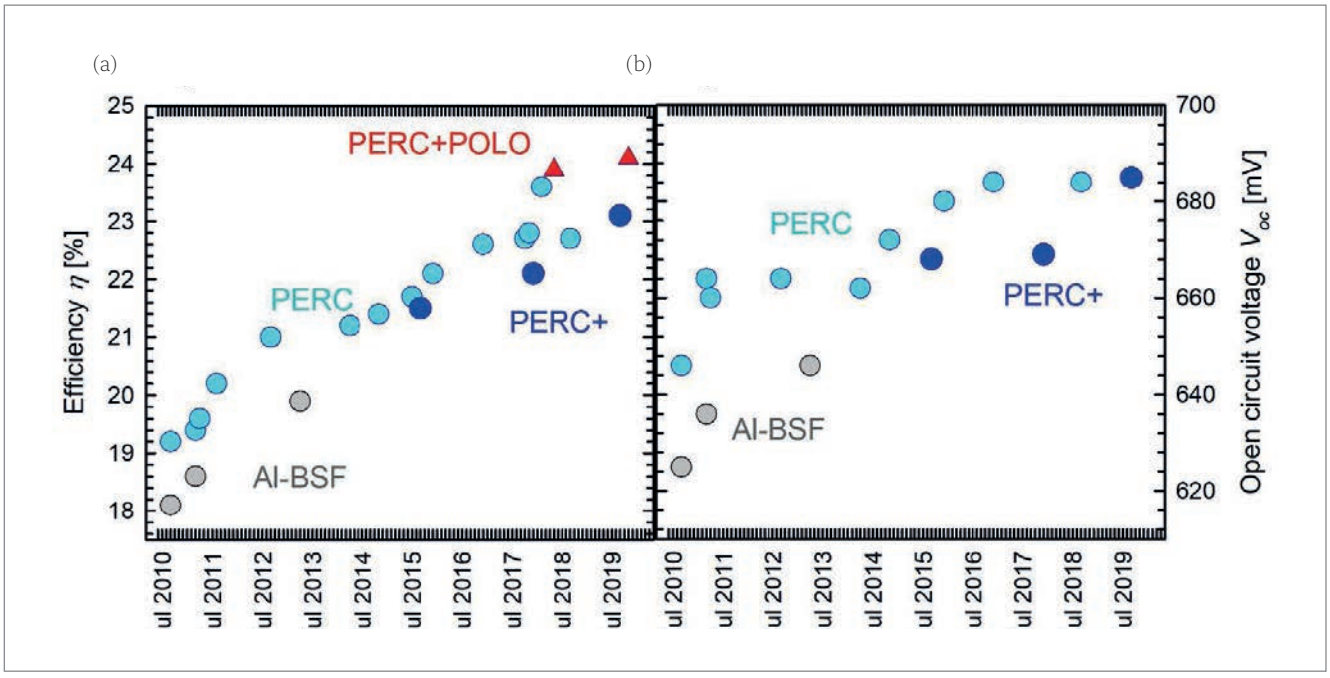


**Figure 1. (a) The record efficiency (light blue dots) of industrial PERC solar cells has constantly increased by about 0.5%$_{abs}$/year from 19.2% in 2010 up to 23.6% in 2019. The best bifacial PERC+ cells (dark blue dots) exhibit similar efficiencies to those of the monofacial PERC cells. The initial R&D-type PERC+POLO cells (red triangles) achieve efficiencies of around 24%. (b) The $V_{oc}$ has improved from 625mV for Al-BSF cells (grey dots) in 2010, to 685mV for industrial PERC+ cells in 2019, thus being a main contributor to the higher conversion efficiencies. Unfortunately, the $V_{oc}$ values of the record PERC+POLO cells have not been published (but simulated values are shown later in Fig. 4). The main reasons for the 5% $_{abs}$ efficiency improvement during the past nine years are explained later in Fig. 2 and Table 1, which also provide a forecast for 2022. (Note that this figure is an updated version of the one given in Dullweber [16], and now includes data from other publications [1,2,13,14,39].)**

| | 2010<br>Al-BSF | Technology<br>improvement | 2019<br>PERC/PERC+ | 2022<br>PERC+ | 2022<br>PERC+POLO |
|---|---|---|---|---|---|
| $f_{Al} \times J_{o,Al\text{-}BSF}$ | 100% × 300fA/cm² | PERC | 4% × 400fA/cm² | 1% × 400fA/cm² | 1% × 400fA/cm² |
| $J_{o,AlOx/SiN}$ | N/A | PERC | 12fA/cm² | 1fA/cm² | 1fA/cm² |
| $J_{o,rear}$ | 300fA/cm² | | 28fA/cm² | 5fA/cm² | 5fA/cm² |
| $J_{o,E}$ | 100fA/cm² | In situ / ex situ oxidation, LDSE | 30fA/cm² | 22fA/cm² | 22fA/cm² |
| $f_{Ag} \times J_{o,Ag}$ | 7% × 1,400fA/cm² | Fine-line Ag print, 0BB | 3% × 1,400fA/cm² | 2% × 1,400fA/cm² | 2% × 35fA/cm² |
| $J_{o,front}$ | 198fA/cm² | | 72fA/cm² | 50fA/cm² | 23fA/cm² |
| $J_{o,bulk}$ | 80fA/cm² | Low $O_i$, Ga | 30fA/cm² | 8fA/cm² | 8fA/cm² |
| $J_{o,total}$ | 578fA/cm² | | 130fA/cm² | 63fA/cm² | 36fA/cm² |
| Calc. $V_{oc}$ | 636mV | | 678mV | 696mV | 711mV |
| $J_{sc}$ | 37.0mA/cm² | PERC, fine-line Ag print | 41.0mA/cm² | 41.0mA/cm² | 41.0mA/cm² |
| Bifaciality | 0% | PERC+ | 80% | 90% | 90% |

**Table 1. Detailed breakdown of the contributions to the reduction of the $J_{o,total}$ from 578fA/cm² in 2010 to 130fA/cm² in 2019, which enabled a large increase in $V_{oc}$ as the main driver for the efficiency improvements shown in Fig. 1. Furthermore, a projection is provided for the expected $J_o$ contributions of PERC+ and PERC+POLO cells in 2022 (which are subsequently used in the Quokka simulations in Fig. 4). The individual $J_o$ values were either measured at ISFH or taken from the literature.**

comparable to monofacial PERC cells. As a reference, the published efficiencies of full-area Al-BSF solar cells are shown, which, however, have been phased out of industrial mass production in favour of PERC and PERC+. The R&D-type PERC+POLO cells of Jinko and LONGi, yielding efficiencies of around 24% [13,14], are also included in Fig. 1(a).

Whereas a typical industrial Al-BSF solar cell in the year 2010 had an efficiency of around 17.5%, today's industrial PERC and bifacial PERC+ solar cells exhibit average conversion efficiencies of around 22.5% in mass production, approaching the record PERC efficiencies of around 23% displayed in Fig. 1(a). This corresponds to an efficiency increase of $5\%_{abs}$ of industrial silicon solar cells within nine years, and a fairly constant efficiency learning rate of around $0.5\%_{abs}$/year during the last decade.

Fig. 1(b) presents the historic trend of the open-circuit voltage $V_{oc}$ of Al-BSF, PERC and PERC+ solar cells, and reveals an increase from 625mV in 2010 to 685mV in 2019, thus indicating it to be a main contributor to the $5\%_{abs}$ efficiency increase shown in Fig. 1(a). The PERC design led to an increase in the $V_{oc}$ of Al-BSF cells of approximately 20mV. Further increases in the $V_{oc}$ of PERC cells mainly originated from improved emitter doping profiles and reduced Ag front-contact area (as explained later in Table 1). Because of their similar device structure, PERC and PERC+ solar cells exhibit very similar $V_{oc}$ values, as can be observed in Fig. 1(b). Unfortunately, the $V_{oc}$ values of the 24%-efficient PERC+POLO cells have not been published (but are simulated to be around 700mV, as will be seen later in Fig. 4). The $V_{oc}$ improvements, together with reduced Ag front-grid shadowing and improved rear optics of PERC, also significantly increased the short-circuit current density $J_{sc}$ from 37mA/cm² in 2010 [17] to 41mA/cm² in 2019 [2]; this too played a big part in the increased conversion efficiency illustrated in Fig. 1(a).

Table 1 lists the most important technology improvements from typical Al-BSF cells in 2010 to typical monofacial PERC and bifacial PERC+ cells in 2019, enabling the continuous increases in the efficiency and $V_{oc}$ of industrial silicon solar cells, as shown in Fig. 1. Since PERC and PERC+ cells exhibit almost identical saturation current density $J_o$ values because of their very similar device structure, their $J_o$ values for 2019 are shown in the combined column '2019 PERC/PERC+' in Table 1. The $J_o$ values stated in Table 1 are either measured for industry-typical PERC and PERC+ cells processed at ISFH, or taken from the literature as indicated in the following paragraphs. Two further columns have been added in Table 1, extrapolating the future $J_o$ reduction and $V_{oc}$ improvement potential for PERC+ and PERC+POLO cells.

The key improvement when moving from Al-BSF cells to PERC cells was the reduction in area fraction $f_{Al}$ of the aluminium rear contacts from 100% to around 4% today, thereby drastically minimizing charge-carrier recombination at the rear metal contact. Fig. 2 shows two scanning electron microscopy (SEM) cross-section images for (a) a 19.4%-efficient ISFH PERC cell in 2010 [17], and (b) a 22.3%-efficient ISFH PERC+ cell in 2019. As can be seen, the early PERC cells had around 100µm-wide line-shaped alloyed Al contacts, which contacted around 10% of the rear area.

"The key improvement when moving from Al-BSF cells to PERC cells was the reduction in area fraction of the aluminium rear contacts from 100% to around 4% today."

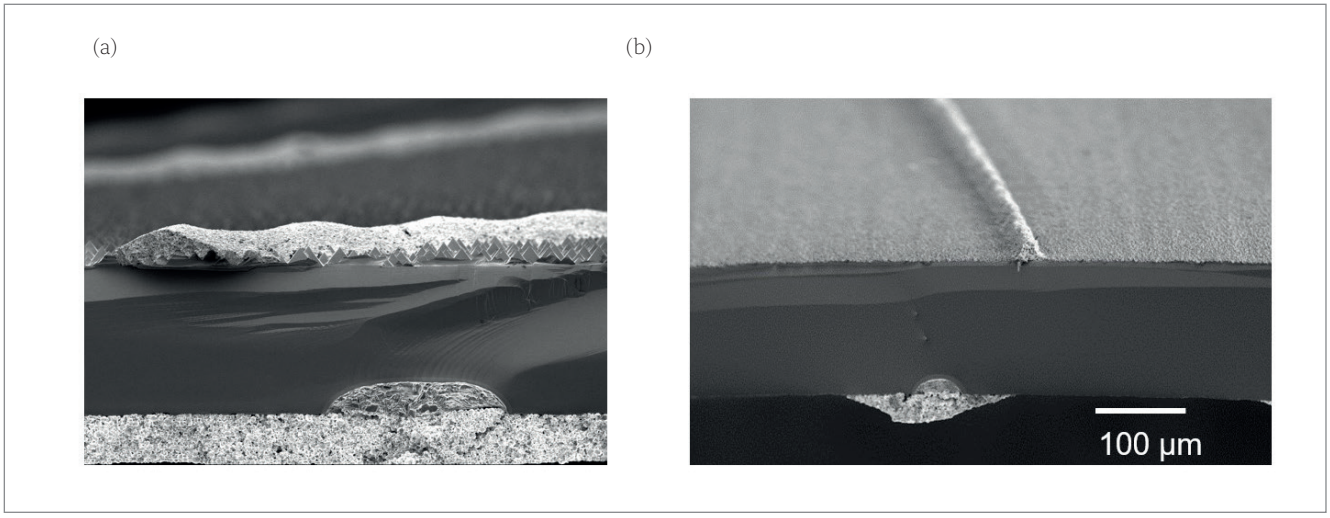


**Figure 2. Scanning electron microscopy (SEM) images of: (a) the 19.4%-efficient ISFH PERC record cell in 2011 (see Fig. 1); and (b) a 22.3%-efficient ISFH bifacial PERC+ solar cell from 2019. Whereas the Si wafer thickness has remained constant at about 180µm, the Ag finger widths have been reduced from around 100µm in 2010 to around 35µm in 2019, thus minimizing light reflection and front-contact recombination. The Al-BSF contact-area fraction has been reduced from 100% for Al-BSF cells to around 10% for the early PERC cells in 2010, and to around 4% for today's PERC+ solar cells. Although the *y* axis is the same for both SEM images, the *x* axis in image (a) is stretched by a factor of 1.4, since the PERC cell has been broken in a 45° angle to the metal fingers. In (b), the cell has been broken in a 90° angle to the Ag fingers.**

By improving the laser contact opening pattern and the Al paste chemistry it was possible to further reduce the Al contact-area fraction to around 4% while maintaining a well-alloyed aluminium back surface field (Al-BSF), enabling fairly low $J_{o,Al\text{-}BSF}$ values around 400fA/cm², as described in the review in Dullweber [16], as well as according to ISFH internal measurements. Additionally, the Al fingers of PERC+ cells limit the diffusion of Si into the Al paste during firing and hence slightly deeper Al-BSFs and lower $J_{o,Al\text{-}BSF}$ values [18] may be obtained. In any case, the specific $J_{o,Al\text{-}BSF}$ = 400fA/cm² of PERC and PERC+ is only slightly higher than that for full-area Al-BSF contacts with $J_{o,Al\text{-}BSF}$ values around 300fA/cm² [17]. Hence, the total area-weighted $J_o$ contribution of the Al rear contacts has decreased from 300fA/cm² in 2010 to just 16fA/cm² in 2019.

In the next few years, it is expected that

improved LCO geometries and Al pastes will further reduce the Al contact-area fraction to around 1% without increasing the specific $J_{o,Al\text{-}BSF}$, as already demonstrated in Peng et al. [19] and Tsuji et al. [20], thereby minimizing the area-weighted $J_o$ contribution of the Al rear contacts to just 4fA/cm², as shown in Table 1. At the same time, the $AlO_x/SiN_y$ rear passivation covering almost 100% of the PERC+ rear side contributes a $J_{o,AlOx/SiN}$ of only 12fA/cm² to the total $J_o$ [21] as a result of its excellent passivation properties. It is expected that $J_{o,AlOx/SiN}$ will be reduced to 1fA/cm² in the next few years by continuous process optimization, as this value has already been measured on test structures at ISFH. Accordingly, the total rear-side saturation current density $J_{o,rear}$, which is the sum of the area-weighted contributions of $J_{o,Al\text{-}BSF}$ and $J_{o,AlOx/SiN}$, has dropped from 300fA/cm² in 2010 to 28fA/cm² in 2019, and is expected to further decrease to just 5fA/cm² in 2022.

Another important contribution to increases in efficiency and $V_{oc}$ has been the reduction of the emitter saturation current density $J_{o,E}$ from around 100fA/cm² [22,23] back in 2010 to today's values of around 30fA/cm² [24,25] by developing advanced emitter doping profiles with reduced phosphorus surface concentrations through applying techniques such as in situ [26–28] and ex situ oxidation [25,29]. The advanced diffusion processes reduce $J_{o,E}$ while maintaining an emitter sheet resistance below 150Ω/sq., which allows a wide spacing, greater than 1mm, of the Ag front-contact fingers. Just as important were new developments, such as improved Ag pastes and laser-doped selective emitters (LDSE) [5,6], which enabled the electrical contacting of the advanced doping profiles. It is expected that this trend will continue and that $J_{o,E}$ values of 22fA/cm² will be obtained in production in the coming years, since such low $J_{o,E}$ values have already been published in R&D [24,25].

One of the most important contributions to increased crystalline silicon solar cell conversion efficiencies in the last few decades has been the continuous improvement of the front Ag pastes. Improved Ag paste chemistries have made possible much narrower Ag finger widths [30], thus reducing the optical shadowing loss and metal contact charge-carrier recombination loss. Improved Ag pastes have also allowed the contacting of lightly doped emitters as stated earlier. The two SEM images in Fig. 2 demonstrate the huge progress in reducing the front Ag finger widths from approximately 100µm in 2010 to around 35µm in 2019, according to Lorenz et al. [30]. Consequently, the metallization area fraction $f_{Ag}$ of the Ag front fingers has fallen from 5% in 2010 to around 2.5% in 2019.

"Another promising approach to reducing metal contact recombination is the use of carrier-selective contacts, which entails the application of polycrystalline silicon on thin interfacial oxide."

Simultaneously, the busbar design has also changed during the past nine years. Whereas in 2010, typically three busbars were printed with fire-through Ag pastes, contacting around 2% of the front surface, today's PERC+ cells often utilize non-fire-through busbar pastes and/or advanced multi-busbar designs [31], which cover less than 0.5% of the wafer front surface. In consequence, the total contacted area fraction $f_{Ag}$ (Ag fingers and busbars) has decreased from around 7% in 2010 to around 3% in 2019 (see Table 1).

For the front Ag contacts, a specific $J_{o,Ag}$ = 1,400fA/cm² is determined by a detailed carrier lifetime measurement and subsequent numerical modelling using Quokka. This value is within the range of previously reported $J_{o,Ag}$ values, specifically from 200 to 2500fA/cm² [29,32–34], which depend in particular on the sheet resistance and doping profile of the phosphorus emitter. Assuming a similar $J_{o,Ag}$ of up to 1,400fA/cm² back in 2010, the area-weighted $J_o$ contribution of the Ag front contacts

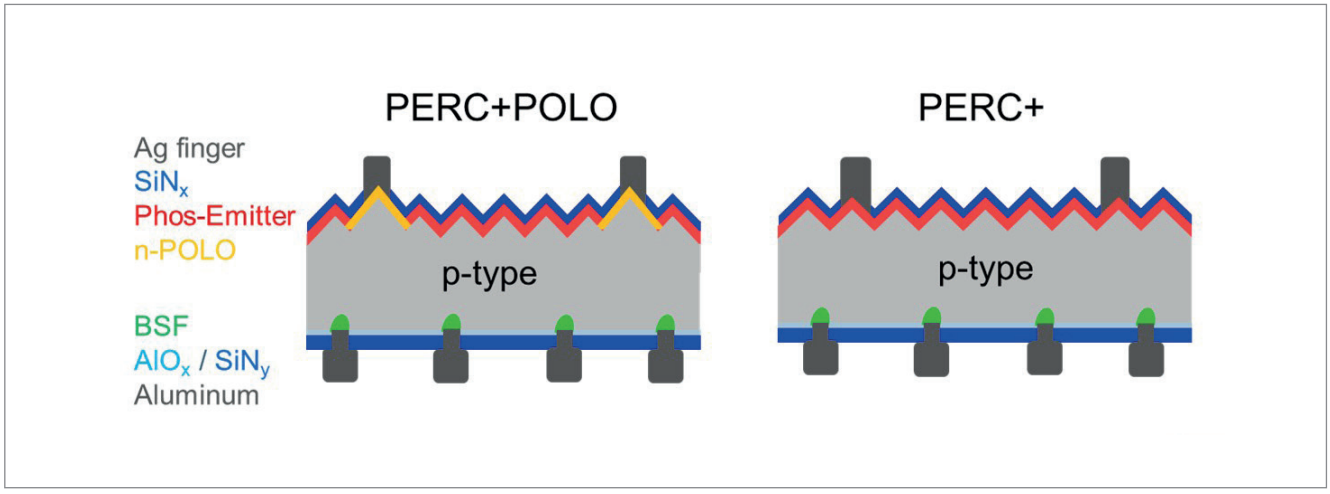


**Figure 3. Schematic drawings of PERC+POLO and PERC+ solar cells. The poly-Si on oxide (POLO) finger below the Ag finger drastically minimizes the front-contact recombination.**

has decreased from 98fA/cm² in 2010 to 42fA/cm² in 2019, as indicated in Table 1. The possibility of further reductions in the Ag finger width towards 25µm in the next few years [30] is expected, hence further reducing the contacted area fraction $f_{Ag}$ to an anticipated 2% in 2022.

It is quite challenging, however, to reduce the high $J_{o,Ag}$ of 1,400fA/cm². One solution to suppress Ag contact recombination is the use of selective emitters with a very deep doping profile below the Ag contacts [29]. Unfortunately, the industry-typical laser-doped selective emitter forms only a shallow emitter, since the higher laser intensities required for deep doping cause melting of the silicon pyramids [6]. Other techniques, such as deep phosphorus diffusion followed by a selective etch-back process [22], are likely to be too expensive for industrial production and hence have not yet been adapted to mass production.

Another promising approach to reducing metal contact recombination is the use of carrier-selective contacts, which entails the application of polycrystalline silicon on thin interfacial oxide, referred to as *POLO* [7] or *TOPCon* [8] and their industrial solar cell variants. It has been shown that the carrier recombination at the screen-printed Ag metal contacts can be minimized to 35fA/cm² with carrier-selective poly-Si contacts [35]. When weighted with the contact-area fraction of 2%, the recombination at the Ag/poly-Si contact is well below 1fA/cm². Hence, in Table 1 the column 'PERC+POLO 2022' has been introduced on the right, where it is suggested to insert a poly-Si finger below the Ag finger of a PERC+ solar cell, similarly to Jin [13] and Fan et al. [14].

A schematic drawing of the PERC+POLO cell in comparison to an industry-typical PERC+ cell is shown in Fig. 3. The total front-side saturation current density $J_{o,front}$, which is the sum of the area-weighted contributions of $J_{o,Ag}$ and $J_{o,E}$, has fallen from 198fA/cm² in 2010 to 72fA/cm² in 2019, thus making it the main $V_{oc}$ limitation of today's PERC and PERC+ solar cells. Advanced emitters and the PERC+POLO cell design are expected to reduce $J_{o,front}$ to 23fA/cm² in 2022.

Finally, the saturation current density $J_{o,bulk}$ of p-type Czochralski (Cz) silicon wafer material has also been reduced, from around 80fA/cm² [36] in 2010 to around 30fA/cm² in 2019 [37], by improving the wafer quality, by reducing the oxygen content and by regeneration procedures minimizing boron–oxygen defect recombination (see, for example, the review in Dullweber [38]). Here, $J_{o,bulk}$ is reported at a carrier density of $1\times10^{15}$cm$^{-3}$, which corresponds to $V_{oc}$ conditions. The $J_{o,bulk}$ values at maximum power point are slightly higher because of the injection dependence of the bulk carrier lifetime. In the past decade, the p-type Cz wafer resistivity has decreased from around 2Ωcm in 2010 to around 1Ωcm in 2019 [37], which enables a wider Al finger spacing of greater than 1mm and hence an increased bifaciality of PERC+ solar cells. It is expected that the improvement of the p-type Cz wafer material will continue and enable $J_{o,bulk}$ values as low as 8fA/cm², as evidenced by today's best R&D Cz wafers utilizing Ga doping or extremely low oxygen concentrations [37].

Adding up the individual area-weighted saturation current density contributions in Table 1 by applying Equation 1 results in a total $J_{o,total}$ = 578fA/cm² for the Al-BSF cell in 2010.

$$J_{0,\text{total}} = f_{Ag}\times J_{0,Ag} + \left(1-f_{Ag}\right)\times J_{0,E} + J_{0,\text{bulk}} + f_{Al}\times J_{0,Al} + \left(1-f_{Al}\right)\times J_{0,Al} \quad (1)$$

$$V_{oc} = \frac{nkT}{q}\times \ln\left(\frac{J_{sc}}{J_{0,\text{total}}}\right) \quad (2)$$

When a one-diode model is applied according to Equation 2 with ideality factor $n$ = 1 and short-circuit current density $J_{sc}$ = 37mA/cm² [17], this $J_{o,total}$ value corresponds to a $V_{oc}$ of 636mV for the Al-BSF cell, which closely agrees with measured $I$–$V$ parameters at that time [17].

For the PERC+ cell in 2019, a $J_{o,total}$ value of 130fA/cm² is obtained, corresponding to a $V_{oc}$ of 678mV when $J_{sc}$ = 41mA/cm² is assumed [2]. This number is not far off the $V_{oc}$ of around 680mV of today's typical PERC+ cells [2]. It should be noted that the largest $J_{o,total}$ contribution of 42fA/cm² originates from the recombination at the Ag front contacts. ISFH's extrapolation of the PERC+ parameters to 2022 predicts a $J_{o,total}$ value of 63fA/cm², corresponding to a calculated $V_{oc}$ of 696mV, which is limited, again, mainly by $f_{Ag}\times J_{o,Ag}$ = 28fA/cm².

Finally, the extrapolation to 2022 for the PERC+POLO cell results in the smallest $J_{o,total}$ value of 36fA/cm², corresponding to a calculated $V_{oc}$ of 711mV. Experimental evidence for this fairly high calculated $V_{oc}$ of PERC+POLO cells is given by measured implied open-circuit voltages i$V_{oc}$ of up to 712mV [25] for PERC+ solar cells processed at ISFH without metal contacts; this corresponds to a total $J_{o,iVoc}$ = 35fA/cm². According to Table 1, the i$V_{oc}$ values of PERC+ test structures differ from the $V_{oc}$ values of PERC+POLO cells mainly by the $f_{Al}\times J_{o,Al\text{-}BSF}$ contribution, which is only 4fA/cm² in the 2022 scenarios. Since $f_{Ag}\times J_{o,Ag}$ for PERC+POLO is less than 1fA/cm² and the $f_{Al}\times J_{o,Al\text{-}BSF}$ is only 4fA/cm², it is expected that the $J_{o,total}$ for PERC+POLO will only increase by 5fA/cm², from 31 to 36fA/cm², after metallization; hence, the cell $V_{oc}$ for PERC+POLO will be close to the i$V_{oc}$ of 712mV of PERC+ cells without metal contacts [25].

Another important improvement which significantly increases the energy yield of PERC solar cells and modules is the introduction of bifacial PERC solar cells called *PERC+* [1], where an

"Quokka simulations confirm that PERC+POLO cells yield higher $V_{oc}$ values and higher conversion efficiencies, compared with PERC+ solar cells."

| Parameter | Value |
|---|---|
| Wafer resistivity | 0.9Ωcm |
| Wafer thickness | 170µm |
| Front-contact shadowing | 3.0% |
| Emitter sheet resistance $R_{sh}$ | 133Ω/sq. |
| Specific contact resistance, front | 1.5mΩcm² |
| Specific contact resistance, rear | 1.3mΩcm² |

**Table 2. Input parameters used for the Quokka simulations in Fig. 4, as measured at ISFH. The $J_o$ and $f$ values for the different PERC+ and PERC+POLO scenarios were taken from Table 1.**

Al finger grid is applied on the rear side. Whereas the full-area Al-BSF cells in 2010, as well as the first commercial PERC cells, were monofacial with 0% bifaciality, today's PERC+ solar cells exhibit a bifaciality of up to 80% [1,2,16]. Between now and 2022, the bifaciality of PERC+ solar cells is expected to increase to 90% through further reductions of the Al finger width in combination with multi-busbar module designs as outlined in Dullweber et al. [39].

## Quokka simulations of the near-term PERC+ efficiency potential

The conversion efficiency potential of PERC+ and PERC+POLO solar cells is assessed in detail by means of numerical simulations by applying the conductive boundary model [40] as implemented in the Quokka software [41]. Two topical scenarios are simulated for PERC+ and PERC+POLO cells. The 'PERC+ 2019' scenario uses all $J_o$ and $f$ parameters as stated in the '2019 PERC/PERC+' column in Table 1. The 'PERC+POLO 2019' scenario also applies the $J_o$ and $f$ parameters as stated in the '2019 PERC/PERC+' column in Table 1, except for the $J_{o,Ag}$ value, where 35fA/cm² is used for the Ag on POLO contact instead of 1,400fA/cm² for the Ag on phosphorus emitter contact. All other input parameters for both scenarios are given in Table 2 and were measured at ISFH. The 'PERC+POLO 2019' scenario assumes 90µm-wide poly-Si fingers in order to account for possible misalignment between poly-Si structuring and Ag screen printing. The optical absorption of the 90µm-wide poly-Si fingers is included in the 'PERC+POLO 2019' scenario using a ray-tracing approach with optical constants according to Reiter et al. [42] and Min et al. [43].

| | $\eta$ [%] | $V_{oc}$ [mV] | $J_{sc}$ [mA/cm²] | $FF$ [%] |
|---|---|---|---|---|
| ISFH PERC+ cell | 22.3 | 683 | 40.4 | 80.8 |
| PERC+ 2019 Quokka | 22.7 | 682 | 40.8 | 81.8 |
| PERC+ 2022 Quokka | 23.8 | 697 | 41.3 | 82.5 |
| PERC+POLO 2022 Quokka | 24.1 | 712 | 40.9 | 82.8 |

**Table 3. *I–V* parameters for an industrial PERC+ cell processed at ISFH in 2019 compared with those for the various simulated scenarios using the input parameters from Tables 1 and 2.**

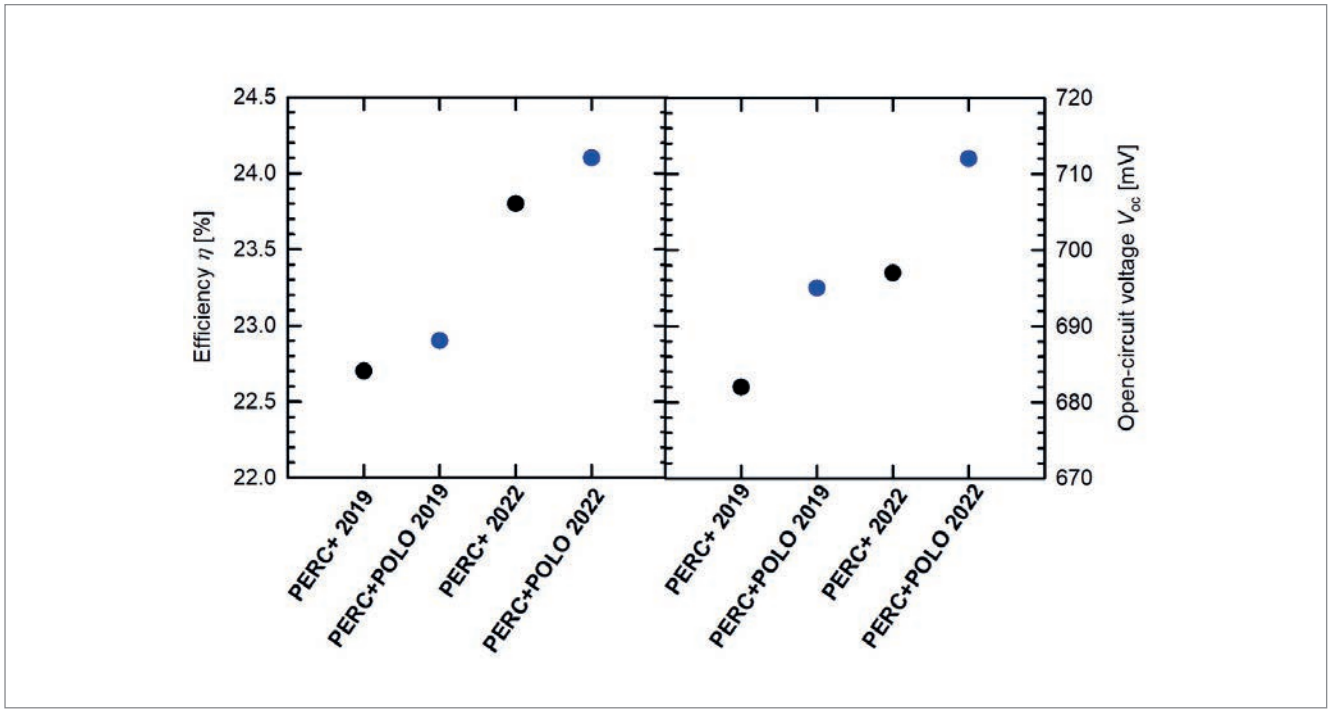


**Figure 4. Simulated conversion efficiencies of PERC+ and PERC+POLO solar cells from using the Quokka software and typical PERC+ and POLO input parameters as measured in 2019 and as expected in 2022 (see Tables 1 and 2). The application of POLO contacts increases the efficiency $\eta$ by up to 0.3%$_{abs}$, towards 24.1%, and $V_{oc}$ by up to 15mV, towards 712mV.**

Table 3 lists the simulated current–voltage (*I–V*) parameters of the 'PERC+ 2019' scenario with a conversion efficiency $\eta$ = 22.7%, which is in good agreement with both the industry status and the PERC+ cell in Table 3 processed at ISFH with $\eta$ = 22.3% efficiency measured in-house. As shown in Fig. 4, the 'PERC+POLO 2019' simulation demonstrates 0.2%$_{abs}$ higher efficiencies and yields 22.9%. As a result of the Ag contact recombination being practically eliminated, the $V_{oc}$ increases from 682mV for PERC+ to 695mV for PERC+POLO.

In a second set of simulations, it is assumed that within the next three years the PERC+ $J_o$ and $f$ parameters will be further improved, as indicated in the '2022 PERC+' column of Table 1; accordingly, the simulated 'PERC+ 2022' efficiency increases to 23.8% and the $V_{oc}$ to 697mV. For the 'PERC+POLO 2022' scenario, the $J_o$ and $f$ parameters given in the '2022 PERC+POLO' column in Table 1 are assumed; these quantities are identical to those for 'PERC+ in 2022', except for the much lower $J_{o,Ag}$ value of the POLO contact.

In addition, it is assumed that it will be possible to reduce the poly-Si finger width to 70µm as a result of improved alignment between poly-Si structuring and Ag screen printing; accordingly, the 'PERC+POLO 2022' simulation achieves the highest conversion efficiency of 24.1% and the highest $V_{oc}$ of 712mV. Again, this high simulated $V_{oc}$ is supported by ISFH's experimentally highest PERC+ implied open-circuit voltage i$V_{oc}$ of 712mV [25]. However, as shown in Table 3, the $J_{sc}$ of the simulated PERC+POLO 2022 cell is 0.4mA/cm² lower than that of the PERC+ 2022 cell because of absorption in the 70µm poly-Si fingers.

## Conclusion

In the past decade, almost all contributions to saturation current density $J_o$ in industrial silicon solar cells have been steadily reduced through the use of new process technologies, such as the PERC concept with $AlO_x/SiN_y$ rear passivation and LCOs, improved emitter doping profiles by in situ and ex situ oxidation, continuous improvements to Ag pastes enabling narrower Ag finger widths, and so on. The reduction in $J_o$ from around 578fA/cm² in 2010 to around 100–150fA/cm² today was a key contribution to increasing the conversion efficiency of 17.5% of Al-BSF cells in 2010 towards 22.5% of today's mass-produced PERC and PERC+ solar cells.

A $J_o$ analysis of current industrial PERC+ solar cells reveals all the individual $J_o$ contributions. Assuming realistic evolutionary improvements, such as further reduced emitter and wafer bulk $J_o$ values, a near-term efficiency potential of up to 23.8% for industrial PERC+ solar cells was simulated. Carrier recombination at the Ag front contact is the biggest contribution to the total $J_{o,total}$ value, thus limiting the $V_{oc}$ to below 700mV. Hence, the PERC+POLO cell concept was simulated, which utilizes poly-Si fingers below the Ag contact, thereby potentially minimizing the area-weighted $J_{o,Ag}$ contribution to below 1fA/cm². Quokka simulations confirm that PERC+POLO cells yield 15mV higher $V_{oc}$ values, of up to 712mV, and 0.3%$_{abs}$ higher conversion efficiencies, of up to 24.1%, compared with PERC+ solar cells. These simulations are supported experimentally by a measured implied open-circuit voltage i$V_{oc}$ = 712mV of PERC+ cell precursors processed at ISFH without metal contacts, as well as by the 24.1%-efficient R&D-type PERC+POLO solar cell published by LONGi.

Because of the relatively small efficiency gain of PERC+POLO over PERC+, in order to be cost effective a very lean manufacturing process flow is proposed for PERC+POLO in which there is only one additional process step compared with PERC+, namely the local deposition of poly-Si fingers by PECVD through a shadow mask. In preliminary experimental tests, the narrowest poly-Si finger widths of 70µm were demonstrated, more details of which can be found in Dullweber et al. [3].

### Acknowledgements

The authors gratefully acknowledge the support of the German Federal Ministry for Economic Affairs and Energy under the contracts 0324294C and 0324246B.

### References

[1] Dullweber, T. et al. 2016, "PERC+: Industrial PERC solar cells with rear Al grid enabling bifaciality and reduced Al paste consumption", *Prog. Photovolt: Res. Appl.,* Vol. 24, pp. 1487–1498.

[2] Stenzel, F. et al. 2019, "Exceeding 23% and mass production of p-Cz Quantum bifacial solar cells", *Proc. 36th EU PVSEC*, Marseille, France, pp. 96–99.

[3] Dullweber, T. et al. 2020, "Evolutionary PERC+ solar cell efficiency projection towards 24% evaluating shadow-mask-deposited poly-Si fingers below the Ag front contact as next improvement step", *Sol. Energy Mater. Sol. Cells,* Vol. 212, 110586.

[4] Min, B. et al. 2017, "A roadmap toward 24% efficient PERC solar cells in industrial mass production", *IEEE J. Photovolt.*, Vol. 7, pp. 1541–1550.

[5] Eisele, S.J. et al. 2009, "18.9% efficient full area laser doped silicon solar cell", *Appl. Phys. Lett.,* Vol. 95, 133501.

[6] Lohmüller, S. et al. 2017, "Key aspects for fabrication of p-type Cz-Si PERC solar cells exceeding 22% conversion efficiency", *Proc. 33rd EU PVSEC,* Amsterdam, The Netherlands, pp. 406–412.

[7] Brendel, R. et al. 2013, "Recent progress and options for future crystalline silicon solar cells", *Proc. 28th EU PVSEC*, Paris, France, pp. 676–690.

[8] Richter, A. et al. 2017, "N-type Si solar cells with passivating electron contact: Identifying sources for efficiency limitations by wafer thickness and resistivity variation", *Sol. Energy Mater. Sol. Cells,* Vol. 173, pp. 96–105.

[9] Stodolny, M.K. et al. 2016, "N-type polysilicon passivating contact for industrial bifacial n-type solar cells", *Sol. Energy Mater. Sol. Cells,* Vol. 158, pp. 24–28.
[10] Feldmann, F. et al. 2019, "Large area TOPCon cells realized by a PECVD tube process", *Proc. 36th EU PVSEC*, Marseille, France, pp. 304–308.
[11] Nandakumar, N. et al. 2019, "Approaching 23% with large area monoPoly cells using screen printed and fired rear passivating contacts fabricated by inline PECVD", *Prog. Photovolt: Res. Appl.,* Vol. 27, pp. 107–112.
[12] Deng, W. et al. 2019, "The influence of diffusion condition to passivation quality of SiOx/poly-silicon layer", *Proc. 36th EU PVSEC*, Marseille, France, pp. 259–261.
[13] Jin, H. 2018, Presentation at 12th SNEC Int. PV Power Gen. Conf., Shanghai, China.
[14] Fan, J. et al. 2019, "The roadmap to > 24% of PERC", *Proc. 29th Internat. PVSEC*, Xi'an, China, pp. 1444–1446.
[15] ITRPV 2019, "International technology roadmap for photovoltaic (ITRPV): Results 2018", 10th edn (Mar.) [https://itrpv.vdma.org/en/].
[16] Dullweber, T. 2020, "High efficiency industrial PERC solar cells for monofacial and bifacial applications", in *High-Efficient Low-Cost Photovoltaics,* Petrova-Koch, V., Hezel, R. & Goetzberger, A., Eds. Springer Nature Switzerland AG, pp. 65 – 94.
[17] Dullweber, T. et al. 2012, "Towards 20% efficient large-area screen-printed rear-passivated silicon solar cells", *Prog. Photovolt: Res. Appl.,* Vol. 20, pp. 630–638.
[18] Kranz, C. et al. 2016, "Void formation in screen-printed local aluminum contacts modeled by surface energy minimization", *Sol. Energy Mat. Sol. Cells,* Vol. 158, pp. 11–18.
[19] Peng, Z.W. et al. 2019, "Industrial screen-printed n-PERT-RJ solar cells: Efficiencies beyond 22% and open-circuit voltages approaching 700 mV", *IEEE J. Photovolt.,* Vol. 9, pp. 1166–1174.
[20] Tsuji, K. et al. 2019, "Fine line Al printing on narrow point contact opening for front side metallization", *AIP Conf. Proc.*, Vol. 2147, 040019.
[21] Kranz, C. et al. 2012, "Impact of the rear surface roughness on industrial-type PERC solar cells", *Proc. 27th EU PVSEC*, Frankfurt, Germany, pp. 557–560.
[22] Hahn, G. 2010, "Status of selective emitter technology", *Proc. 25th EU PVSEC*, Valencia, Spain, pp. 1091–1096.
[23] Dullweber, T. et al. 2013, "Ion-implanted PERC solar cells with $Al_2O_3/SiN_x$ rear passivation", *Energy Procedia,* Vol. 38, pp. 430–435.
[24] Deng, W. et al. 2017, "22.61 % efficient fully

screen printed PERC solar cell", *Proc. 44th IEEE PVSC*, Washington DC, USA, pp. 2220–2226.
[25] Jäger, P., Baumann, U. & Dullweber, T. 2019, "Impact of the thermal budget of the emitter formation on the pFF of PERC+ solar cells", *AIP Conf. Proc.,* Vol. 2147, 140005.
[26] Kimmerle, A. et al. 2013, "Simplified front surface field formation for back contacted silicon solar cells", *Energy Procedia,* Vol. 38, pp. 278–282.
[27] Piechulla, A. et al. 2015, "Low pressure diffusions for high quality emitter formation in advanced p- and n-type solar cells", *Proc. 31st EU PVSEC,* Hamburg, Germany, pp. 420–424.
[28] Dullweber, T. et al. 2017, "Emitter saturation current densities of 22 fA/cm$^2$ applied to industrial PERC solar cells approaching 22% conversion efficiency", *Prog. Photovolt: Res. Appl.,* Vol. 25, pp. 509–514.
[29] Cuevas, A. et al. 1996, "Surface recombination velocity of highly doped n-type silicon", *J. Appl. Phys.,* Vol. 80, pp. 3370–3375.
[30] Lorenz, A. et al. 2018, "Screen printed thick film metallization of silicon solar cells – Recent developments and future perspectives", *Proc. 35th EU PVSEC*, Brussels, Belgium, pp. 819–824.
[31] Braun, S. et al. 2013, "The multi-busbar design: An overview", *Energy Procedia,* Vol. 43, pp. 86–92.
[32] Hannebauer, H. et al. 2012, "Analysis of the emitter saturation current density of industrial type silver screen-printed front contacts", *Proc. 27th EU PVSEC,* Frankfurt, Germany, pp. 1360–1363.
[33] Ye, F. et al. 2016, "22.13% efficient industrial p-type mono PERC solar cell", *Proc. 43rd IEEE PVSC,* Portland, Oregon, USA, pp. 3360–3365.
[34] Shanmugam, V. et al. 2016, "Impact of the phosphorus emitter doping profile on metal contact recombination of silicon wafer solar cells", *Sol. Energy Mater. Sol. Cells,* Vol. 147, pp. 171–176.
[35] Padhamnath, P. et al. 2019, "Metal contact recombination in monoPoly™ solar cells with screen-printed & fire-through contacts", *Sol. Energy Mater. Sol. Cells*, Vol. 192, pp. 109–116.
[36] Dullweber, T. et al. 2013, "Silicon wafer material options for highly efficient p-type PERC solar cells", *Proc. 39th IEEE PVSC,* Tampa, Florida, USA, pp. 3074–3078.
[37] Lim, B. 2018, "LID-free PERC+ cells with stable efficiencies up to 22.1%", *Proc. 35th EU PVSEC,* Brussels, Belgium, pp. 359–365.
[38] Dullweber, T. & Schmidt, J. 2016, "Industrial silicon solar cells applying the Passivated Emitter and Rear Cell (PERC) concept—A review", *IEEE J. Photovolt.,* Vol. 6, pp. 1366–1381.
[39] Dullweber, T. et al. 2018, "Present status and future perspectives of bifacial PERC+ solar cells and modules", *Jpn. J. Appl. Phys.,* Vol. 57, 08RA01.
[40] Brendel, R. 2012, "Modeling solar cells with the dopant-diffused layers treated as conductive boundaries", *Prog. Photovolt: Res. Appl.,* Vol. 20, pp. 31–43.
[41] Fell, A. 2013, "A free and fast three-dimensional/two-dimensional solar cell simulator featuring conductive boundary and quasi-neutrality approximations", *IEEE Trans. Electron Dev.,* Vol. 60, pp. 733–738.
[42] Reiter, S. et al. 2016, "Parasitic absorption in polycrystalline Si-layers for carrier-selective front junctions", *Energy Procedia*, Vol. 92, pp. 199–204.
[43] Min, B. et al. 2018, "Increasing the photo-generated current in solar cells with passivating contacts by reducing the poly-Si deposition temperature", *AIP Conf. Proc.*, Vol. 1999, 040015.

## About the Authors

Dr. Thorsten Dullweber leads the industrial solar cells R&D group at ISFH. His research work focuses on high-efficiency industrial-type PERC and PERC+ silicon solar cells and ultrafine-line screen-printed Ag front contacts. Before joining ISFH in 2009, he spent nine years as a project leader in the microelectronics industry at Siemens AG and later worked for Infineon Technologies AG.

Dr. Robby Peibst obtained his diploma degree in technical physics in 2005. In 2010 he received his Ph.D. from the Leibniz University of Hanover, with a thesis on germanium-nanocrystal-based memory devices. He joined ISFH in 2010 and has led the emerging solar technologies group since 2013. His research focuses on the development of techniques for enabling the production of high-efficiency silicon solar cells.

Rolf Brendel is the scientific director of ISFH. He received his Ph.D. in materials science from the University of Erlangen, for which he researched infrared spectroscopy. In 2004 he joined the Institute of Solid State Physics of the Leibniz University of Hanover as a full professor. His main research focuses on the physics and technology of crystalline silicon solar cells.

## Enquiries

Institute for Solar Energy Research Hamelin (ISFH)
Am Ohrberg 1
31860 Emmerthal
Germany

Email: dullweber@isfh.de
Tel: +49-5151-999-642

# Towards 24% efficiency for industrial n-type bifacial passivating-contact solar cells with homogeneous emitter

Jie Bao, Cheng Chen, Ronglin Liu, Zhencong Qiao, Zheren Du, Zhifeng Liu & Jia Chen, Jolywood Solar Technology Co. Ltd., Taizhou City, Jiangsu Province, China

## Abstract

Passivating-contact solar cells are attracting more and more attention in the solar industry because of their high efficiency potential and high compatibility with existing passivated emitter and rear cell (PERC) and passivated emitter rear totally diffused (PERT) process flows. Jolywood was one of the first few manufacturers producing solar cells and modules featuring passivating-contact technology, with a capacity exceeding 2GW. This work reports the latest results obtained at Jolywood for full-area (251.99cm²) n-type bifacial passivating-contact solar cells using a cost-effective process with industrially-feasible boron diffusion, phosphorus ion implantation and low-pressure chemical vapour deposition (LPCVD) with in situ oxidation. The impact of a P-tail profile and a boron emitter profile on the recombination current in the non-metallized and metallized areas and the corresponding contact resistivity is systematically investigated. To the best of the authors' knowledge, a current density $J_{o,metal}$ of 666fA/cm² is the lowest value reported for a homogeneous boron emitter with a $J_{o,pass}$ of 25fA/cm². This result is an important one in order for industrial passivating-contact solar cells to be cost effective. With optimized processes, an average efficiency of up to 23.85% with an excellent open-circuit voltage $V_{oc}$ of 703.5mV are obtained in the production line. A power loss analysis performed via Quokka3 indicates that the performance is mainly limited by the optical loss and emitter recombination. Inspired by these results, with further process optimization a record efficiency of 24.21% in R&D is achieved, featuring a $V_{oc}$ of 711.6mV. The performance of the passivating-contact solar cells and corresponding modules is found to be stable, and sometimes even improved, under heat and light treatment, such as in standard light-induced degradation (LID) and light and elevated temperature-induced degradation (LeTID) test conditions.

## Introduction

The polysilicon passivating contact has received a lot of attention from many research institutes and industries because of its excellent surface passivation and compatibility with industry-standard processes. Passivating-contact solar cells with a selective p⁺ emitter yielding 25.8% efficiency, and with an interdigitated back contact (IBC) structure yielding 26.1% efficiency, have been demonstrated by Fraunhofer ISE [1] and ISFH [2], respectively.

Inspired by those research achievements, various manufacturers, such as Jolywood, Trina Solar and GCL, have spared no effort in commercializing the passivating-contact solar cell by transferring the technology from the lab to mass production; record efficiencies of 23.85% [3], 24.79 [4], 24.58% [5] and 23.04% [6] on a full-size scale have been reported. However, achieving both low contact recombination and low contact resistivity for n⁺ poly-Si passivation is still a subject of ongoing research in industry with fire-through Ag paste.

"Achieving both low contact recombination and low contact resistivity for n⁺ poly-Si passivation is still a subject of ongoing research in industry with fire-through Ag paste."

As an n-type solar cell and module manufacturer, Jolywood focuses on the development of n-type bifacial passivating-contact solar cells, combining findings from previous developments [7,8]. An average efficiency of 23.85% and a record efficiency of 24.21% with an open-circuit voltage $V_{oc}$ of 711.6mV have been achieved at the cell level by optimizing the doping profile of n⁺ poly-Si and p⁺ emitter. These results may provide some new guidance for cell efficiency improvements in mass production. The reliability of cells and modules is further investigated by performing light-induced degradation (LID), harsher (>3 times) LID, and light and elevated temperature-induced degradation (LeTID) tests. The results show that no degradation occurs in the cells and modules.

This paper is an extended version of a recent publication for the 37th EU PVSEC in 2020 [9].

## Passivating-contact solar cell technology

Fig. 1(a) and (c) show the schematic diagram and process flow of passivating-contact solar cells processed on full-area (251.99cm²) n-type Cz substrates with a resistivity of ~1Ω·cm. The cells feature a homogeneous boron emitter with $BBr_3$ diffusion and tunnel-$SiO_x$/n⁺ poly-Si structure, doped ex situ by industrial phosphorus ion implantation. The tunnel-$SiO_x$ is grown in situ by thermal oxidation in a low-pressure chemical vapour deposition (LPCVD) furnace and capped by intrinsic poly-Si (i-poly) of thickness greater than 100nm. The cells are screen printed with 12 busbars on both sides, as shown in Fig. 1(b).

The impacts of a phosphorus in-diffusion (P-tail) profile and a boron emitter profile on passivated current density ($J_{o,pass}$), metal recombination current density ($J_{o,metal}$) and corresponding contact resistivity ($\rho_c$) are systematically investigated. All of these are closely related to the performance of

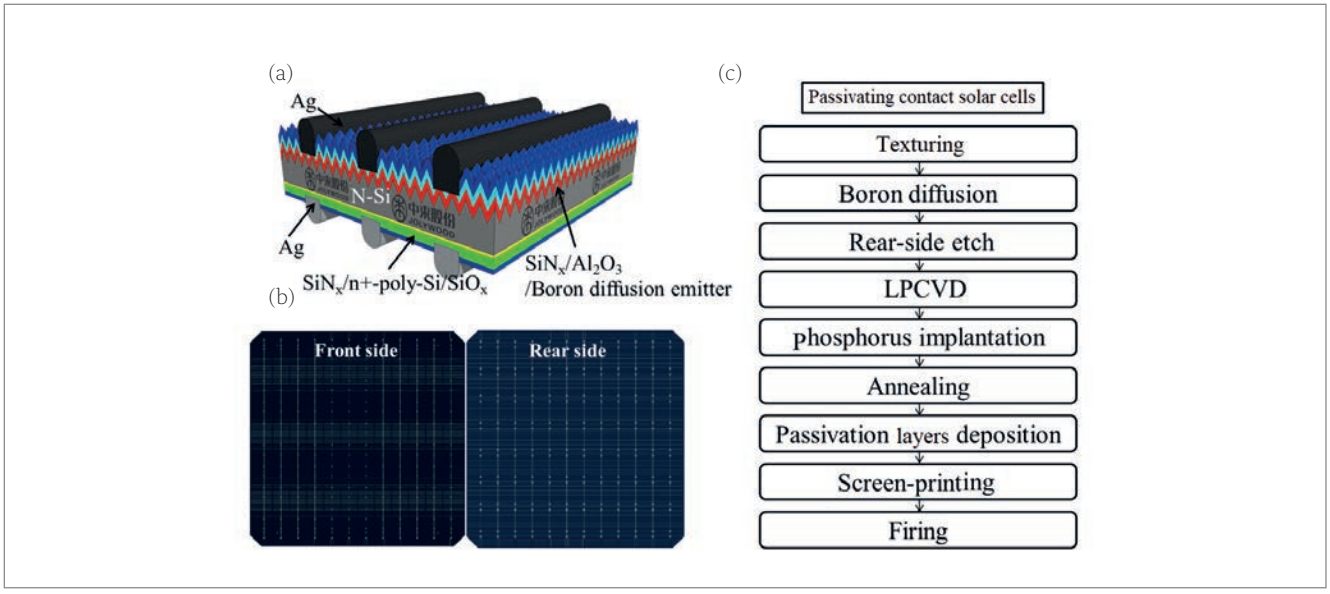


**Figure 1. (a) Schematic diagram of the structure of an n-type bifacial passivating-contact solar cell. (b) Photographs of the front and rear sides of a bifacial passivating-contact solar cell fabricated at Jolywood. (c) Process sequence of a passivating-contact solar cell, used in industrial mass production.**

the solar cell. The results will provide some new guidance for cell efficiency improvement in mass production and R&D.

## Rear passivating-contact optimization

The rear-side $SiO_x/n^+$ poly-Si layers are screen printed with fire-through (FT) Ag paste. It has been reported that the FT paste could locally spike through the $SiO_x/n^+$ poly-Si and make contact directly with the c-Si bulk during firing, resulting in very high recombination and resistive losses [10,11]. To strike a balance between passivation and contact quality, the impact of the 'P-tail' (formed by phosphorus atoms diffusing from the $n^+$ poly-Si into the n-Si substrate) on surface passivation and contact properties is systematically investigated.

As illustrated in the electrochemical capacitance–voltage (ECV) profiles in Fig. 2(a), passivating-contacts with various P-tails, marked N1–N4, are obtained by gradually increasing the annealing temperature ($T_{anneal}$). To avoid parasitic current flowing through several conductive layers, the $n^+$ poly-Si layer and P-tail in the non-contacted regions are etched before the $\rho_c$ measurement via the transmission line method (TLM) [12] or the Cox-Strack method [13]. However, selective removal of the $n^+$ poly-Si layer and the P-tail is too complicated and not cost effective for industrial implementation.

To solve this problem, an improved TLM structure (see inset in Fig. 2(b)) developed by Jolywood is utilized to measure the contact resistivity of $Ag/n^+$ poly-$Si/SiO_x$/c-Si, which features a tunnel-$SiO_x/n^+$ poly-Si layer around each finger and which is isolated by creating grooves with a depth of more than 1.5μm in order to eliminate unwanted current paths during TLM measurements. The measured value is a 'lumped' value comprising the contact resistivity of $Ag/n^+$ poly-Si, the tunnel resistivity of $n^+$ poly-$Si/SiO_x$/c-Si, and the contact resistivity of the Ag/P-tail. The $\rho_c$ values obtained via the improved TLM structure for N1–N4 are summarized in Fig. 2(b).

Fig. 2(a) reveals an initially flat distribution of P dopants in the $n^+$ poly-Si layer, which then drops sharply from the poly-$Si/SiO_x$ interface (indicated by the dashed grey line) to c-Si; the P-tail within the c-Si becomes deeper as a result of more P

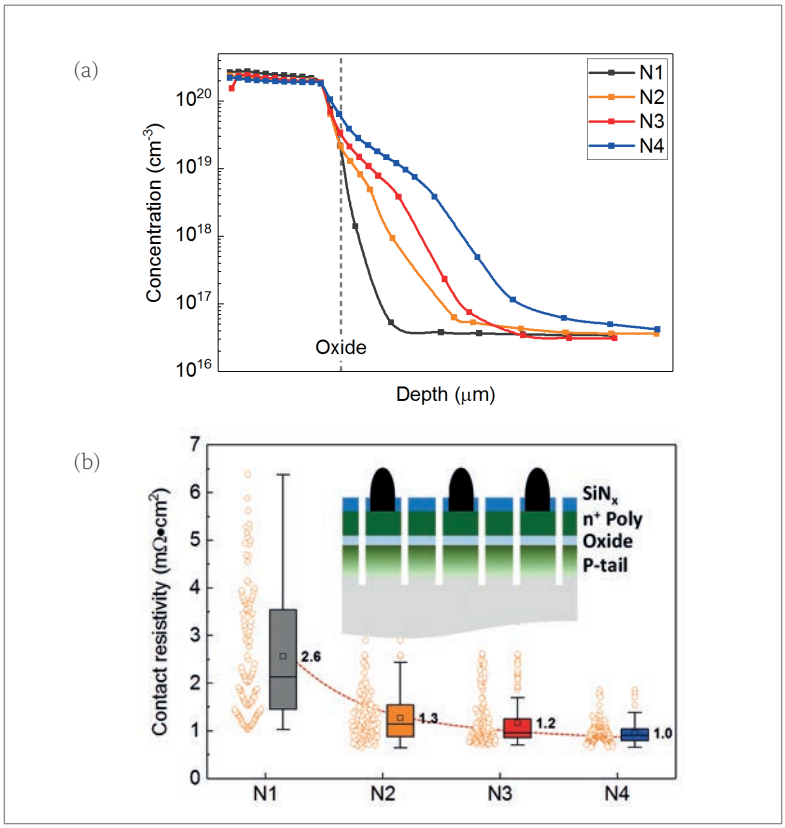


**Figure 2. (a) ECV profiles for phosphorus in the tunnel-$SiO_x/n^+$ poly-Si structure annealed at various temperatures. (b) The corresponding contact resistivities, measured by the improved TLM structure. Inset: schematic of the improved TLM structure for the $\rho_c$ measurement of $Ag/n^+$ poly-$Si/SiO_x$/c-Si. The dashed/dotted lines in the figure are visual guides.**

atoms diffusing from the poly-Si into the bulk at increasing temperatures $T_{anneal}$. The sample N1, with a very shallow P-tail in the Si bulk, exhibits high-quality passivation (~6fA/cm²) but poor contact performance. The upper-limit $\rho_c$ could be around 6.5mΩ·cm².

The rear surface used in this work, formed by acid-based single-side etching, is much rougher than an alkaline polished rear surface; thus, $J_o$ is slightly higher than for an alkaline polished surface. A moderately leaky profile, such as that exhibited by N2, with slightly more in-diffusion, helps reduce $\rho_c$ and maintain $J_{o,pass}$ (7fA/cm²). However, as $T_{anneal}$ continues to increase, more dopants migrate into the c-Si bulk. Although $\rho_c$ drops further to ~1.0mΩ·cm², the value of $J_{o,pass}$ increases significantly from 14fA/cm² to 21fA/cm² (see N3 and N4 in Fig. 3).

The value of $J_{o,metal}$ is extracted by fitting $J_{o,metal}$ vs. metalization fraction, which is measured from Ag-etched lifetime samples [14]. As shown in Fig. 3, $J_{o,metal}$ drops initially with increasing $T_{anneal}$ and gradually saturates at a similar level to that of N2. Unlike the results of Stodolny et al. [13] from ECN, $J_{o,metal}$ of the passivating contact decreases linearly with increasing in-diffusion depth. These results indicate that, in order to balance the surface recombination and contact properties, a moderate doping tail (~0.15μm) within the c-Si bulk is sufficient to avoid the high recombination and contact resistance caused by metal spikes. With the optimization, excellent passivation characteristics of a $SiO_x/n^+$ poly-Si structure, with $J_{o,pass}$ ~7fA/cm², $J_{o,metal}$ ~247fA/cm² and low $\rho_c$ ~ 1.3mΩ·cm², are obtained simultaneously on a planar surface.

### Front p⁺ emitter optimization

In order to find a suitable p⁺ emitter, four diffusion profiles, represented by B1–B4 with different peak concentrations ($C_{peak}$) and junction depths, were developed by varying the diffusion process. The doping profiles measured by ECV are depicted in Fig. 4(a); the sheet resistances of the B1–B4 profiles measured by a four-point probe (4pp) are 85, 95, 70 and 50Ω/sq., respectively. Profiles B1 and B4 initially show very similar values for $C_{peak}$, and likewise B2 and B3, until the junction depths for profiles B1–B4 gradually increase.

As shown in Figs. 4 and 5, the B1 profile, with a high $C_{peak}$ and shallow junction, exhibits low non-metallized recombination ($J_{o,pass}$ ~27fA/cm²) but poor contact properties ($J_{o,metal}$ ~1,025fA/cm² and $\rho_c$~2.8mΩ·cm²). The latter is attributed to the Ag-Al paste spiking too much into the p⁺ emitter (perhaps close to the p-n junction) and forming a centre of high recombination during metallization.

A high $C_{peak}$ and a deep junction profile, such as that of B4, could provide a better shielding of the high recombination at the metal contacts ($J_{o,metal}$ ~541fA/cm²) and enable low contact resistivity ($\rho_c$ ~0.9mΩ·cm²), while $J_{o,pass}$ is dramatically increased. A lightly doped $C_{peak}$ and a deep junction

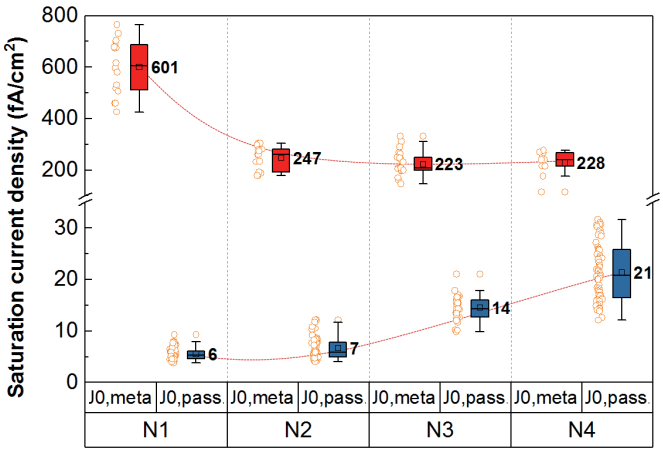


**Figure 3. The corresponding non-metallized and metallized passivation properties for a passivating contact with different annealing temperatures. The dashed/dotted lines in the figure are visual guides.**

"To balance the surface recombination and contact properties, a moderate doping tail within the c-Si bulk is sufficient to avoid the high recombination and contact resistance caused by metal spikes."

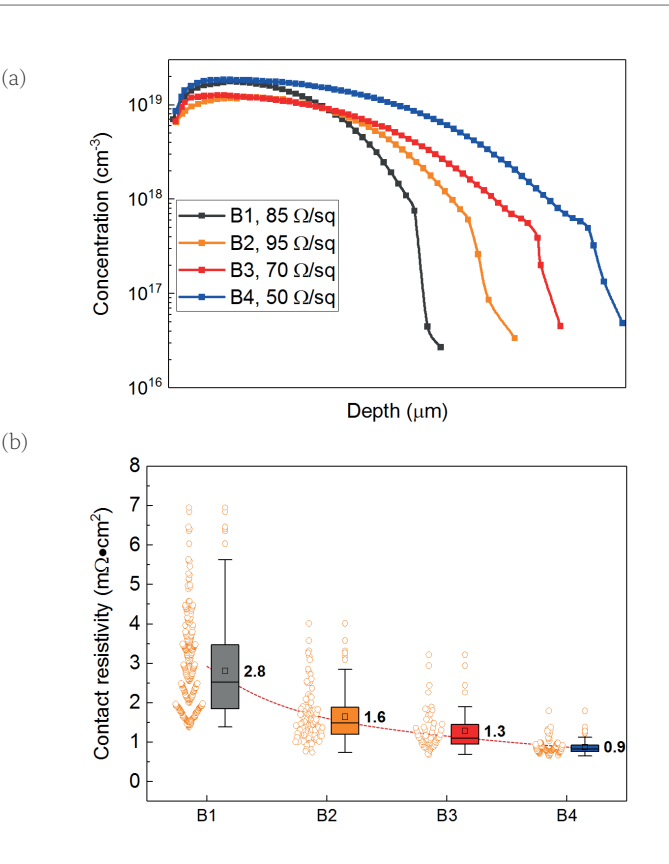


**Figure 4. (a) Boron-doping profiles of the p⁺ emitter with various diffusion processes. (b) The corresponding contact resistivities are measured using the standard TLM structure. The dotted line in the figure is a visual guide.**

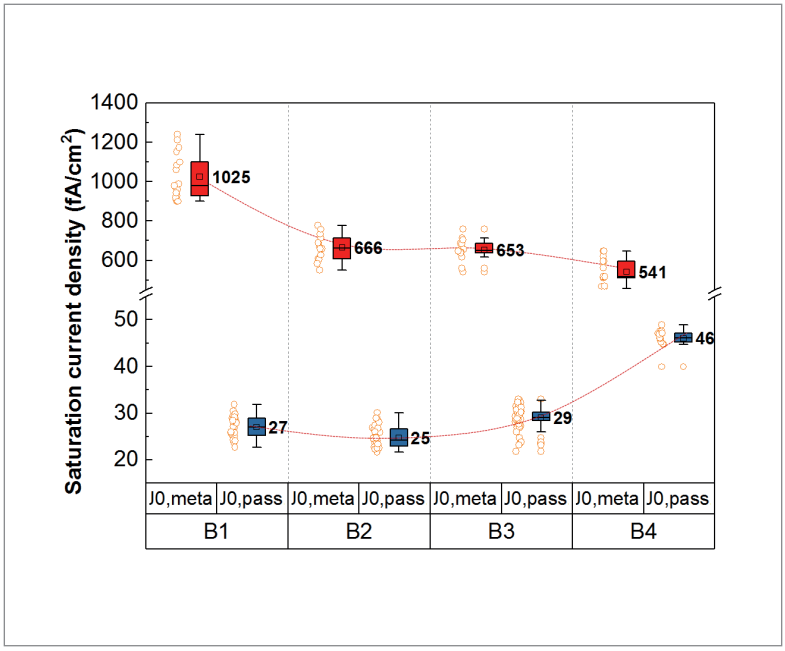


**Figure 5. Corresponding passivated and metallized passivation properties for the p⁺ emitter with the doping profiles. Dashed/dotted lines in the figure are visual guides.**

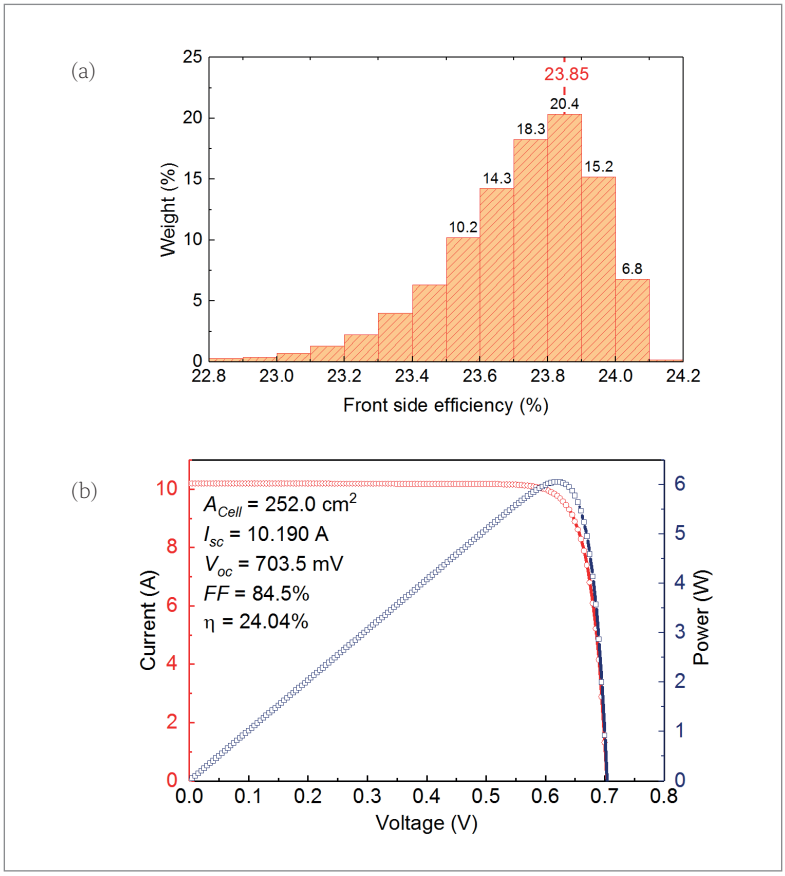


**Figure 6. (a) Front-side efficiency distribution for a batch of over 20,000 cells fabricated on the production line. (b) Third-party calibrated *I–V* curves of the calibrated cell. These figures have been reproduced using the raw data.**

> "The values of $J_{o,metal}$ and $\rho_c$ of the p⁺ emitter are more related to junction depth than to peak concentration."

depth, for example demonstrated in the B2 and B3 profiles, enables both a low $J_{o,pass}$ and a low $J_{o,metal}$.

The studies carried out indicate that the values of $J_{o,metal}$ and $\rho_c$ of the p⁺ emitter are more related to junction depth than to peak concentration. A homogeneous p⁺ emitter with a low $C_{peak}$ and a deep junction depth is preferable in order to balance the $J_{o,pass}$, $J_{o,metal}$ and $\rho_c$. Compared with the B3 profile, the B2 profile shows the merits of reduced Auger recombination loss, free-carrier absorption (FCA) and lower diffusion temperature, and is therefore used in Jolywood's passivating-contact solar cells.

## Mass-produced passivating-contact cells

The distribution of the front-side efficiency for a batch of 20,000 solar cells in a single production line is shown in Fig. 6, which features a very narrow efficiency distribution and thus good process stability. The average efficiency in mass production is 23.85%. The record cell in Jolywood's production line was independently measured by a third party to have a front-side efficiency of 24.04% and a $V_{oc}$ of 703.5mV; detailed parameters are summarized in Table 1.

## Power loss of the passivating-contact cell

To identify options for further improvement of cell performance, a power loss analysis of the record solar cell is performed by applying the FELA [15] approach implemented in Quokka3. As shown in Fig. 7, with the help of a passivating contact the recombination and resistive losses for the $SiO_x$/n⁺ poly-Si are minor. The optical loss, on the other hand, reduces the efficiency by about 2.93%, which is mostly dominated by the imperfect light-trapping loss (1.55%). After the optical loss, the p⁺ emitter is the second largest component (1.13%), among which the passivated recombination of the p⁺ emitter contributes the most (0.59%).

Enlightened by the power loss analysis, further optimization of the optical losses (such as reflection, electrode shading and light-trapping losses) was carried out. Upon incorporating a better optimized p⁺ emitter and rear n⁺ poly-Si/$SiO_x$ into the cells, a record passivating-contact solar cell with 24.21% efficiency and 711.6mV $V_{oc}$ was achieved.

| | $J_{sc}$ [mA/cm²] | $V_{oc}$ [mV] | *FF* [%] | $\eta$ [%] |
|---|---|---|---|---|
| Calibrated* | 40.44 | 703.5 | 84.5 | 24.04 |

*Independently confirmed by the third-party Metrology Institute.

**Table 1. Record efficiency of an n-type passivating-contact solar cell in mass production.**

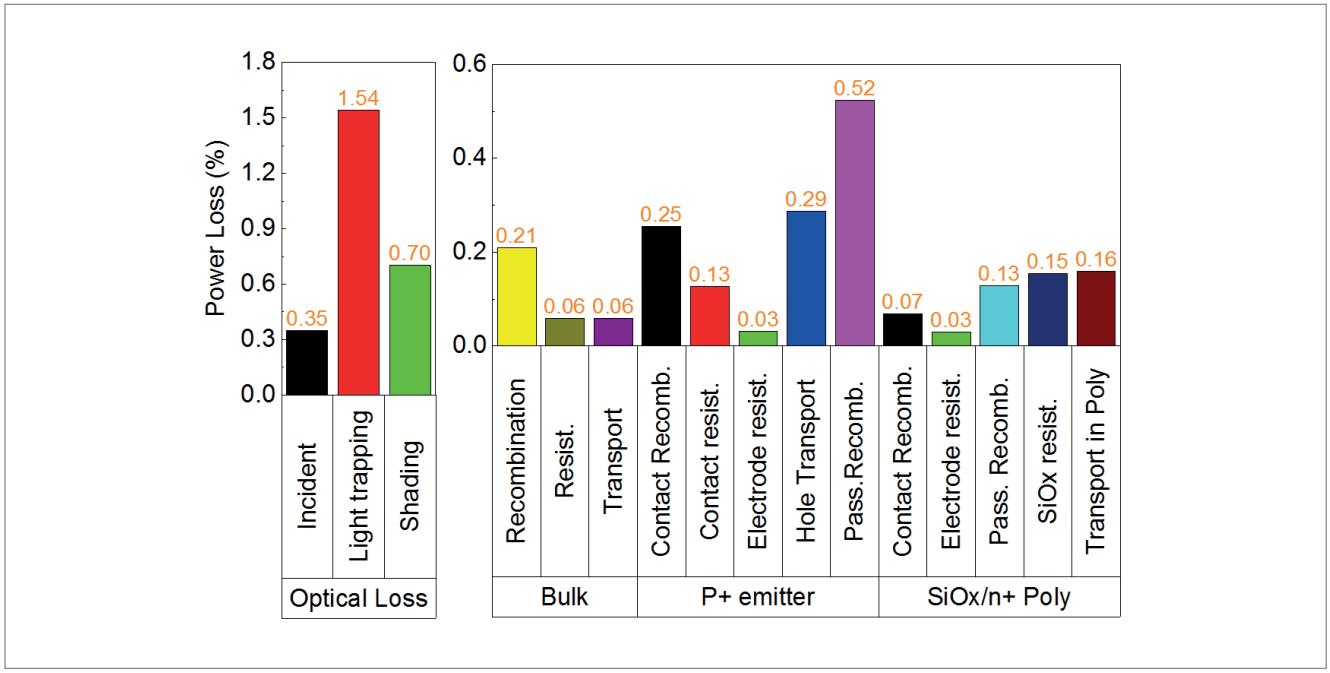


**Figure 7. Detailed power loss analysis for the solar cells in mass production with an average efficiency of 23.85%.**

## Passivating-contact module technology

N-type modules, as shown in Fig. 8, were fabricated with Jolywood's passivating-contact silicon solar cells. A front-side *I–V* measurement was performed under standard test conditions (STC) with the rear side covered by a non-reflective black mask. Average output powers of 415W and 420W were obtained for the n-type bifacial passivating-contact modules with 72 full-size cells and 144 half-cut cells, respectively. The bifacial modules show the merits of a high bifaciality of ~85%, a low degradation coefficient of less than –1.0% for the first year and –0.4% annually thereafter, a low temperature coefficient of –0.32%/K, and a high weak-illumination response.

A full-black module developed by Jolywood utilizing a black backsheet on the rear side is shown in Fig. 8(c). Compared with a double-glass module, the weight can be reduced by ~30% by replacing the rear glass with a black backsheet. The full-black module features excellent aesthetics and light weight, which is perfect for building-integrated PV (BIPV) applications.

## Reliability of passivating-contact cells and modules

### LID test

In the production line, cells are randomly selected to monitor the LID after the *I–V* measurement. The test conditions for LID are five hours light soaking under 1-sun light intensity at 55°C. The relative efficiency variation is defined by $(\eta_{before} - \eta_{after})/\eta_{before}$, where $\eta_{before}$ is the initial efficiency of cells before the LID test, and $\eta_{after}$ is the final efficiency of the cells after the LID test.

The relative efficiency variation results for the whole of 2019 for Jolywood's bifacial passivating-contact solar cells tested under LID conditions are summarized in Fig. 9. The relative efficiency changes are all negative for n-type passivating-contact solar cells, which indicates that rather than degrading the initial efficiency, the LID test treatment is beneficial in terms of improving the efficiency of these types of solar cell.

> "Upon incorporating a better optimized $p^+$ emitter and rear $n^+$ poly-Si/$SiO_x$ into the cells, a record passivating-contact solar cell with 24.21% efficiency and 711.6mV $V_{oc}$ was achieved."

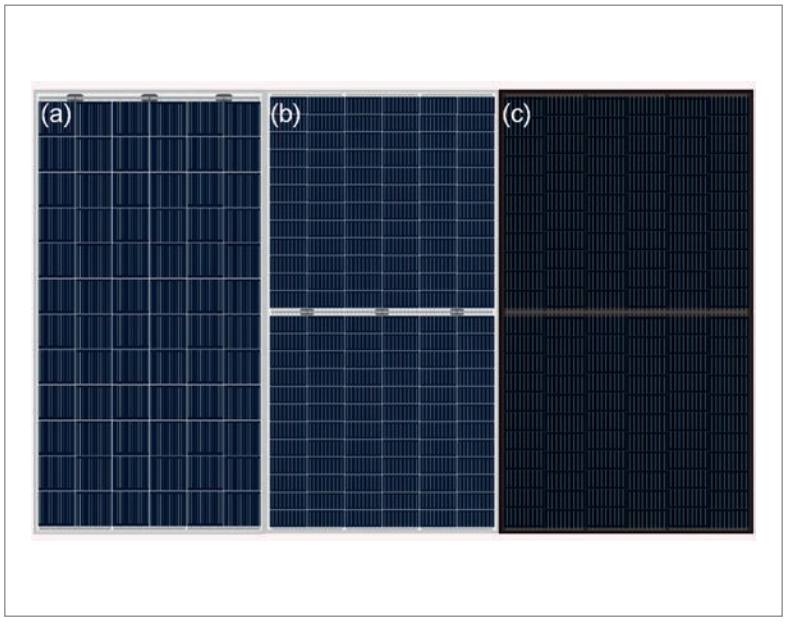


**Figure 8. Images of n-type bifacial passivating-contact module products with (a) 72 full-size cells, and (b) 144 half-cut cells. (c) Full-black monofacial module with 132 half-cut cells.**

# PV CELLTECH CONFERENCE Online 2021

## 27-29 April 2021

Going into its sixth year, **PV CellTech** is a truly unique event attended by the world's top cell manufacturers, equipment and material suppliers, shaping the PV Technology Roadmap of the future

**Join us to network with PV industry leaders.**

> "PVCellTech kept me up-to-date at a time where networking and exchange is more difficult than usual. The speakers are asked not to show generally available graphs (like the ITRPV) and instead are required to show their own achievements and to talk about their own activities. This makes the content very useful and unique."
> **Pietro Altermatt, Princpal Scientist, Trinasolar**

> "This conference is the most information dense annual event in the field of PV cell technology."
> **Akira Terakawa, R&D Project Leader, Panasonic Corporation**

Previous sponsors included:

GOLD

Aiko CELLS made from the heart · Heraeus · JINERGY · 中来光电 JOLYWOOD · Q CELLS Engineered in Germany · MEYER BURGER · risen solar technology · SCHMID Expect Solutions · SINGULUS · VON ARDENNE

SILVER

halm.

SUPPORTING

ISRA VISION GPsolar · PVEL · sgl carbon

To get involved either as a speaker, partner or attendee please email: **marketing@solarmedia.co.uk**

**celltech.solarenergyevents.com**

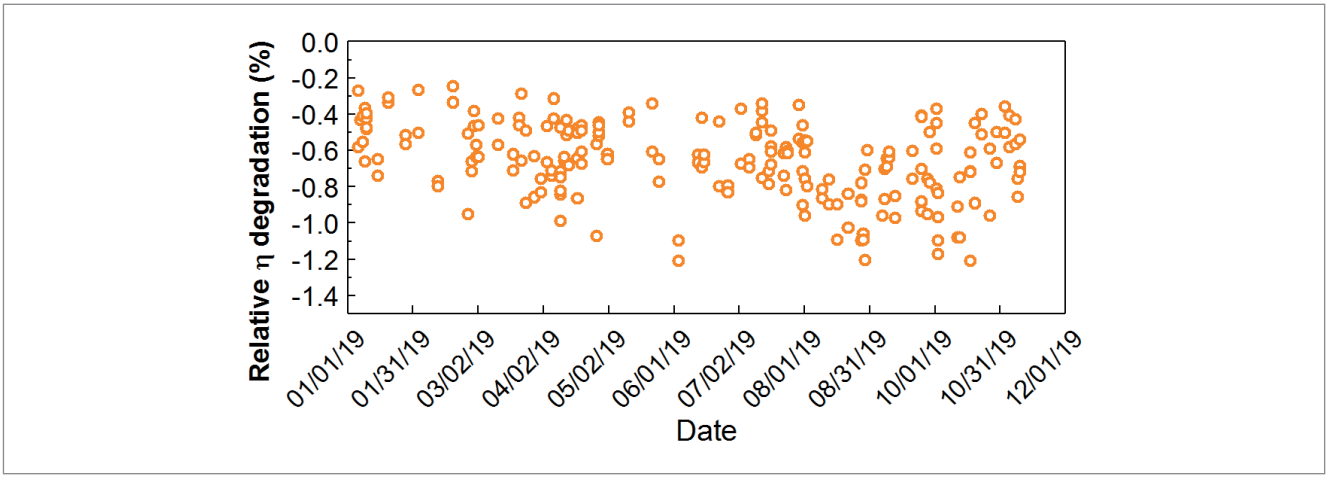


**Figure 9. Light-induced degradation (LID) of n-type passivating-contact solar cells, using an illumination intensity of 1 sun and a cell temperature of 55°C.**

### Harsher LID test

The reliability of n-type passivating-contact solar cells is tested under much harsher conditions, such as higher temperatures (≥220°C) and higher illumination intensities (≥5 suns). This test equates to more than three times more severe than a typical LID test.

Fig. 10 shows the variation in the *J–V* parameters of the cells before and after the harsher LID test. It can be seen that after being processed with the harsher LID test, the efficiency of the cells increased by 0.17%, which is mainly due to the improvement in $V_{oc}$ and *FF*. Consequently, the n-type passivating-contact solar cells exhibit excellent reliability, even under more stringent LID tests.

### LeTID test

LeTID tests are performed on n-type bifacial passivating-contact modules with 72 full-size cells. The modules are treated in the dark chamber at 75°C with 1A current soaking, each LeTID cycle lasting 96 hours. Modules utilizing cells without having undergone the severe LID test show non-degradation after the first cycle of the LeTID test, and minor degradation (<1.0%) after the third cycle. The performance of the modules recovered and showed positive gains after the 4th cycle, as shown in Fig. 11(a). For those modules using solar cells processed with the harsher LID test, no degradation was observed, even after four cycles of the LeTID test, as shown in Fig. 11(b).

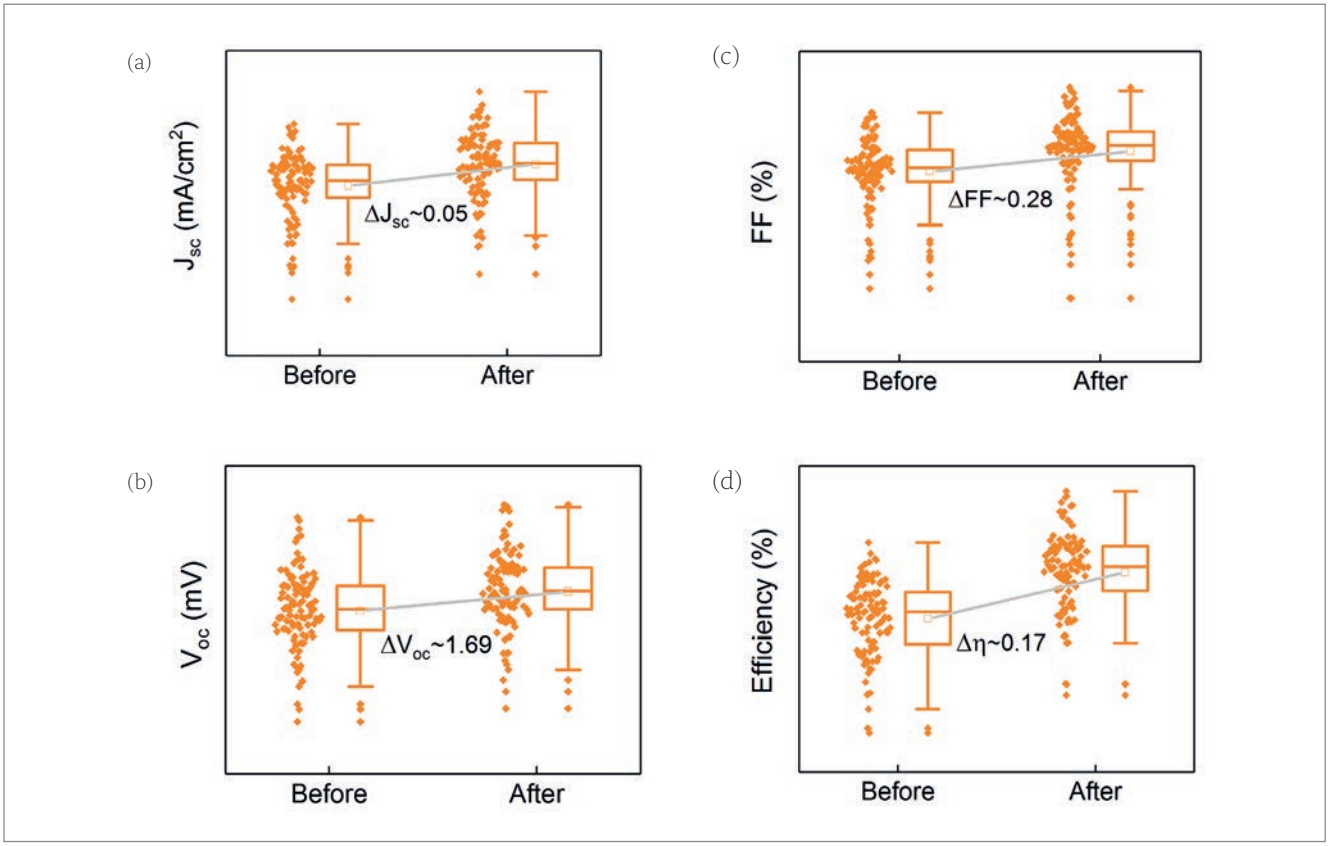


**Figure 10. *J–V* parameters for n-type passivating-contact solar cells before and after the harsher (>3 times) LID tests.**

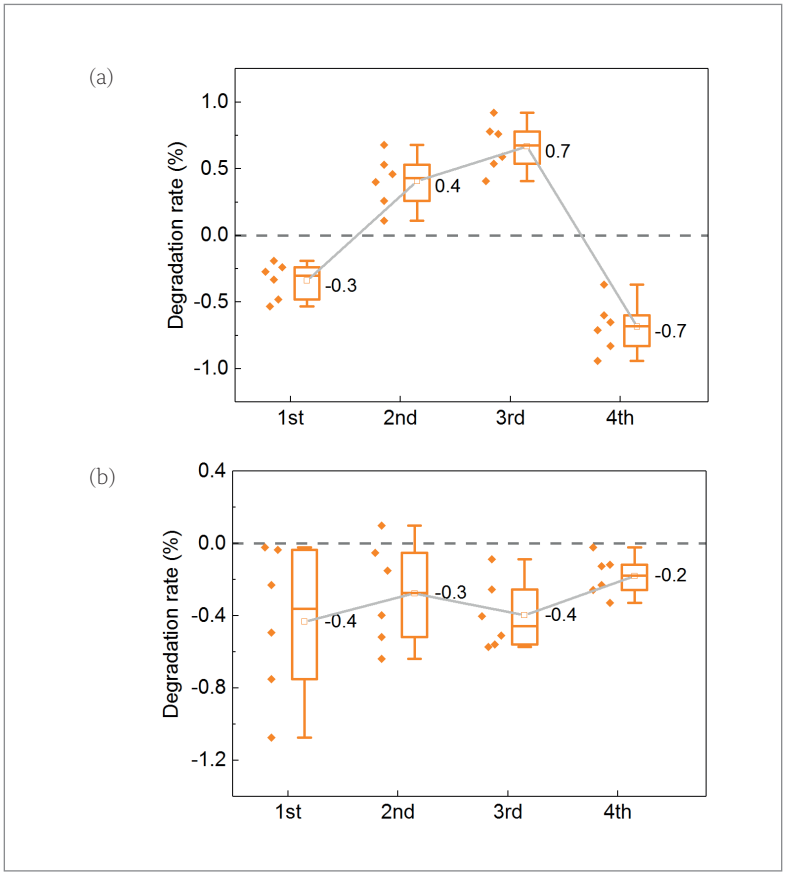


**Figure 11. Four-cycle LeTID test for n-type passivating-contact modules: (a) without and (b) with the harsher (>3 times) LID test. The time duration of one cycle of the LeTID test is 96 hours, with a module temperature of 75°C and a 1A current soaking.**

"The reliability tests showed that n-type bifacial passivating-contact solar cells and modules are free from LID and are minimally impacted by LeTID."

It is interesting to observe that modules treated under severe LID test conditions are more stable throughout these four cycles. It is proposed that excess hydrogen in the bulk silicon after the firing process can form hydrogen-bonded defects during the first cycle of the LeTID test. These defects, however, can be dissociated during long-duration carrier injection and annealing, which accounts for the recovery of modules after the fourth cycle. On the other hand, if the modules have already been subjected to the harsher (>3 times) LID test, the excess hydrogen in the bulk silicon becomes depleted, which keeps the solar cells in the modules free from hydrogen-related degradation in the subsequent LeTID test.

## Summary

This paper has reported the latest results obtained at Jolywood for full-size n-type bifacial passivating-contact solar cells using cost-effective processes comprising phosphorus ion implantation and LPCVD with in situ oxidation. In this work, the impact of a P-tail profile and boron emitter profile on the recombination currents in the non-metalized and metallized areas and the corresponding contact resistivity were systematically investigated.

The results indicated that a moderate doping tail (~0.15μm) within the c-Si bulk in a passivating contact is sufficient to avoid the high recombination and contact resistance caused by metal spikes, and that a homogeneous $p^+$ emitter with low peak concentration and deep junction depth is preferred in order to balance the passivation and contact performance. With optimized fabrication processes, an average efficiency of up to 23.85% with an excellent $V_{oc}$ of 703.5mV was obtained in the production line.

An implementation of the FELA approach in Quokka 3 revealed that optical factors (2.93%) are responsible for the largest power loss, and that recombination and resistive losses at the $p^+$ emitter are the second largest limitation for the record cell. With further process optimization, the best record efficiency in R&D of 24.21% was achieved, featuring a $V_{oc}$ of 711.6mV.

The reliability tests showed that n-type bifacial passivating-contact solar cells and modules are free from LID and are minimally impacted by LeTID, which consisted of light/current soaking and annealing. Rather than degrading performance, the light soaking and annealing processes have a positive effect on $V_{oc}$ and *FF*, which contribute to an improvement in efficiency of n-type bifacial passivating-contact solar cells and modules.

## References

[1] Richter, A. et al. 2019, "Both sides contacted silicon solar cells: Options for approaching 26% efficiency", *Proc. 36th EU PVSEC*, Marseille, France, pp. 90–95.

[2] Haase, F. et al. 2018, "Laser contact openings for local poly-Si-metal contacts enabling 26.1%-efficient POLO-IBC solar cells", *Sol. Energy Mater. Sol. Cells*, Vol. 186, pp. 184–193.

[3] Chen, J. et al. 2020, "Progress and application of the new generation n-type TOPCon technology", Presentation at 14th SNEC, Shanghai, China.

[4] JinkoSolar 2020, "JinkoSolar's large-area n-type monocrystalline silicon single junction cell has a conversion efficiency of 24.79%, a world record", News report [http://www.jinkosolar.com/site/newsdetail/815].

[5] Chen, D. et al. 2020, "24.58% total area efficiency of screen-printed, large area industrial silicon solar cells with the tunnel oxide passivated contacts (i-TOPCon) design", *Sol. Energy Mater. Sol. Cells*, Vol. 206, 110258.

[6] Sheng, J. et al. 2019, "Impact of phosphorus diffusion on n-type poly-Si based passivated contact silicon solar cells", *Sol. Energy Mater. Sol. Cells*, Vol. 203, 110120.

[7] Chen, J. et al. 2019, "The development of n-type bifacial silicon solar cell and module with passivating-contact technology in Jolywood", Presentation at 9th Silicon PV, Leuven, Belgium.

[8] Wu, W. et al. 2019, "Development of industrial n-type bifacial TOPCon solar cells and modules",

*Proc. 36th EU PVSEC*, Marseille, France, pp. 100–102.
[9] Bao, J. et al. 2020, "Towards 24% efficiency for industrial n-type bifacial passivating-contact solar cells with homogeneous emitter", *Proc. 37th EU PVSEC* (virtual event), pp. 160–163.
[10] Çiftpınar, H. et al. 2017, "Study of screen-printed metallization for polysilicon based passivating contacts", *Energy Procedia*, Vol. 124, pp. 851–861.
[11] Padhamnath, P. et al. 2019, "Metal contact recombination in monoPoly™ solar cells with screen-printed & fire-through contacts", *Sol. Energy Mater. Sol. Cells*, Vol. 192, pp. 109–116.
[12] Rienäcker, M. et al. 2016, "Junction resistivity of carrier-selective polysilicon on oxide junctions and its impact on solar cell performance", *IEEE J. Photovolt.*, Vol. 7, No. 1, pp. 11–18.
[13] Stodolny, M. et al. 2019, "Poly-Si contacting with second generation FT pastes and accurate characterization of contact resistances", Presentation at 8th Worksh. Metalliz. Interconn. Cryst. Sil. Sol. Cells, Konstanz, Germany.
[14] Liu, R. et al. 2019, "Metal contact performance optimization of n-type passivating-contact solar cells", Presentation at 15th CSPV, Shanghai, China.
[15] Brendel, R. et al. 2008, "Theory of analyzing free energy losses in solar cells", *Appl. Phys. Lett.*, Vol. 93, 173503.

## About the Authors

Jie Bao received his master's degree in optical engineering in 2017 from the Institute of Solar Energy Systems (ISES), Sun Yat-Sen University (SYSU). After graduating in 2017, he joined the Solar Cell R&D Center at Jolywood as a senior engineer. His research focuses on fabrication, characterization and simulation of n-type high-efficiency solar cells.

Cheng Chen studied physical electronics at Nanjing University of Science and Technology, China. In 2017 he joined Jolywood's R&D department as a senior engineer, focusing on the technology development, process integration and mass-production introduction of n-TOPCon solar cells.

Ronglin Liu studied microelectronics at Jiangnan University and received his master's degree in semiconductor device physics in 2009. In 2010 he started his career in the PV industry as an R&D engineer and focused on the industrialization of silicon solar cells. He joined Jolywood in 2015, where he initially focused on technology development and industrialization of n-PERT and n-TOPCon cells. Now, as an R&D manager, he leads the high-efficiency n-TOPCon team, working on efficiency optimization.

Zhencong Qiao studied condensed state physics at Henan University and received his master's degree in 2011. Later that year, he began working in the PV industry and focused on the industrialization of crystalline silicon. In 2016 he joined Jolywood, specializing in passivation and reliability of n-PERT and n-TOPCon cells. Now as an R&D manager, he leads the team involved in equipment and mass production of n-TOPCon solar cells.

Dr. Zheren Du received his bachelor of electrical engineering degree (Hons.) from the National University of Singapore (NUS) in 2010. He obtained his Ph.D. from the Department of Electrical and Computer Engineering at NUS and the Solar Energy Research Institute of Singapore (SERIS). He currently works for Jolywood, where he is in charge of the cell R&D department. His research interests include architecture, process, materials and laser processing applications in high-efficiency silicon-based solar cells.

Dr. Zhifeng Liu received his Ph.D. in the field of condensed matter physics from Nanjing University (NJU). In 2016 he was appointed director of the R&D Center, where he developed the industrialization-feasible process for IBC, n-PERT, n-TOPCon solar cells and modules. He founded and chaired the 2.4GW-capacity n-type bifacial solar cells factory. He is currently the deputy general manager of Jolywood, responsible for technology, overseas sales and marketing.

Dr. Jia Chen obtained his Ph.D. from the National University of Singapore. In 2014 he joined imec in Belgium, focusing on efficiency improvement of n-type silicon solar cells. Since 2018 he has been working at China-based Jolywood as the deputy general manager, responsible for R&D development of n-type cells and modules, such as TOPCon and IBC cell and module technologies.

## Enquiries

Jia Chen
Jolywood Solar Technology Co. Ltd.
No. 6 Kaiyang Rd.
Jiangyan Economic Development Zone
Taizhou City, Jiangsu Province
China, 225500

Tel: +86 13852664642
Email: chenjia@jolywood.cn

# monoPoly™ to biPoly™: Low-cost passivating contact technologies for efficiencies towards 25%

Naomi Nandakumar, Nitin Nampalli, Pradeep Padhamnath & Shubham Duttagupta, Solar Energy Research Institute of Singapore (SERIS), National University of Singapore (NUS)

## Abstract

Passivated emitter and rear cell (PERC) technology continues to dominate the solar industry as the standard in large-scale production. However, conventional PERC is limited to efficiencies below 23% in production. There is a need to push past this efficiency in high-volume manufacturing with low-cost technological improvements. In recent years, the emergence of screen-printed and fired polysilicon-based rear-side passivating contacts, such as in SERIS' monoPoly™ technology platform, have proved effective in achieving cell efficiencies of near 24% with an attractive low-cost upgrade to most PERC/PERT production lines. The significant reduction in carrier recombination at the rear contacts has enabled cell open-circuit voltages $V_{oc}$ greater than 705mV. To boost $V_{oc}$ and efficiencies beyond 24%, this paper presents preliminary results of SERIS' biPoly™ cell: the bifacial application of polysilicon-based passivating contact stacks with front and rear screen-printed and fired metallization. Both monoPoly and biPoly technologies can be integrated into existing manufacturing lines, enabling cell efficiencies above 24% to be obtained in mass production.

## Background

The global c-Si cell and PV module production capacity at the end of 2019 increased to ~200GWp as a result of continued passivated emitter and rear cell (PERC) capacity expansions [1]. The implementation of half-cell interconnections and the use of larger wafers have led to higher average PERC module powers. Today's mainstream p-type mono-Si-based modules reach efficiencies of ~20%. Improvements in the wafer material and the front and rear sides of the cells and the introduction of bifacial cell concepts are needed in order to boost module efficiencies further. It is likely that in the next few years, double-side contact cell concepts (e.g. PERC/PERT/TOPCon) will dominate the market, with passivating contacts on n-type mono-Si gaining market share over standard PERC technologies.

Passivating contact stacks consisting of polycrystalline silicon (poly-Si) on silicon oxide ($SiO_x$) show considerable promise, with cell efficiencies of 25.7% being achieved on laboratory-scale (<100cm²) solar cells, and up to 24.8% on industrial-scale (≥239cm²) solar cells, as presented in Fig. 1 [2–4].

SERIS' monoPoly™ platform for the monofacial application of poly-Si-based passivating contact stacks offers an ideal low-cost process that: 1) can be retrofitted to current solar cell lines; 2) is compatible with screen-printed and fired bifacial contacts; and 3) is cost competitive with standard PERC technology [5,6]. The monoPoly technology has achieved conversion efficiencies close to 24% on M2-sized wafers, with open-circuit voltages ($V_{oc}$) near 710mV and short-circuit current densities ($J_{sc}$) greater than 41mA/cm², as a result of the semitransparent nature of the layers (shown in Table 1). Note that the 23.2% reported was independently measured by ISFH.

As the PV industry progresses towards cell efficiencies in excess of 24%, the need for double-side passivating contacts, which significantly reduce front- and rear-contact recombination, becomes increasingly important. Current passivating contact cell technologies mainly deploy poly-Si stacks on the rear side, because of high parasitic absorption in the doped poly-Si layers and because of the inability to form screen-printed contacts to very thin poly-Si layers.

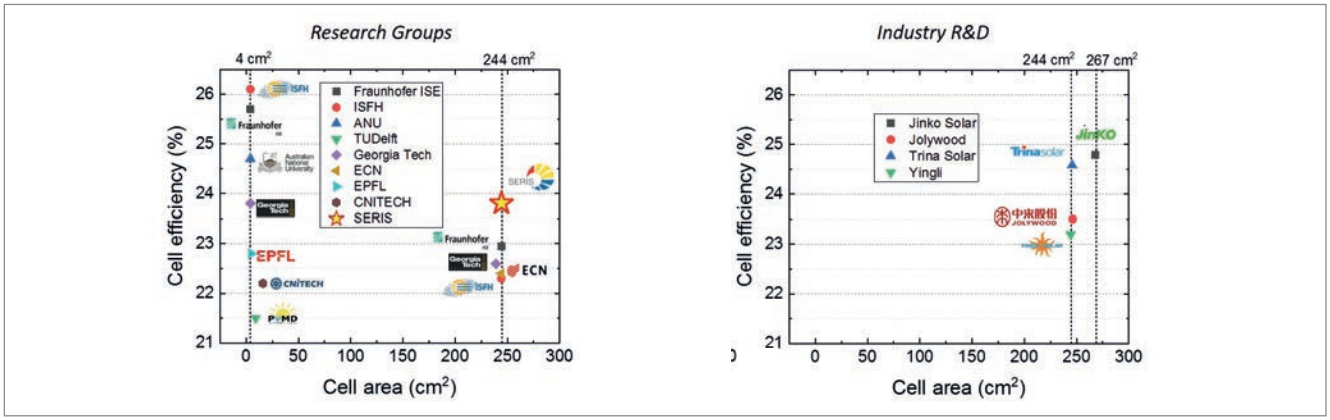


**Figure 1. Overview of solar efficiencies achieved with single-side poly-Si/$SiO_x$ passivating contact stacks on small-area (<100cm²) and large-area (≥239cm²) silicon wafer solar cells for various groups and industrial players, as reported at scientific conferences and in the press.**

This paper presents SERIS' biPoly™ technology platform, a follow-up to monoPoly; it incorporates the double-side (bifacial) application of poly-Si-based passivating contact stacks. Preliminary studies demonstrate recombination current density ($J_o$) values less than 5fA/cm² for both phosphorus-doped ($n^+$:poly-Si) and boron-doped ($p^+$:poly-Si) layers on an ultrathin interfacial $SiO_x$ layer.

Furthermore, silicon solar cell precursors fabricated with a front $n^+$ poly-Si/$SiO_x$ emitter and rear $p^+$ poly-Si/$SiO_x$ back-surface field (BSF), as shown in Fig. 2, have demonstrated implied $V_{oc}$ values of up to 730mV before metallization.

## biPoly layer properties

The front and rear biPoly stacks consist of an ultrathin (~2nm) interfacial oxide ($iO_x$) layer that is capped by either $n^+$- or $p^+$-doped poly-Si layers [7]. The stack can be deposited by either low-pressure chemical vapour deposition (LPCVD), atmospheric chemical vapour deposition (APCVD) or plasma-enhanced chemical vapour deposition (PECVD). The $iO_x$ is grown in situ in both cases (with no break in vacuum).

Doping of the poly-Si layers is achieved ex situ (LPCVD, APCVD) or in situ (PECVD), where the doped layers can be fabricated using a single-side high-throughput system, for example, in the case of PECVD. The properties of the poly-Si stacks are developed and optimized to meet the requirements for high-performing biPoly solar cells. The dopant profiles for the $n^+$ and $p^+$ poly-Si/$SiO_x$ stacks are presented in Fig. 3. Optimized peak dopant concentrations of $4\times10^{20}cm^{-3}$ for $n^+$ poly-Si and $3\times10^{19}cm^{-3}$ for $p^+$ poly-Si were found to be ideal for industrial screen-printed and fired metal contacts on the poly-Si. The optimized thickness of the poly-Si further ensures semitransparency at the front side of the biPoly solar cells.

| | $V_{oc}$ [mV] | $J_{sc}$ [mA/cm²] | *FF* [%] | $\eta$ [%] |
|---|---|---|---|---|
| Record batch | 697 | 41.4 | 81.3 | 23.5 |
| Record $V_{oc}$ | 707 | 40.4 | 81.2 | 23.2 |

**Table 1. Best-performing monoPoly *J–V* parameters.**

## Solar cell process flow

The introduction of passivating contacts to large-scale solar cell manufacturing is very appealing but at the same time challenging. High-throughput, low-cost deposition schemes are necessary for successful deployment of front and rear passivating contact stacks in mass manufacturing.

The typical process flows for standard pPERC and nPERT are presented in Fig. 4 for comparison. The pPERC process has a laser step after passivation, whereas the nPERT process has an additional $n^+$ diffusion to form the BSF on the rear. The pPERC process is representative and does not take into consideration any selective emitter process or the mandatory 'stabilization' process included in most PERC production lines today. Both pPERC and nPERT processes use standard screen-printed metallization with high-temperature firing to form the metal contacts.

In recent years, SERIS and its key industry partners have extensively developed the proprietary monoPoly passivating contact solar cell technology platform for mass production, which has produced efficiencies up to 23.5% (shown in Table 1), and also more recently close to 24%, where an independent verification of the results is ongoing at the moment. The monoPoly process – presented in Fig. 4 – is an eight-step simple and lean process flow that can be easily adapted to existing PERC/PERT production lines, with one additional tool required while maintaining the same number of total process steps. This passivating

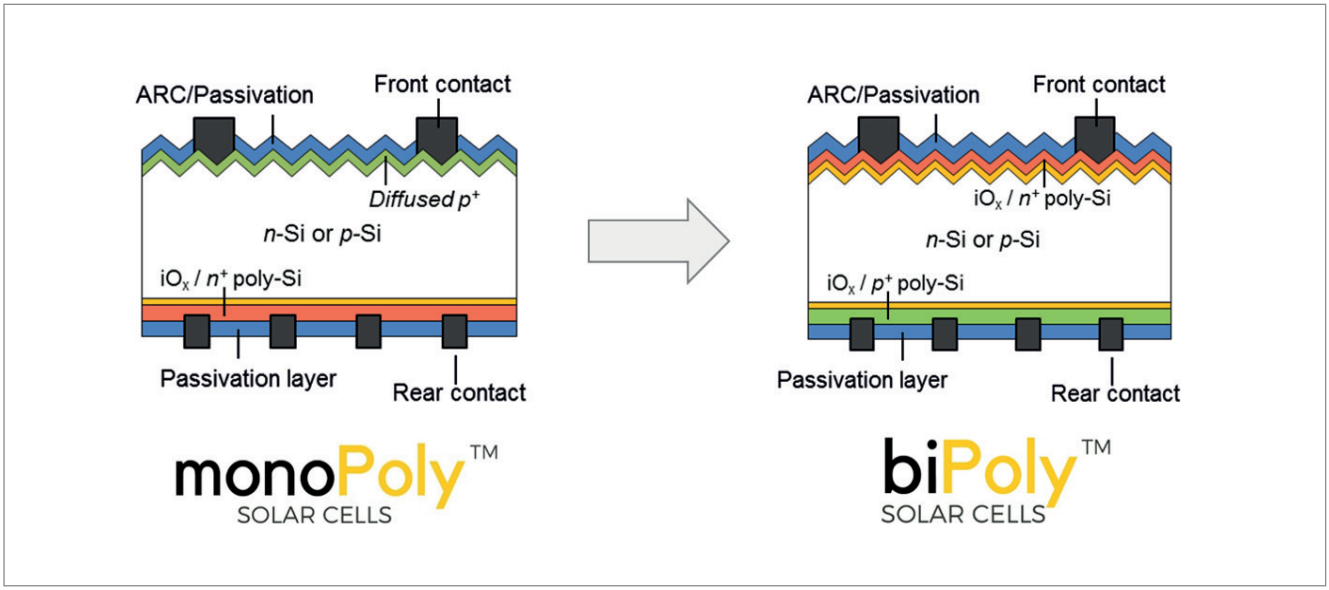


**Figure 2. Transition from a bifacial monoPoly cell to a bifacial biPoly cell with a front semitransparent electron-selective passivating contact stack and a rear hole-selective passivating contact stack.**

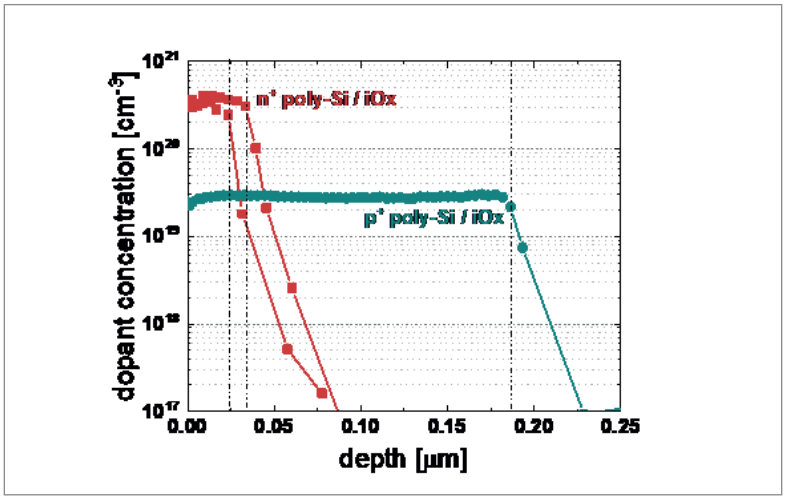


**Figure 3. Dopant profiles for ultrathin n$^+$ poly-Si (25 and 35nm) and p$^+$ poly-Si (180nm) on iO$_x$ stacks developed for the biPoly cell structure.**

"High-throughput, low-cost deposition schemes are necessary for successful deployment of front and rear passivating contact stacks in mass manufacturing."

contact process uses a unique PECVD process and set of equipment, enabling a streamlined method of manufacturing. The same lean process is now used for front-side application of a poly-Si on the oxide stack in the biPoly cell process – also presented in Fig. 4. With a single-side in situ process, the deposition of the front-side passivating contact stack simply replaces the emitter diffusion step in the monoPoly process.

## Efficiency potential

The preliminary passivation quality and implied solar cell performance of biPoly cell precursors is presented in Fig. 5. A 'first-attempt' i$V_{oc}$ of 710mV (at 1 sun) was achieved using an industrial process flow with front and rear poly-Si layers. Further optimization of the process, with improvements in the rear surface roughness, passivating contact stack properties and front layer thickness, pushed the i$V_{oc}$ to 730mV. These cell precursors have a thin front electron-selective n$^+$ poly-Si/iO$_x$ stack and a rear hole-selective p$^+$ poly-Si/iO$_x$ stack on a large-area M2-size low-resistivity n-type Cz-Si substrate. A corresponding total surface $J_o$ of 10fA/cm$^2$ and an implied fill factor (i*FF*) of more than 84.5% indicate very low device recombination at maximum power point (MPP) conditions. Low device recombination (i.e. high excess carrier density) at MPP not only helps to increase the upper *FF* limit but also increases the lateral carrier conductivity in the silicon base [8].

With the measured properties of i$V_{oc}$ and i*FF*, assuming an attainable $J_{sc}$ of 40mA/cm$^2$ for ultrathin ~25nm front n$^+$ poly-Si layers, the biPoly cell precursor has an implied cell efficiency (unmetallized) of close to 25%. This brings biPoly cell efficiencies on par with silicon heterojunction cells while retaining high-temperature stability, which is not possible with silicon heterojunction technology. Furthermore, existing PV production lines can be adapted for biPoly fabrication with cost-effective upgrades while retaining most of the existing PERC process steps (e.g. wet chemical steps, SiN$_x$ passivation, screen-printing and firing).

Some challenges remain, however, when fabricating a high-efficiency solar cell – in particular, the screen-printed metallization of the ultrathin biPoly layers using commercially available (non-optimized) metal pastes. With the rapid development of rear-side passivating contact technologies in the PV community (e.g. TOPCon, monoPoly, etc.), metal paste manufacturers are demonstrating continuing improvements in paste that can contact ultrathin poly-Si layers. It will not be long before improved paste formulations will help realize the efficiency potential of cell technologies with front and rear poly-Si passivating contacts, such as biPoly.

## Outlook and roadmap towards 30%

The current record efficiency for Si single-junction solar cells is 26.7% [9], with a theoretical efficiency limit of 29.56% [10] for single-junction Si cells because of unavoidable spectral losses and Auger recombination in the silicon material. The only way to surpass this limit is by adding a second solar cell in tandem – for example, multijunction cells with a silicon bottom cell and either a III-V semiconductor or a perovskite-based top cell.

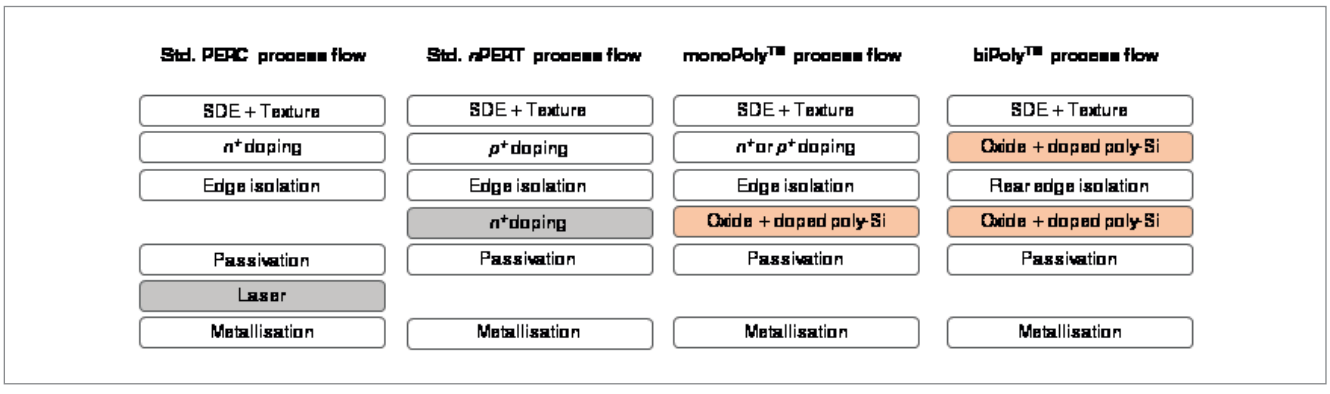


**Figure 4. Comparison of the standard PERC and PERT process flows with the simple eight-step process flows for the fabrication of monoPoly and biPoly solar cells, where the oxide and doped poly-Si can be deposited by PECVD, LPCVD or APCVD.**

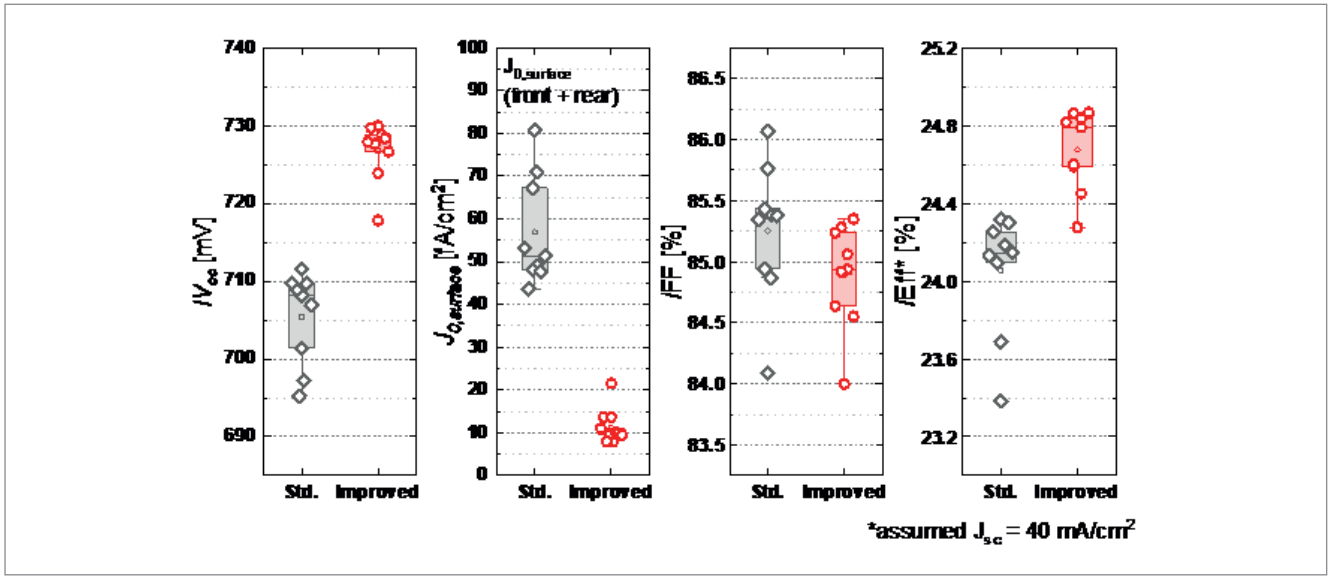


**Figure 5. Implied open-circuit volage (iV$_{oc}$) at 1 sun, total surface recombination current density (J$_{o,surface}$), implied fill factor (iFF) and implied efficiency (iE*ff*) of biPoly cell precursors fabricated at SERIS. Parameters are measured prior to metallization for standard and optimized process flows. A J$_{sc}$ of 40mA/cm$^2$ is assumed for iE*ff* estimations.**

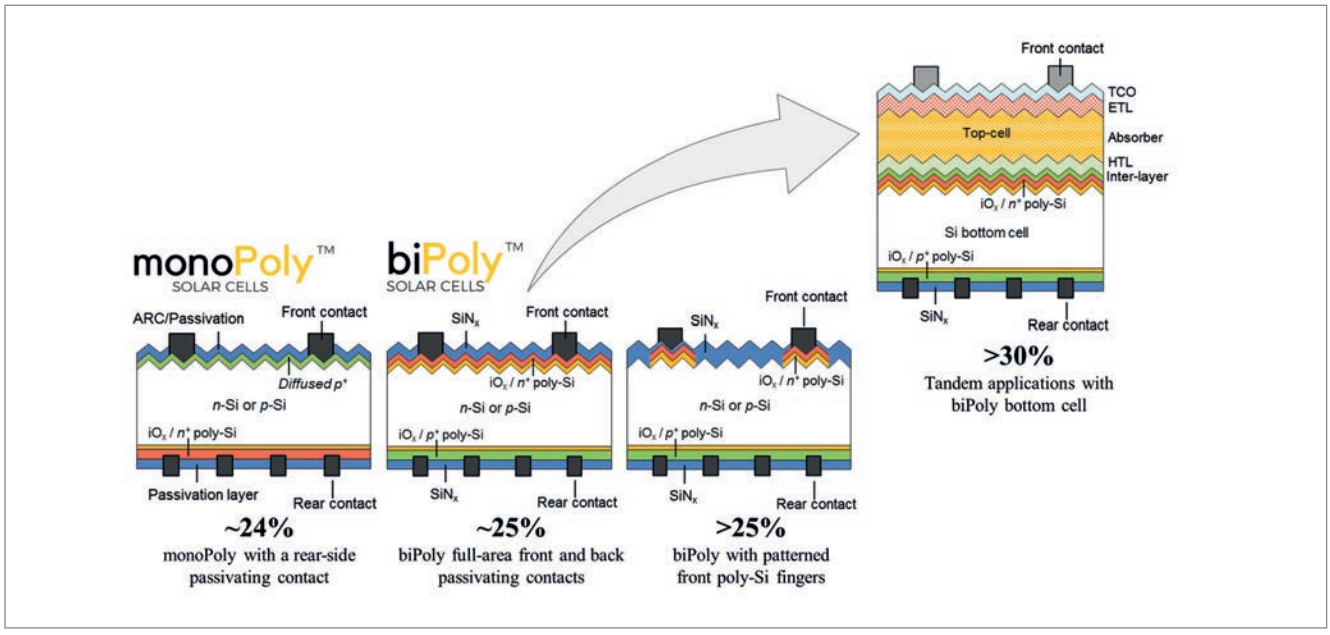


**Figure 6. Schematic roadmap depicting the evolution of current PERC cell technology to monoPoly, biPoly and biPoly$^+$ as the bottom cell in silicon-based tandem solar cell applications.**

Today, PERC technology holds a market share of more than 65% in the PV industry but is limited to cell efficiencies of ~22.5% in production. Integrating rear-side passivating contacts in PERC production lines will offer a boost in cell efficiencies to near 24%, while the addition of front-side passivating contacts will enable efficiencies of above 25% (Fig. 6). Furthermore, these high-$V_{oc}$ devices (potentially up to 740mV with SERIS' biPoly process) serve as an ideal cost-effective bottom cell upgrade for ~100GW of present day PERC lines. This paves the way from mainstream PERC to silicon-based tandem applications for efficiencies exceeding 30% in the PV industry [11,12].

## Summary

This paper has presented SERIS' monoPoly™ and biPoly™ cell technologies, for the adoption of rear-side and front-side passivating contacts in the c-Si PV industry. A simple process flow enabled by single-side in situ doped poly-Si layers yields cell efficiencies of close to 24% for the monoPoly technology, while biPoly cell precursors demonstrate i$V_{oc}$ values of up to 730mV, corresponding to an efficiency potential of 25%. These promising results pave the way for the adoption of passivating contacts in retrofitted PERC/PERT production lines today and as silicon bottom

"Integrating rear-side passivating contacts in PERC production lines will offer a boost in cell efficiencies to near 24%, while the addition of front-side passivating contacts will enable efficiencies of above 25%."

cells for high-efficiency >30% tandem solar cell applications.

**Acknowledgements**

SERIS, a research institute at the National University of Singapore (NUS), is supported by NUS, the National Research Foundation Singapore (NRF) and the Singapore Economic Development Board (EDB).

**References**

[1] VDMA 2020, "International technology roadmap for photovoltaic (ITRPV): Results 2019", 11th edn (Apr.) [https://itrpv.vdma.org/en/].

[2] Feldmann, F. et al. 2014, "Passivated rear contacts for high-efficiency n-type Si solar cells providing high interface passivation quality and excellent transport characteristics", *Sol. Energy Mater. Sol. Cells,* Vol. 120, pp. 270–274.

[3] Chen, D. et al. 2020, "24.58% total area efficiency of screen-printed, large area industrial silicon solar cells with the tunnel oxide passivated contacts (i-TOPCon) design", *Sol. Energy Mater. Sol. Cells,* Vol. 206, p. 110258.

[4] Bellini, E. 2020, "Jinko claims 24.79% efficiency for n-type monocrystalline cell", *pv magazine* (Jul.).

[5] Duttagupta, S. et al. 2018, "monoPoly cells: Large-area crystalline silicon solar cells with fire-through screen-printed polysilicon contacts", *Sol. Energy Mater. Sol. Cells*, Vol. 187, pp. 76–81.

[6] Nandakumar, N. et al. 2019, "Approaching 23% with large-area monoPoly cells using screen-printed and fired rear passivating contacts fabricated by inline PECVD", *Prog. Photovolt: Res. Appl.,* Vol. 27, No. 2, pp. 107–112.

[7] Nandakumar, et al. 2019, "Investigation of 23% monoPoly screen-printed silicon solar cells with an industrial rear passivated contact", *Proc. 46th IEEE PVSC*, Chicago, Illinois, USA, pp. 1463–1465.

[8] Haschke, J. et al. 2019, "Injection-dependent lateral resistance in front-junction solar cells with nc-Si: H and a-Si: H hole selective contact", *Proc. 46th IEEE PVSC*, Chicago, Illinois, USA, pp. 3042–3045.

[9] Yoshikawa, K. et al. 2017, "Silicon heterojunction solar cell with interdigitated back contacts for a photoconversion efficiency over 26%", *Nature Energy*, Vol. 2, No. 5, p. 17032.

[10] Schäfer, S. & Brendel, R. 2018, "Accurate calculation of the absorptance enhances efficiency limit of crystalline silicon solar cells with Lambertian light trapping", *IEEE J. Photovolt.,* Vol. 8, No. 4, pp. 1156–1158.

[11] Peibst, R. et al. 2018, "From PERC to tandem: POLO-and $p^+/n^+$ poly-Si tunneling junction as interface between bottom and top cell", *IEEE J. Photovolt.*, Vol. 9, No. 1, pp. 49–54.

[12] Hermle, M. et al. 2020, "Passivating contacts and tandem concepts: Approaches for the highest silicon-based solar cell efficiencies", *Appl. Phys. Rev.*, Vol. 7, No. 2, p. 021305.

**About the Authors**

Dr. Naomi Nandakumar is the team leader for Solar Cell Innovations in the Advanced Silicon Solar Cells group within the Silicon Solar Cells and Modules (SSCM) Cluster at SERIS, where her research focuses on the development of advanced high-efficiency solar cells fabricated using industrial processes. She holds a Ph.D. in electrical engineering and an M.Sc. in applied physics from NUS. For her Ph.D. she investigated functional thin films deposited by spatial atomic layer deposition for PV applications.

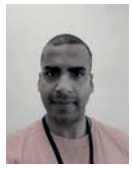

Dr. Nitin Nampalli is the team leader for Heterojunction Solar Cells in the Advanced Silicon Solar Cells group at SERIS. His current research focuses on the development of heterocontacts and novel materials for high-efficiency solar cells using industrial processes. He received his bachelor's degree in microelectronics from Rochester Institute of Technology (USA), and holds a Ph.D. and a master's in photovoltaics from the University of New South Wales (UNSW), where he developed industrial approaches for hydrogenation and bulk defect mitigation in p-type silicon solar cells.

Pradeep Padhamnath is a research scholar in the Department of Electrical and Computer Engineering, National University of Singapore. He is attached to SERIS, where his research focuses on the development of advanced metallization of high-efficiency passivated-contact solar cells fabricated using industrial processes. He holds an M.Tech degree in energy systems engineering from IIT Bombay, as well as dual bachelor's in materials engineering and mechanical engineering.

Dr. Shubham Duttagupta is deputy director of the Silicon Solar Cells and Modules (SSCM) Cluster at SERIS and is also head of the Advanced Silicon Solar Cells group within the SSCM Cluster. His research group focuses on the development and commercialization of large-area >25%-efficient crystalline silicon solar cells and high-efficiency processes. His Ph.D. research involved the development of advanced multifunctional materials required for high-efficiency crystalline silicon wafer solar cells.

**Enquiries**

Shubham Duttagupta
shubham.duttagupta@nus.edu.sg

# Advertisers and web index

| ADVERTISER | WEB ADDRESS | PAGE NO. |
|---|---|---|
| Aiko Cells | en.aikosolar.com | Outside Back Cover |
| EU PVSEC 2021 | www.photovoltaic-conference.com | Inside Back Cover |
| Exateq GmbH | www.exateq.de | 34 |
| Intersolar Global | www.intersolar.de | 45 |
| JA Solar | www.jasolar.com | Inside Front Cover |
| Mondragon Assembly | www.mondragon-assembly.com | 10 |
| PV CellTech 2021 | celltech.solarenergyevents.com | 69 |
| PV ModuleTech 2021 | moduletech.solarenergyevents.com | 23 |
| PV TechTalk | www.pv-tech.org | 53 |
| RENA | www.rena.com | 57 |
| Sentech Instruments GmbH | www.sentech.com | 62 |
| Seraphim Energy | www.seraphim-energy.com | 7 |
| Singulus Technologies AG | www.singulus.com | 39 |
| SNEC PV Power Expo 2021 | www.snec.org.cn | 14 |
| Trina Solar | www.trinasolar.com | 5 |
| Von Ardenne GmbH | www.vonardenne.biz | 30 |

**To advertise within Photovoltaics International, please contact the sales department: Tel +44 (0) 20 7871 0122**

# EU PVSEC 2021

## 38th European Photovoltaic Solar Energy Conference and Exhibition

***THE INNOVATION PLATFORM FOR THE GLOBAL PV SOLAR SECTOR***

**06 - 10 SEPTEMBER 2021**

**LISBON PORTUGAL**

**SAVE THE DATE**

**We hope to see you all in person next year in Lisbon!**

We are monitoring current developments very carefully and reserve the right to change the concept if the situation requires it.

Photo by Daoudi Aissa on Unsplash

**www.photovoltaic-conference.com**
**www.photovoltaic-exhibition.com**

Aiko CELLS
made from the heart

Aikosolar

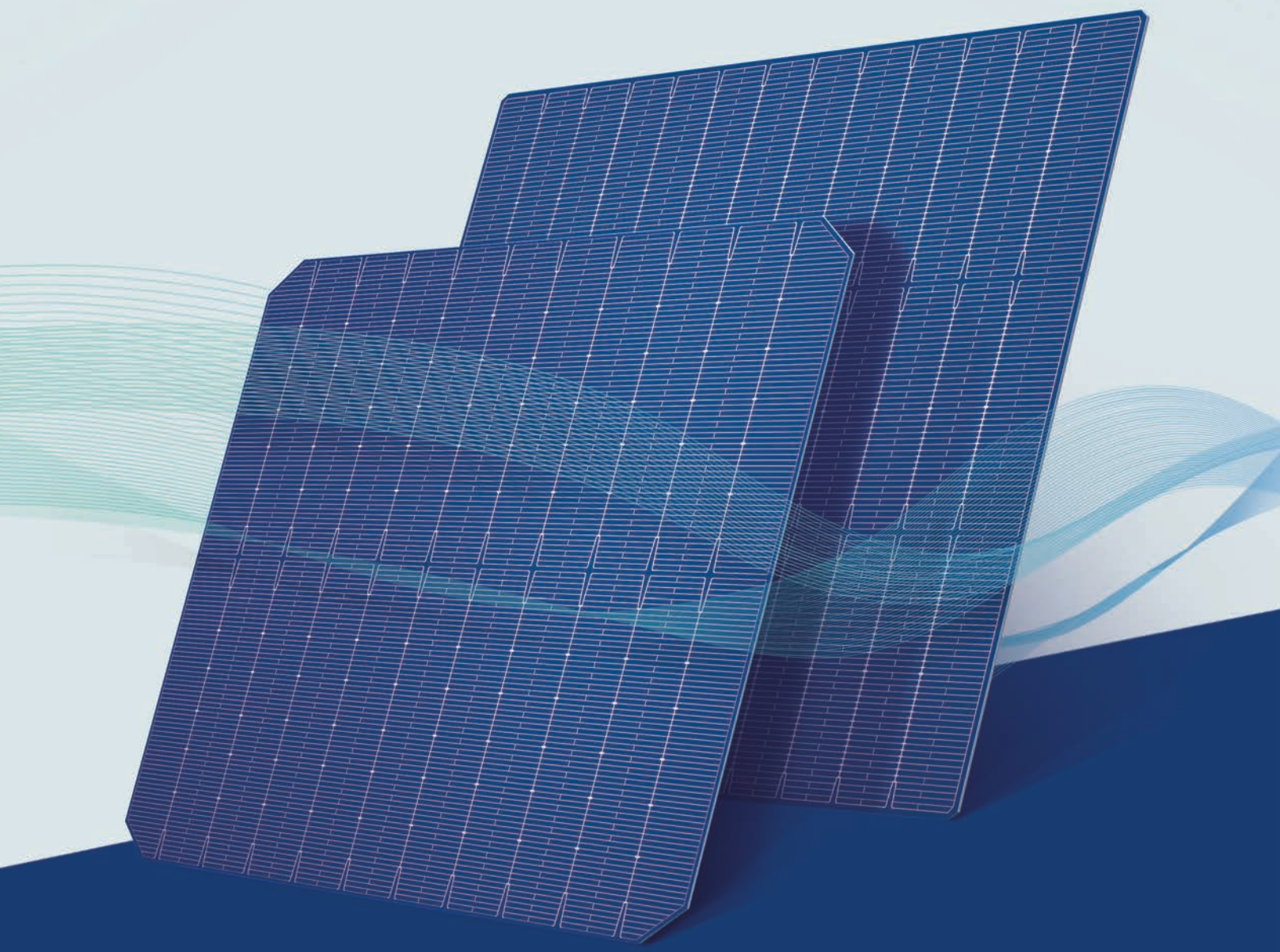

## Aikosolar's High Efficiency PERC Cell

Front Side Efficiency **>23%**

Assisting Module Power Output **600W+**

## Bifacial Cells Metrology & Classification

Classification Standard : Front Side 0.1% & Rear Side 0.5%

Provide Highly Reliable Products For Customers